

# STELLINGEN

TR3284 S

behorende bij het proefschrift

'Computation of flow at all speeds with a staggered scheme'

door Hester Bijl

1. Door combinatie van discretisatie van de compressibele stromingsvergelijkingen op een 'staggered' rooster en een geschikte nondimensionalisering kunnen zowel compressibele als incompressibele stromingen efficiënt en nauwkeurig worden berekend. Met deze methode kan een nauwkeurige oplossing worden bepaald in een beperkte, van het Mach getal onafhankelijke rekentijd.
2. Omdat volstaan kan worden met het vervangen van afgeleiden door centrale of eenzijdige differenties, vergt een 'staggered' schema voor de Euler vergelijkingen in principe beduidend minder rekentijd dan 'colocated' schema's gebaseerd op flux-evaluatie met 'approximate Riemann solvers'.
3. De mogelijkheden van numerieke stromingsleer worden nog onderbenut in praktische toepassingen. Ruimere toepassing van numerieke methoden voor stromingsvraagstukken in de praktijk biedt kansen voor besparingen bij de gebruiker, nieuwe inzichten bij de onderzoeker en meer inkomsten voor de universiteit.
4. Informatietechnologie biedt de wetenschap interessante mogelijkheden om de bundeling, beoordeling en verspreiding van wetenschappelijke artikelen zelf te organiseren. Als gevolg hiervan zullen de wetenschappelijke uitgeverijen, die geen wezenlijke inhoudelijke meerwaarde leveren, een belangrijk deel van hun inkomsten in de komende jaren zien verdwijnen.
5. Het investeringsbeleid van de Nederlandse overheid zal leiden tot een afname van hoogwaardig technologisch vernuft en tot een overschot aan fysieke capaciteit - goederenspooren en landingsbanen - voor relatief laagwaardige transportdiensten. Hierdoor wordt Nederland niet de Silicon Valley, maar het rangeerterrein van Europa.
6. De wachtgeldregeling op de Nederlandse universiteiten belemmert de uitstroom van improductieve medewerkers en maakt tegelijkertijd het aantrekken van jong talent moeilijker. Alleen door afschaffing van deze regeling en invoering van een op kwaliteit gericht personeelsbeleid kan de universiteit de middelmatigheid, de onwil en de verveling met succes bestrijden.
7. Positieve discriminatie bestaat niet. Een expliciet voorkeursbeleid voor aanstelling van vrouwen is nadelig voor zowel mannen als vrouwen.
8. De door Noam Chomsky ontwikkelde 'Government and Binding' theorie, een universeel grammaticaraamwerk, is meer een op zich zelf staande kunst dan een zinvol instrument om taal te leren, te analyseren, te vertalen of te genereren. Er zijn zoveel extra regels nodig om

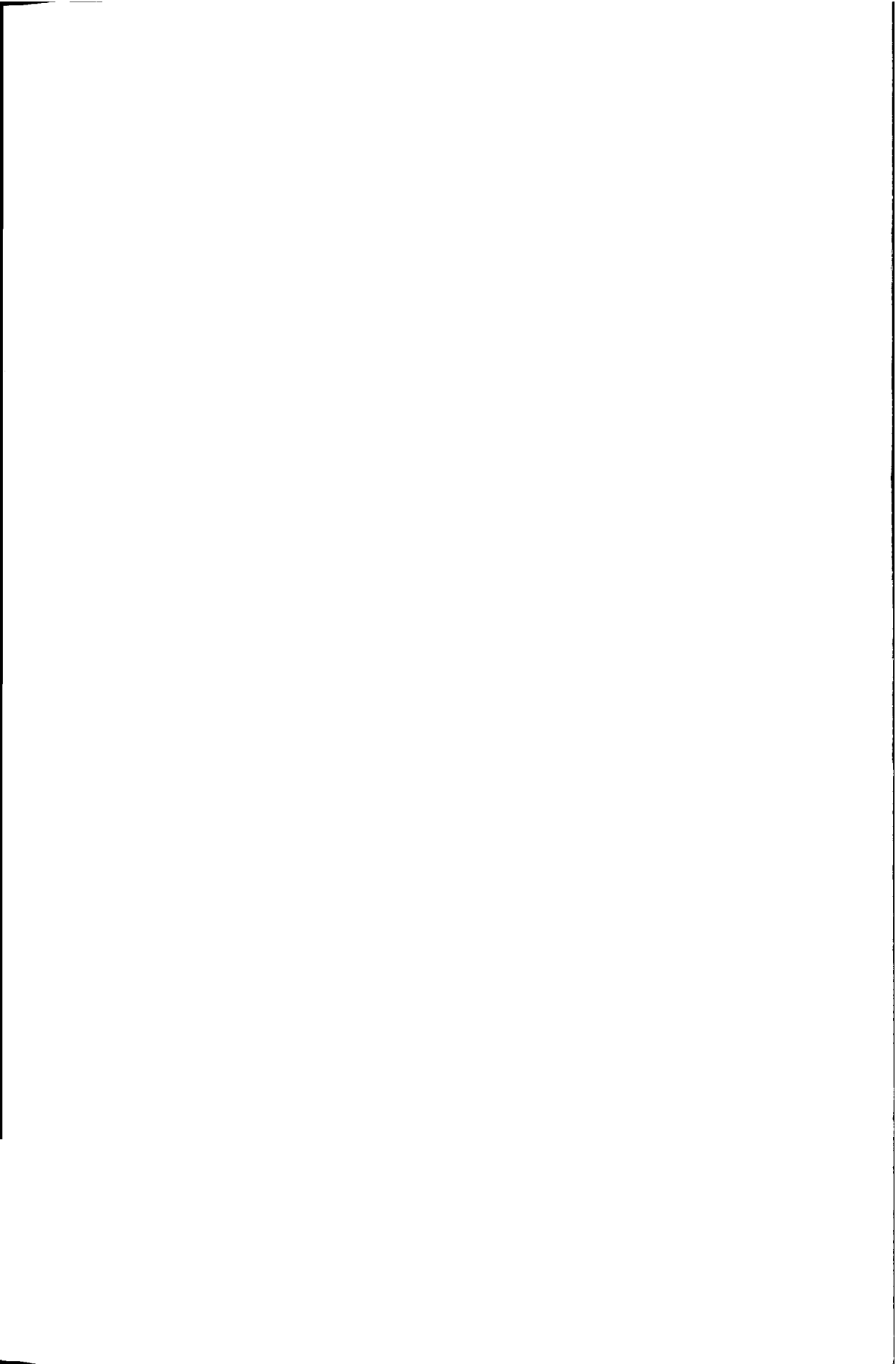
uitzonderingen per taal te beschrijven, dat volledig taalspecifieke methoden veelal de voorkeur verdienen.

9. De bij fusies en overnames verwachte schaalvoordelen - vooral die in ondersteunende en administratieve functies - zijn veelal theoretisch moeilijk verdedigbaar en blijken in de praktijk vaak niet te materialiseren.

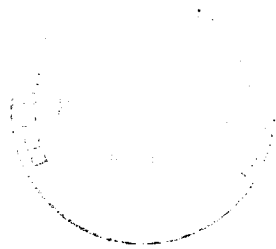
10. Het promotieprotocol van de Technische Universiteit Delft, inclusief de kledingvoorschriften, is sterk verouderd en betuttelend voor de betrokkenen. Door aanpassing en vereenvoudiging van het reglement ontstaat bovendien ruimte voor bezuiniging op de dienst Protocollaire Zaken van de universiteit.

328'  
7u89u7  
3-72182  
TR3284

Computation of flow at all speeds  
with a staggered scheme



# Computation of flow at all speeds with a staggered scheme



## PROEFSCHRIFT

ter verkrijging van de graad van doctor  
aan de Technische Universiteit Delft,  
op gezag van de Rector Magnificus prof. ir. K.F. Wakker,  
in het openbaar te verdedigen ten overstaan van een commissie,  
door het College voor Promoties aangewezen,

op maandag 1 februari 1999 te 13.30 uur  
door Hester BIJL,  
wiskundig ingenieur,  
geboren te Voorburg.

Dit proefschrift is goedgekeurd door de promotor:  
Prof. dr. ir. P. Wesseling

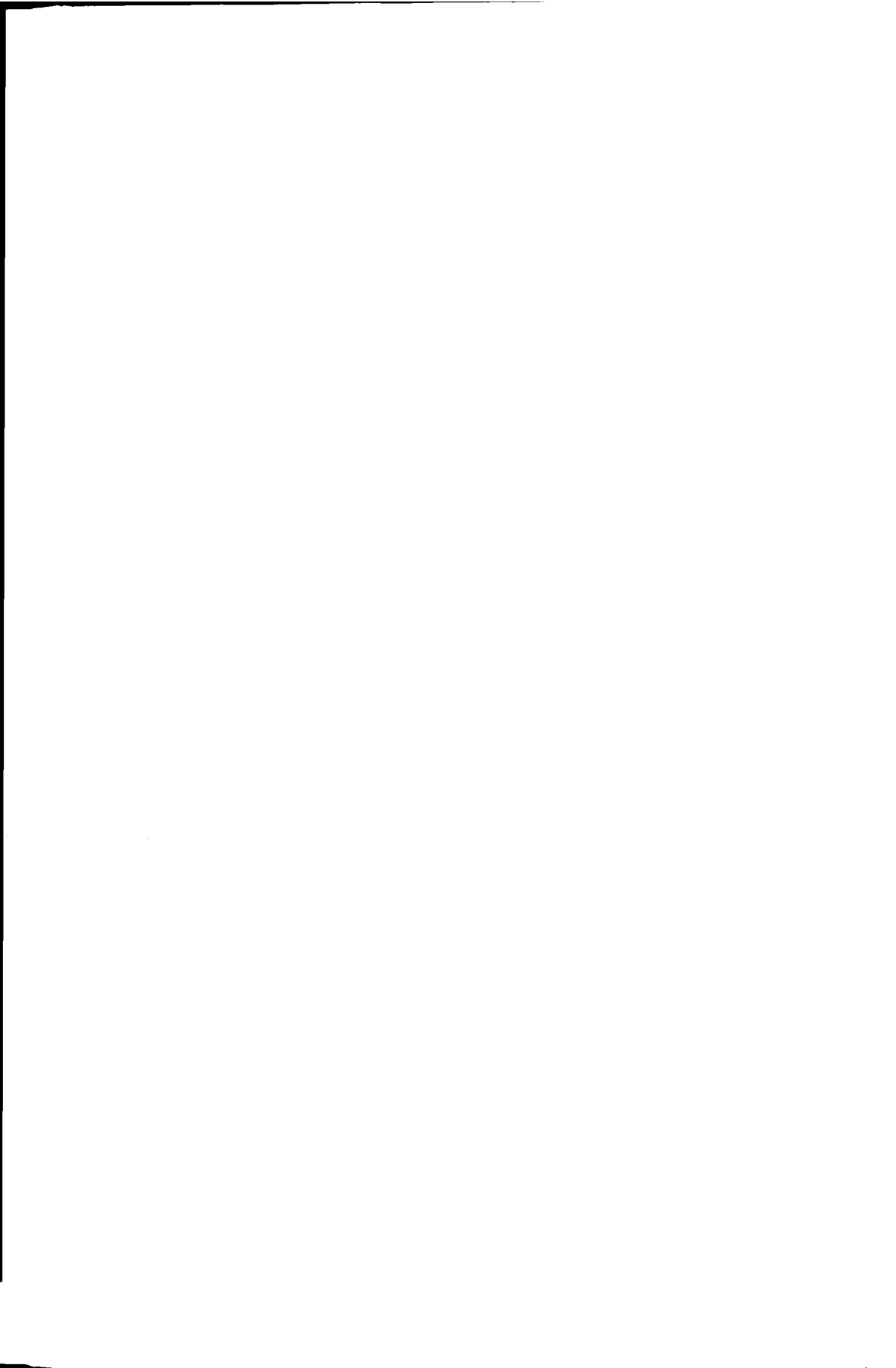
Samenstelling promotiecommissie:

Rector Magnificus,  
Prof. dr. ir. P. Wesseling,  
Prof. dr. ir. C.J. van Duijn,  
Prof. dr. ir. H.W.M. Hoeijmakers,  
Prof. dr. D. Kröner,  
Prof. dr. ir. G. Ooms,  
Prof. dr. D.J.E.M. Roekaerts,  
Dr. ir. C. Vuik,

voorzitter  
Technische Universiteit Delft, promotor  
Technische Universiteit Delft  
Universiteit Twente  
Institut für Angewandte Mathematik  
Technische Universiteit Delft  
Technische Universiteit Delft  
Technische Universiteit Delft

Dit onderzoek werd gesteund door de Stichting der Technische Wetenschappen (STW).

*voor Leen Bijl*





# Summary and conclusions

## Computation of flow at all speeds with a staggered scheme

In Computational Fluid Dynamics a rigid division exists between methods for the computation of compressible and incompressible flows. This makes computation of a flow that has both compressible and incompressible regions or characteristics difficult. Straightforward use of standard methods for the computation of compressible flow, though relatively easy, gives severe convergence problems or even breakdown in the presence of regions with incompressible characteristics. These regions are low Mach number regions, since a low Mach number is a necessity for incompressibility.

In this thesis a numerical method is developed that is especially designed for efficient and accurate computation of both compressible and incompressible flows, or briefly flow at all speeds. Tests show that with this method an accurate solution can be computed in a limited time with a Mach number independent convergence rate. Furthermore, the Mach number can be prescribed to be arbitrarily small, including zero, in which case the incompressible scheme of Harlow and Welch [23] (in orthogonal coordinates) or that of Wesseling et al. [83, 92, 93] (in general coordinates) is recovered. Moreover, temporal accuracy is obtained in a simple manner, without introducing a pseudo-time variable and dual time stepping, as required in many other methods designed to tackle the same problem. Finally, surprisingly good performance of the scheme in the fully compressible case is demonstrated.

The two most important building blocks of the method are:

- nondimensionalisation of the variables to eliminate the singularity associated with  $M \downarrow 0$
- discretisation of the compressible flow equations on a staggered grid to avoid spurious pressure modes in the limit  $M \downarrow 0$

Furthermore, we use mass flux, pressure and enthalpy as primary unknowns. In our method, first, the nondimensionalised compressible flow equations are discretised in general coordinates in space using a finite volume method on a staggered mesh. Then, these equations are discretised in time with the  $\theta$ -method and solved with a compressible extension of the pressure correction method. This means that after the energy

equation a mass flux predictor equation is solved. The predicted mass flux is then corrected with a term following from solution of the pressure correction equation, an equation derived from manipulation of the original equations. All three systems of discrete equations are solved using a preconditioned Krylov subspace method: preconditioned GMRES.

From various test cases we conclude that with our method flows at all speeds can be efficiently and accurately computed. That is, an accurate solution can be computed in a limited time with a Mach number independent convergence rate. Simulations are done for the channel with bump with inlet Mach numbers equal to 0 up to 0.5, and for a strongly converging-diverging nozzle with Mach numbers varying from 0.045 up to 2.67 in the flow domain. Furthermore, shocks are computed as accurately as with methods with a comparably accurate discretisation. This is shown for the channel with bump with inlet Mach numbers equal to 0.675 and 1.65. Also for fully compressible nonstationary flows the present staggered scheme is as accurate as colocated compressible schemes. This is shown for various Riemann problems, including shocks, contact discontinuities and expansion waves. Furthermore, from results for the NACA0012 airfoil we conclude that our method is also suitable for computation of flows with stagnation points. Finally, the method is applied to a realistic industrial flow with varying Mach numbers, namely an industrial blower configuration in use at AKZO Nobel.

Hester Bijl

# Contents

Summary	iii
Notation	vii
<b>1 Introduction</b>	<b>1</b>
1.1 The main issue	1
1.2 Scope of this study	2
1.3 Outline of this thesis	3
<b>I Difficulties associated with standard methods</b>	<b>5</b>
<b>2 Relation between compressible and incompressible flow</b>	<b>7</b>
2.1 Equations governing flow of Newtonian fluids	7
2.2 Definition of incompressible flow	10
2.3 Conditions for incompressible flow	10
2.3.1 Small pressure change $\rightarrow M \ll 1$	11
2.3.2 Small entropy change $\rightarrow$ small heat release	13
2.4 Asymptotic expansion for $M \downarrow 0$	15
2.4.1 Expanded variables in the flow equations	16
2.4.2 Low Mach number flow versus incompressible flow equations	19
2.4.3 Physical significance of pressure variables	20
<b>3 Computations for <math>M \downarrow 0</math>, difficulties and remedies</b>	<b>23</b>
3.1 Computational difficulties when $M \downarrow 0$	23
3.1.1 Bad convergence due to disparity of wave speeds	23
3.1.2 Cancellation due to disparity between mean pressure field and pressure differences	24
3.1.3 Weak pressure-density coupling	25
3.1.4 Singularity of limit $M \downarrow 0$	25
3.2 Previously proposed remedies and their shortcomings	26
3.2.1 Asymptotic expansion techniques	26
3.2.2 Extension of methods for compressible flows	26
3.2.3 Extension of methods for incompressible flows	28

<b>II</b>	<b>The present method</b>	<b>31</b>
<b>4</b>	<b>Mach-uniform formulation of the Euler equations</b>	<b>33</b>
4.1	<i>Dimensionless formulation for arbitrary reference values</i> . . . . .	33
4.2	Breakdown of standard compressible formulation as $M \downarrow 0$ . . . . .	35
4.3	Alternative non-dimensionalisation, valid for $M \downarrow 0$ . . . . .	35
4.3.1	Reference pressure equal to reference dynamic pressure . . . . .	35
4.3.2	Reference values equal to stagnation conditions . . . . .	37
4.3.3	Dimensionless equations and boundary conditions . . . . .	37
<b>5</b>	<b>Discretisation of the compressible equations on a staggered grid</b>	<b>39</b>
5.1	Invariant formulation in general coordinates . . . . .	39
5.2	Staggered grid and associated geometric quantities . . . . .	41
5.3	The continuity equation . . . . .	44
5.3.1	Finite volume discretisation . . . . .	44
5.4	The momentum equations . . . . .	45
5.4.1	Finite volume discretisation . . . . .	45
5.4.2	Central approximation of convection term . . . . .	46
5.4.3	Upwind approximation of convection term . . . . .	48
5.5	The energy equation . . . . .	49
5.5.1	Finite volume discretisation . . . . .	49
5.6	The equation of state . . . . .	50
5.7	Upwind methods . . . . .	51
<b>6</b>	<b>Solution strategy</b>	<b>53</b>
6.1	Time integration by the $\theta$ -method . . . . .	53
6.2	Original pressure correction method . . . . .	54
6.2.1	Derivation of compressible pressure correction equation . . . . .	55
6.2.2	Overview of solution algorithm . . . . .	56
6.2.3	Solution algorithm in one dimension . . . . .	57
6.3	Alternatives for better preservation of contact discontinuities . . . . .	60
6.3.1	Alternative pressure correction equation . . . . .	60
6.3.2	Conservative energy equation . . . . .	61
6.4	Iterative solver: preconditioned GMRES . . . . .	62
<b>7</b>	<b>Extension to the Navier-Stokes equations</b>	<b>65</b>
7.1	Dimensionless equations . . . . .	65
7.2	Discretisation in general coordinates on a staggered grid . . . . .	66
7.3	Solution strategy . . . . .	68

<b>III</b>	<b>Results obtained with the present method</b>	<b>71</b>
<b>8</b>	<b>Demonstration of Mach-uniform accuracy and efficiency</b>	<b>73</b>
8.1	Channel with bump . . . . .	73
8.1.1	Inviscid incompressible flow . . . . .	74
8.1.2	Inviscid subsonic flow . . . . .	75
8.1.3	Inviscid transonic flow . . . . .	75
8.1.4	Inviscid supersonic flow . . . . .	77
8.1.5	Viscous subsonic flow . . . . .	79
8.2	Converging-diverging nozzle . . . . .	81
<b>9</b>	<b>Validation for Riemann problems</b>	<b>85</b>
9.1	Analytical aspects . . . . .	85
9.1.1	Stationary shock waves . . . . .	86
9.1.2	Moving normal shock waves . . . . .	88
9.1.3	Expansion fans . . . . .	88
9.1.4	Contact discontinuities . . . . .	90
9.1.5	Analytical solution of the Riemann problem . . . . .	90
9.2	Numerical results . . . . .	93
9.2.1	Sod's shock tube problem . . . . .	93
9.2.2	Test case of Lax . . . . .	96
9.2.3	Supersonic flow test case . . . . .	98
9.2.4	Test case with nonstationary contact discontinuity . . . . .	101
9.2.5	Final remarks . . . . .	103
<b>10</b>	<b>Applications</b>	<b>105</b>
10.1	Industrial application . . . . .	105
10.1.1	Flow type and domain . . . . .	106
10.1.2	Boundary conditions . . . . .	108
10.1.3	Computational results for straight fiber channel . . . . .	111
10.1.4	Computational results for fiber channel with widening . . . . .	115
10.2	Flow around an airfoil . . . . .	117
10.2.1	Final remarks . . . . .	122
	<b>Bibliography</b>	<b>123</b>
	<b>Samenvatting</b>	<b>130</b>



# Notation

## List of Symbols

$\alpha$	isothermal compressibility
$\mathbf{a}^\alpha, \alpha = 1, 2, 3$	contravariant base vector
$\mathbf{a}_\alpha, \alpha = 1, 2, 3$	covariant base vector
$a$	speed of sound
$\beta$	bulk expansion coefficient
$c_p$	specific heat at constant pressure
$c_v$	specific heat at constant volume
$e_{\alpha\beta}, \alpha, \beta = 1, 2, 3$	rate of strain tensor
$E$	total energy
$e$	internal energy
$f_\alpha, \alpha = 1, 2, 3$	external force in the direction of $x^\alpha$
$\gamma = \frac{c_p}{c_v}$	ratio of specific heats
$\sqrt{g}$	Jacobian of coordinate mapping
$g^{\alpha\beta}, \alpha, \beta = 1, 2, 3$	contravariant metric tensor
$g_{\alpha\beta}, \alpha, \beta = 1, 2, 3$	covariant metric tensor
$h$	enthalpy
$k$	heat conductivity
$L$	characteristic length
$M$	Mach number
$\mu$	dynamic viscosity
$\mu_{art}$	artificial viscosity
$m^\alpha = \rho u^\alpha$	momentum components
$\Phi$	rate of dissipation
$p$	pressure
$p_v$	pressure ratio
$q$	heat release rate
$\rho$	density
$R = c_p - c_v$	gas constant
$Re$	Reynolds number
$s$	entropy
$\tau_{\alpha\beta}, \alpha, \beta = 1, 2, 3$	viscous stress tensor
$\tau$	characteristic time

$\theta$	time stepping parameter
$t$	time
$T$	temperature
$u_\alpha, \alpha = 1, 2, 3$	velocity components
$U$	characteristic velocity
$U^\alpha, \alpha = 1, 2, 3$	contravariant velocity component
$U_\alpha, \alpha = 1, 2, 3$	covariant velocity component
$V^\alpha = \sqrt{g}U^\alpha, \alpha = 1, 2, 3$	mass flux
$\xi^\alpha, \alpha = 1, 2, 3$	spatial coordinates in curvilinear coordinate system
$x_\alpha, \alpha = 1, 2, 3$	spatial coordinates in a Cartesian coordinate system

## Conventions

The basic equations will be derived in a right-handed Cartesian coordinate system  $(x_1, x_2, x_3)$  with three dimensions. Bold-faced lower case Latin letters will be used to denote vectors, for example  $\mathbf{x} = (x_1, x_2, x_3)$ . Greek letters will be used for scalars. In this thesis the *summation convention* is used, which means that summation takes place over Greek indices that occur twice in a term, for example:

$$\frac{\partial}{\partial x_\beta} \tau_{\alpha\beta} = \sum_{\beta=1}^d \frac{\partial}{\partial x_\beta} \tau_{\alpha\beta}$$



# 1

## Introduction

In Computational Fluid Dynamics a rigid division exists between numerical methods for the computation of compressible and incompressible flows. This makes computation of a flow that has both compressible and incompressible flow regions or characteristics difficult. In the literature several solutions to this problem are listed, but they all have one or more disadvantageous properties. Therefore, we have developed a new approach, extending and improving the early work of Harlow and Amsden [21, 22].

### 1.1 The main issue

The partition of flows into compressible and incompressible flows is based on the Mach number  $M = \frac{|u|}{a}$ , equal to the speed of the flow  $|u|$  divided by the speed of sound in the flow  $a$ . When the Mach number in a flow is uniformly low, say below 0.3, incompressible governing equations are employed. Solution can take place with numerical methods specially suited for the incompressible flow case, and the velocity field is assumed to be divergence free. When the Mach number is higher, compressible flow governing equations need to be employed, and numerical methods different from those for the incompressible flow case are used. This leaves us with the question: what to do when a flow has both compressible and incompressible flow regions or characteristics?

What is needed is a method with Mach-uniform accuracy and efficiency, both as the Mach number  $M \downarrow 0$  and when  $M = \mathcal{O}(1)$ . Straightforward use of standard methods for the computation of compressible flows gives severe convergence problems or even breakdown in the presence of regions with very low Mach number. Therefore efforts have been made to develop special methods for such flows.

For low speed variable density flows asymptotic methods based on series expansion in the Mach number have been developed in [19, 37, 49]. Such methods can only be used when the Mach number is small enough (less than 0.3 say). Another approach is to improve the low Mach number behaviour of compressible flow methods. Because large investments have been made in codes for compressible flows, much work has been done in this direction. Extension to low Mach numbers can be done by preconditioning

[11, 14, 18, 63, 71, 72, 76, 79]. Another possibility is to perturb the equations with artificial compressibility, replacing the physical acoustic modes by artificial acoustic modes [13, 19, 28, 45, 46, 47, 57, 78, 86]. These measures usually falsify the time dependence, making time-accurate unsteady computations awkward or inefficient. Also, usually very small Mach numbers (less than 0.05, say) cannot be handled, or only at increasing expense, and the limit  $M \downarrow 0$  is frequently singular. Such low Mach numbers are encountered in flows with combustion or in stratified atmospheric flows. Another type of method is proposed by Patnaik et al. [53]; here the density is stepped forward in time by the continuity equation, and a pressure correction equation is derived from the energy equation. The method can compute sound waves and instationary weakly compressible flows. It would seem that this method does not reduce to a well-known incompressible flow method as  $M \downarrow 0$ . All of the above methods use nonstaggered grids.

Alternatively, one may extend a numerical method for the computation of incompressible flows to the compressible flow case. Obviously, this gives the best prospects for handling the limit  $M \downarrow 0$ , assuming that in this limit a well-proven incompressible flow scheme is recovered. With a nonstaggered scheme this has been done by Demirdžić et al. [16]. A staggered grid was first used to compute compressible flows by Harlow and Amsden [21, 22], generalizing the MAC scheme of Harlow and Welch [23] to the compressible flow case, in orthogonal coordinates. Later works in this direction, using general coordinates, are [32, 31, 34, 63, 65, 66]. This is also the approach taken by us here. Staggered schemes have not caught on for compressible flows, because they seem to offer no advantage over nonstaggered schemes, and are more complicated to implement accurately in general coordinates. However, for incompressible flows they are attractive, because no artificial measures need to be taken to avoid spurious pressure oscillations, and the physical boundary conditions suffice. Furthermore, for the incompressible flow case, recently staggered discretizations in general coordinates have appeared; some references, apart from those just quoted, are: [15, 30, 39, 59, 69, 83, 92, 93]. Given an accurate staggered scheme in general coordinates, inclusion of compressibility is quite feasible along the lines already laid out by Harlow and Amsden. Inclusion of accurate and efficient time discretization is in fact easier than for nonstaggered schemes, because there are no artificial regularizing terms. Furthermore, as some of the test cases to be described show, accuracy and efficiency of a staggered scheme turn out to compare quite well with standard schemes in the fully compressible flow case.

## 1.2 Scope of this study

Here we will generalize the staggered scheme for incompressible flows in general coordinates described in [83, 92, 93] to the nonstationary compressible flow case. We specialize to the Euler equations, because viscosity plays no role in the difficulties associated with  $M \downarrow 0$ . Generalization to Navier-Stokes is straightforward. Compared

to the earlier work quoted above, we unify the following two existing methodologies, combining their advantages:

- a nondimensionalisation similar to that of Shuen et al. [63] that eliminates the singularity associated with  $M \downarrow 0$
- a general coordinate version of the staggered grid method of Harlow and Amsden [21, 22], similar to that of Shyy et al. [65, 66].

Shuen et al. [63] use a colocated scheme for compressible flows extended to weakly compressible flows by preconditioning, falsifying transients, and not allowing to take  $M = 0$ . Shyy [65, 66] does not eliminate the singularity associated with  $M \downarrow 0$ , which we do by our special nondimensionalization. This avoids a difficulty hinted at on p. 203 of Harlow and Amsden [22], where it is advised to work with a scaled variable in solving the pressure equation under certain circumstances, and the stabilizing mass diffusion term used in [22] is not needed here.

We can prescribe the Mach number to be arbitrarily small, including zero, in which case the scheme for the computation of incompressible flows of Harlow and Welch [23] (in orthogonal coordinates) or that of [83, 92, 93] (in general coordinates) is recovered. Moreover, temporal accuracy is obtained in a simple manner, without introducing a pseudo-time variable and dual time stepping, as required in many of the works quoted above. Finally, we demonstrate surprisingly good performance of the scheme in the fully compressible case.

Tests will show that an accurate solution can be computed in a limited time with a Mach number independent convergence rate. This will be done for a notorious academic test example, the strongly converging/diverging nozzle. Furthermore, it will be shown that the method, which consists of a combination of compressible and incompressible numerical techniques, works for both fully compressible and fully incompressible flow too. Our method will compute flow through a channel with a bump with a reference Mach number equal to 0 up to 1.65. In the last case shocks will be computed as accurately as methods with a comparably accurate discretisation. In order to show that for fully compressible nonstationary flows the present staggered scheme is as accurate as colocated compressible schemes, results for various Riemann problems, with shocks, expansion waves, and contact discontinuities are shown as well. Finally, the method will be used to compute two applications: flow around an airfoil and flow in an industrial blower configuration.

### 1.3 Outline of this thesis

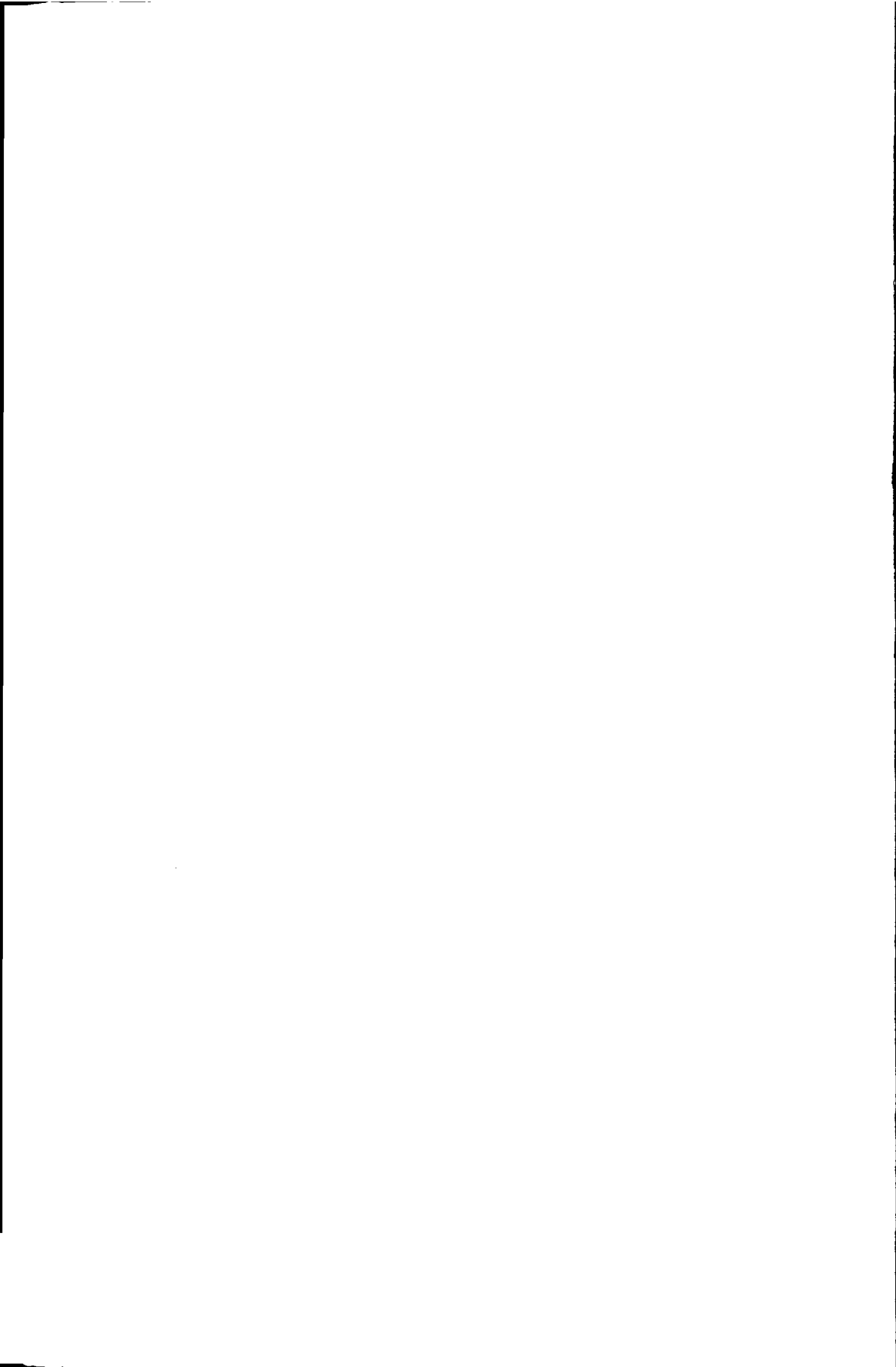
This thesis is divided into three parts: difficulties with standard methods, the present method and results obtained with the present method.

Various difficulties that arise with the computation of compressible flows with low Mach numbers are identified in Chapter 2. Chapter 3 lists the major types of existing methods and discusses their advantages and disadvantages. This is the end of part one. The building blocks of the present method are the subject of the second part, which is divided into four chapters. One on the non-dimensionalisation of the Euler equations, Chapter 4; one on the discretisation of these equations, Chapter 5; one on the solution of the discretized equations, Chapter 6; and one on extension to the Navier-Stokes equations, Chapter 7. In the third and last part results obtained with the present method are shown. Chapter 8 treats low Mach number test problems, where the accuracy of the solution is judged by comparison with results from the literature, and efficiency is measured by comparing the computational times for several inlet Mach numbers. That fully compressible flow, including shocks, can be computed satisfactorily on staggered grids is shown in Chapter 9. In Chapter 10 results are shown for two applications: flow around an airfoil and flow in a blower configuration used to stretch and transport fibers at AKZO Nobel. Finally, concluding remarks and suggestions for further research are collected in Chapter 11.

A synopsis of our method has appeared in [10]. Further publications about our research are [6, 7, 8, 9, 5, 10].

**Part I**

**Difficulties associated with standard  
methods**



## 2

# Relation between compressible and incompressible flow

Flows of gases, as well as those of liquids, are frequently incompressible. The layman is usually surprised to learn that the pattern of flow of air can be similar to that of water. Nevertheless, we can have an incompressible flow of a gas that is easily compressed. A flow is said to be incompressible when the density of a fluid particle does not change. When certain conditions concerning heat transfer and the time scale of the flow are satisfied, a flow is incompressible when  $M = \frac{|u|}{a} \ll 1$ , which means that the speed of the flow  $|u|$  is small compared to the speed of sound in the flow  $a$ . The speed of sound indicates to what extent the pressure is unable to affect the density. For example in liquids, where the speed of sound is high, the density is almost independent of the pressure, while in gases, which have smaller speeds of sound than liquids, the density depends more strongly on the pressure. When the Mach number in a non-stratified flow is uniformly low, that is  $M \lesssim 0.3$ , and there is no heat addition, the density is almost constant and the incompressible flow equations are employed. When, on the other hand, there are also medium or high Mach number flow regions or when there is strong heat addition, the compressible flow equations are needed to adequately model the flow.

In this chapter, after the equations for general flows are described, the mathematical definition of incompressible flow will be given. From this definition the main criterion for incompressible flow:  $M \ll 1$  will be derived. In addition, it will be shown that certain conditions concerning heat transfer must be satisfied.

## 2.1 Equations governing flow of Newtonian fluids

After a description of the equations governing the compressible flow of general Newtonian fluids, the equations for isentropic flow will be derived.

### The compressible flow Navier-Stokes equations

In general, flow of Newtonian fluids is governed by the Navier-Stokes equations. These

express the conservation of mass, momentum and energy. For the present analysis we will use the non-conservation formulation. For the derivation of the computational method in Chapter 5, on the other hand, we will use the conservation form. The equation for conservation of mass can be written as

$$\frac{1}{\rho} \frac{D\rho}{Dt} + \nabla \cdot \mathbf{u} = 0. \quad (2.1)$$

Conservation of momentum is described by

$$\rho \frac{Du_\alpha}{Dt} = \rho f_\alpha - \frac{\partial p}{\partial x_\alpha} + \frac{\partial \tau_{\alpha\beta}}{\partial x_\beta}, \quad (2.2)$$

where  $f_\alpha$  are the external volume forces; furthermore, for so-called Newtonian fluids the shear stress  $\tau_{\alpha\beta}$  is defined by

$$\tau_{\alpha\beta} = \left\{ 2\mu(e_{\alpha\beta} - \frac{1}{3}\delta_{\alpha\beta}\Delta) \right\}, \quad (2.3)$$

where  $\delta_{\alpha\beta}$  is the Kronecker delta,  $e_{\alpha\beta}$  is the rate of strain tensor defined by

$$e_{\alpha\beta} = \frac{1}{2} \left\{ \frac{\partial u_\alpha}{\partial x_\beta} + \frac{\partial u_\beta}{\partial x_\alpha} \right\}, \quad (2.4)$$

and  $\Delta = e_{\alpha\alpha} = \nabla \cdot \mathbf{u}$ . The entropy  $s$  is defined by specifying its variation with internal energy and density:

$$T\delta s = \delta e + p\delta\left(\frac{1}{\rho}\right). \quad (2.5)$$

For a calorically perfect gas the internal energy  $e$  depends on  $T$  only, according to the caloric equation of state:

$$e = c_v T, \quad (2.6)$$

where  $c_v$  is the specific heat at constant volume. The equation for conservation of energy can be written in the following form:

$$T \frac{Ds}{Dt} = \frac{1}{\rho} \Phi + \frac{1}{\rho} \nabla \cdot (k \nabla T) + q. \quad (2.7)$$

Here  $\Phi$  is the rate of dissipation of mechanical energy due to shear viscosity defined by

$$\Phi = 2\mu(e_{\alpha\beta}e_{\alpha\beta} - \frac{1}{3}\Delta^2), \quad (2.8)$$

and  $q$  is the heat release rate. The molecular transport coefficients  $\mu$  and  $k$ , the dynamic viscosity and heat conductivity, respectively are functions of the local state of the fluid. With  $\rho$  and  $T$  as convenient choices of the two variables of state, we have

$$\mu \equiv \mu(\rho, T), \quad k \equiv k(\rho, T). \quad (2.9)$$



Applying (2.5) to a material particle gives

$$T \frac{Ds}{Dt} = \frac{De}{Dt} - \frac{p}{\rho^2} \frac{D\rho}{Dt}, \quad (2.10)$$

which can be rewritten with (2.1) into

$$T \frac{Ds}{Dt} = \frac{De}{Dt} + \frac{p}{\rho} \nabla \cdot \mathbf{u}. \quad (2.11)$$

Hence, the energy equation (2.7) can be rewritten into

$$\frac{De}{Dt} = -\frac{p}{\rho} \nabla \cdot \mathbf{u} + \frac{1}{\rho} \Phi + \frac{1}{\rho} \nabla \cdot (k \nabla T) + q. \quad (2.12)$$

Equations (2.1), (2.2), and (2.12) contain  $\mathbf{u}$ ,  $\rho$ ,  $p$ ,  $T$  and  $e$  as unknown dependent variables, and two further scalar equations are needed to make possible the determination of the flow field. These additional relations are provided by two equations of state, the caloric equation of state, as shown in (2.6), and the thermal equation of state, which may be written generally as

$$\rho = f(p, T). \quad (2.13)$$

For a perfect gas the thermal equation of state is:

$$\rho = \frac{p}{RT}, \quad (2.14)$$

with  $R = c_p - c_v$ , and  $c_p$  and  $c_v$  the constant specific heat at constant pressure and velocity respectively.

### Isentropic flow

In the derivation of the conditions for incompressible flow in the next section we will use the simpler equations for adiabatic inviscid non-heat-conducting ( $q = \mu = k = 0$ ) flow. The energy equation (2.7) shows that in these circumstances  $\frac{Ds}{Dt} = 0$ , and the flow is said then to be isentropic. The simplifying feature of isentropic flow is that exchanges between the internal energy and other forms of energy are reversible. Taking  $p$  and  $s$  as our independent variables the mass conservation equation (2.1) for isentropic flow becomes:

$$\frac{1}{a^2} \frac{Dp}{Dt} + \rho \nabla \cdot \mathbf{u} = 0, \quad (2.15)$$

where we define

$$a^2 = \left( \frac{\partial p}{\partial \rho} \right)_s, \quad (2.16)$$

where the subscript  $s$  indicates that  $s$  is to be kept constant. Note that  $(\partial p / \partial \rho)_s > 0$  because increasing  $p$  (compression) gives increasing  $\rho$ . Because  $\mu = 0$  in isentropic flow, conservation of momentum is described by the inviscid momentum equation:

$$\rho \frac{D\mathbf{u}}{Dt} = -\nabla p + \rho \mathbf{f}. \quad (2.17)$$

The equation of state for isentropic flow of a perfect gas is:

$$\frac{\rho^\gamma}{p} = \frac{\rho_0^\gamma}{p_0} = \text{constant}, \quad (2.18)$$

with  $\gamma = c_p / c_v = \text{constant}$ .

## 2.2 Definition of incompressible flow

The term incompressible flow is applied to any situation where changes in the density of a fluid particle are negligible. The term fluid particle refers in a loose sense to an infinitesimal part of the fluid. A mathematical definition of incompressible flow is:

$$\frac{1}{\rho} \frac{D\rho}{Dt} = 0. \quad (2.19)$$

From the continuity equation we have

$$\frac{1}{\rho} \frac{D\rho}{Dt} = -\nabla \cdot \mathbf{u}. \quad (2.20)$$

This shows that an equivalent definition is that  $\nabla \cdot \mathbf{u} = 0$  (the rate of expansion is zero). Notice that particles in an incompressible flow do not have to have the same density. The only requirement is that the density of each particle remains unchanged. In some cases - for example, the ocean, where salinity and temperature are functions of depth - the density of adjacent particles is different, but any one particle has constant density. These *stratified* flows constitute a separate branch of fluid mechanics and will not be studied in this thesis.

## 2.3 Conditions for incompressible flow

The flow may be regarded as incompressible when  $\frac{1}{\rho} \frac{D\rho}{Dt}$  is small enough, that is if:

$$\left| \frac{1}{\rho} \frac{D\rho}{Dt} \right| \ll \frac{U}{L}, \quad (2.21)$$

with  $L$  and  $U$  characteristic length and velocity scales of the flow. We choose the density and the entropy as independent thermodynamic variables, in which case the rate of change of pressure experienced by a material element can be expressed as:

$$\frac{Dp}{Dt} = \left( \frac{\partial p}{\partial \rho} \right)_s \frac{D\rho}{Dt} + \left( \frac{\partial p}{\partial s} \right)_\rho \frac{Ds}{Dt}. \quad (2.22)$$

With this equation (2.21) is equivalent to:

$$\left| \frac{1}{\rho a^2} \frac{Dp}{Dt} - \frac{1}{\rho a^2} \left( \frac{\partial p}{\partial s} \right)_\rho \frac{Ds}{Dt} \right| \ll \frac{U}{L}. \quad (2.23)$$

This condition will normally be satisfied only if each of the two terms on the left-hand side has a magnitude small compared to  $\frac{U}{L}$ , and we proceed to examine these subsidiary conditions in turn.

### 2.3.1 Small pressure change $\rightarrow M \ll 1$

From equation (2.22) and (2.23) it follows that when the condition

$$\left| \frac{1}{\rho a^2} \frac{Dp}{Dt} \right| \ll \frac{U}{L} \quad (2.24)$$

is satisfied, the changes in density of a material element due to pressure variations are negligible. We now assume inviscid flow, because normally viscosity does not have a decisive effect on the order of magnitude of pressure variations. Hence we can use the momentum equation (2.17) to obtain:

$$\frac{Dp}{Dt} = \frac{\partial p}{\partial t} + \mathbf{u} \cdot \nabla p = \frac{\partial p}{\partial t} - \frac{1}{2} \rho \frac{D\mathbf{u} \cdot \mathbf{u}}{Dt} + \rho \mathbf{u} \cdot \mathbf{f}. \quad (2.25)$$

Since in general there is no reason why these three terms should balance we obtain the following three conditions for incompressibility:

$$\left| \frac{\mathbf{u} \cdot \mathbf{f}}{a^2} \right| \ll \frac{U}{L}, \quad (2.26)$$

$$\left| \frac{1}{\rho a^2} \frac{\partial p}{\partial t} \right| \ll \frac{U}{L}, \quad (2.27)$$

$$\left| \frac{1}{a^2} \frac{D\mathbf{u} \cdot \mathbf{u}}{Dt} \right| \ll \frac{U}{L}. \quad (2.28)$$

These conditions will be rewritten in order to obtain conditions that are easier to work with.

(i) We start with the first condition (2.26). If we regard the body force as arising from gravity this condition becomes  $\frac{gU}{a^2} \ll \frac{U}{L}$ , so that

$$\frac{gL}{a^2} \ll 1. \quad (2.29)$$

For the case of air we can use the isentropic equation of state (2.18) to find

$$\frac{gL}{a^2} = \frac{\rho g L}{\gamma p}. \quad (2.30)$$

This shows that the condition (2.29) is satisfied provided the difference between the static fluid pressures at two points at vertical distance  $L$  apart is a small fraction of the absolute pressure. This means that the condition is satisfied provided the length scale  $L$ , characteristic of the velocity distribution, is small compared with  $p/\rho g$ , the scale-height of the atmosphere, which is about 8.4 km for air under normal conditions. It is evident that this condition will be satisfied for all motions occurring in the laboratory or in layers of the atmosphere not exceeding a few hundred metres in depth.

(ii) Next the second condition for incompressible flow (2.27) is considered. The magnitude of the term  $|\frac{1}{\rho a^2} \frac{\partial p}{\partial t}| = \frac{1}{\rho a^2} |\frac{\partial p}{\partial t}|$  depends directly on the unsteadiness of the flow. In our analysis we therefore need the typical time scale of the flow:  $\tau$ . There are two causes for the pressure variations to be estimated: a) change in momentum, described by the momentum equation, or b) global compression, described by the equation of state.

To begin with a), the magnitude of pressure that follows from the momentum equation is  $\frac{\rho U L}{\tau}$ . The magnitude of  $\frac{\partial p}{\partial t}$  is then  $\frac{\rho U L}{\tau^2}$ , and the condition that  $\frac{1}{\rho a^2} |\frac{\partial p}{\partial t}|$  be small compared with  $\frac{U}{L}$  is

$$\frac{L^2}{a^2 \tau^2} \ll 1, \quad (2.31)$$

hence

$$\frac{1}{\tau} \ll \frac{a}{L}. \quad (2.32)$$

If the representative time scale is  $L/U$ , this condition reduces to  $U/a \ll 1$ , the condition (2.35) that will also be derived from the third incompressibility condition (2.28). But (2.32) is more exacting than (2.35) in cases in which  $\tau \ll L/U$ . In acoustics the representative time scale is  $L/a$ , and (2.32) is not satisfied, corresponding to the fact that compressibility cannot be irrelevant to the flow due to passage of a sound wave.

Considering isentropic global compression, that is case b), the magnitude of pressure variations from the equation of state is  $a^2 \rho$ . Hence,  $\frac{1}{\rho a^2} |\frac{\partial p}{\partial t}|$  is of the order  $1/\tau$ , so that the second incompressibility condition (2.27) becomes:

$$\frac{1}{\tau} \ll \frac{U}{L}. \quad (2.33)$$

This means that the time scale associated with global compression, such as may be caused by a shrinkage of a closed flow domain, must be much larger than  $L/U$ .

(iii) Last, in the third condition (2.28) we have  $D(\mathbf{u} \cdot \mathbf{u})/Dt = \partial(\mathbf{u} \cdot \mathbf{u})/\partial t + u^\alpha \partial(\mathbf{u} \cdot \mathbf{u})/\partial x^\alpha$ . The order of magnitude of these terms is  $U^2/\tau$  and  $U^3/L$ , respectively. Hence (2.27) gives the following two conditions:

$$\frac{UL}{a^2 \tau} \ll 1, \quad (2.34)$$

$$\frac{U^2}{a^2} \ll 1. \quad (2.35)$$

Equation (2.34) is not independent, but follows from (2.32) and (2.35) (which give  $(UL/a^2\tau)^2 \ll 1$ ). In a steady flow, or one in which temporal rates of change do not play a dominant part, a change in speed of a fluid element from zero to  $U$  requires a pressure variation of order  $\rho U^2$ , and so  $\delta\rho/\rho$ , or  $\delta p/\rho a^2$  is small compared with unity when  $\frac{U^2}{a^2} \ll 1$ ; this is the informal argument underlying (2.35). The ratio  $\frac{U}{a}$  is termed the *Mach number* of the flow field for which  $U$  and  $a$  are representative parameters. The Mach number plays an important role in the dynamics of gases. For air at  $15^\circ\text{C}$  and one atmosphere pressure,  $a = 340.6\text{m/s}$ , and for water at  $15^\circ\text{C}$ ,  $a$  is about  $1470\text{m/s}$ , depending on the amount of dissolved air. It is to be expected that the flow due to bodies moving steadily through the atmosphere at speeds below  $50\text{m/s}$  will show little, if any, effect of compressibility of the air, and that normal steady flows in water are most unlikely ever to be influenced by compressibility of the medium.

In conclusion, the first conditions for incompressibility (without entropy variations taken into account) can be written as

$$\frac{1}{\tau} \ll \frac{a}{L}, \quad (2.36)$$

and

$$M \ll 1. \quad (2.37)$$

The first condition limits the frequency of unsteady phenomena in the flow; the second limits the magnitude of the velocity in the flow.

### 2.3.2 Small entropy change $\rightarrow$ small heat release

We now return to (2.23) and consider the second subsidiary condition for the flow to be incompressible:

$$\left| \frac{1}{\rho a^2} \left( \frac{\partial p}{\partial s} \right)_\rho \frac{Ds}{Dt} \right| \ll \frac{U}{L}. \quad (2.38)$$

Since there is a single functional relationship between  $p$ ,  $s$  and  $\rho$  when the fluid is homogeneous, as we assume to be the case, we can write

$$\frac{1}{\rho a^2} \left( \frac{\partial p}{\partial s} \right)_\rho = -\frac{1}{\rho a^2} \left( \frac{\partial p}{\partial \rho} \right)_s \left( \frac{\partial \rho}{\partial s} \right)_p = \quad (2.39)$$

$$-\frac{1}{\rho} \left( \frac{\partial \rho}{\partial s} \right)_p = -\frac{1}{\rho} \frac{(\partial \rho / \partial T)_p}{(\partial s / \partial T)_p} = \frac{\beta T}{c_p}, \quad (2.40)$$

with  $c_p$  the specific heat at constant pressure, and  $\beta$  the thermal compressibility coefficient:

$$c_p = T \left( \frac{\partial s}{\partial T} \right)_p, \quad \beta = -\frac{1}{\rho} \left( \frac{\partial \rho}{\partial T} \right)_p. \quad (2.41)$$

Substitution for  $Ds/Dt$  from the energy equation (2.7) gives

$$\left| \frac{\beta}{c_p} \left\{ \frac{1}{\rho} \Phi + \frac{1}{\rho} \frac{\partial}{\partial x_i} \left( k \frac{\partial T}{\partial x_i} \right) + q \right\} \right| \ll \frac{U}{L}, \quad (2.42)$$

the essential meaning of which is that variations of density of a material element due to internal dissipative heating or due to molecular conduction of heat into the element must be small.

We suppose that the effect of spatial differentiation of a quantity is to change its general magnitude by a factor  $L^{-1}$ , and that the three terms on the left-hand side of (2.42) do not cancel at all points of the flow field. Then it follows from the expression for  $\Phi$  (2.8) that (2.42) is equivalent to the following three conditions

$$\frac{\beta U^2}{c_p} \frac{\mu}{\rho LU} \ll 1, \quad \beta \theta \frac{\kappa}{LU} \ll 1, \quad \frac{\beta}{c_p} |q| \ll 1 \quad (2.43)$$

where  $\kappa = k/\rho c_p$  is the thermal diffusivity,  $\theta$  is a measure of the magnitude of temperature differences in the fluid, and  $\beta$  has been assumed to be positive. For adiabatic flow  $q = 0$ , so that the third condition is satisfied. An indication of the circumstances in which the other conditions (2.43) are satisfied is provided by the following numbers from Batchelor [4] for air and water at  $15^\circ\text{C}$  and one atmosphere pressure. In a case in which  $L = 0.1$  m,  $U = 0.1$  m/s,  $\theta = 10^\circ\text{C}$ :

	$\frac{\beta U^2}{c_p} \frac{\mu}{\rho LU}$	$\beta \theta \frac{\kappa}{LU}$
air	$5 \times 10^{-10}$	$7 \times 10^{-4}$
water	$4 \times 10^{-13}$	$3 \times 10^{-7}$

Clearly, the first two conditions of 2.43 are amply satisfied under these circumstances. These conditions can be formulated in terms of the Mach, Reynolds, and Prandtl numbers as follows. For a perfect gas we have  $a^2 = \gamma RT$ , so that  $\beta = \gamma R/a^2$ , and the first condition can be rewritten as

$$\frac{(\gamma - 1)M^2}{Re} \ll 1, \quad M = U/a, \quad Re = \frac{\rho UL}{\mu}. \quad (2.44)$$

One has to keep in mind that in this estimate  $Re$  should be based on the relevant physical length scale, which may be small, such as a boundary layer thickness, but nevertheless it is hard to think of circumstances in which 2.44 is violated. For a perfect gas,  $\beta = 1/T$ , so that the second condition of (2.43) can be rewritten as

$$\frac{\theta}{T} \frac{1}{Pr Re} \ll 1, \quad Pr = \frac{\mu c_p}{\kappa}, \quad (2.45)$$

where  $Pr$  is called the Prandtl number. This condition may be violated when the temperature differences are large and  $Re$  is small. This is unusual, because under terrestrial circumstances free convection occurs, driving up the Reynolds number.

In practice the most important condition for incompressible flow is  $M \ll 1$ , (2.37). When the Mach number in a non-stratified flow is uniformly low, that is  $M \leq 0.3$ , and there is no heat addition, the density is assumed to be constant and the incompressible flow equations are employed. These are given by:

$$\frac{\partial u_\alpha}{\partial x_\alpha} = 0, \quad (2.46)$$

$$\rho \frac{Du_\alpha}{Dt} = \rho f_\alpha - \frac{\partial p}{\partial x_\alpha} + \frac{\partial \tau_{\alpha\beta}}{\partial x_\beta}, \quad (2.47)$$

with  $\tau_{\alpha\beta}$  the shear stress, which is for incompressible flow equal to:

$$\tau_{\alpha\beta} = \mu \left\{ \frac{\partial u_\alpha}{\partial x_\beta} + \frac{\partial u_\beta}{\partial x_\alpha} \right\}. \quad (2.48)$$

When, on the other hand, there are also medium or high Mach number regions or when there is significant heat addition, the compressible flow equations are needed to adequately model the flow. In the next section the relation between the compressible and the incompressible equations will be discussed.

## 2.4 Asymptotic expansion for $M \downarrow 0$

In this section we will explore the relation between the low Mach number equations and the incompressible flow equations. The low Mach number flow equations are the equations that arise by taking the zero Mach number limit of the compressible flow Navier-Stokes equations. This will be done through a single space, multiple time scale asymptotic expansion of the variables in terms of the global characteristic Mach number  $M$ , see also Müller [48]. Other asymptotic approaches have been presented by: Klainerman and Majda [35, 36], Klein [37], Kreiss, Lorenz and Naughton [40] and Majda [43]. It will be shown that in the limit  $M \downarrow 0$  the compressible flow equations do not converge to the incompressible equations, where constant density is assumed, but to the incompressible equations plus an acoustic field, plus expressions for the heat release rate and global pressure time change. This could be expected from Section 2.3, since there not one, but three conditions for incompressible flow were obtained.

First, the asymptotic low Mach number equations, including acoustics, will be derived. For a comparison with the incompressible flow equations the acoustic effects are eliminated, giving us the same results as a single space, single time scale approach would have given. Finally, the relation between the pressure in low Mach number flows and the pressure in medium and high Mach number flows is discussed.

### 2.4.1 Expanded variables in the flow equations

After a nondimensionalisation, each variable is expanded into an asymptotic power series in the Mach number. Thereafter, a single space, multiple time scale asymptotic analysis is performed.

#### Non-dimensionalisation

First, the Navier-Stokes equations (2.1), (2.2), and (2.7) are rewritten, thereafter they are non-dimensionalised. For a calorically perfect gas we have the following equations of state:

$$e = c_v T \quad \rho = \frac{p}{RT}, \quad (2.49)$$

so that  $T \delta s$  is equal to:

$$T \delta s = \delta e + p \delta \left( \frac{1}{\rho} \right) = c_v \delta T - \frac{p}{\rho^2} \delta \rho = c_v \left( \frac{1}{R \rho} \delta p - \frac{p}{R \rho^2} \delta \rho \right) - \frac{p}{\rho^2} \delta \rho = \frac{1}{\gamma - 1} \frac{1}{\rho} \delta p - \frac{\gamma}{\gamma - 1} \frac{p}{\rho^2} \delta \rho. \quad (2.50)$$

Using this expression, and the continuity equation (2.1) the energy equation (2.7) becomes:

$$T \frac{Ds}{Dt} = \frac{1}{\gamma - 1} \frac{1}{\rho} \frac{Dp}{Dt} + \frac{\gamma}{\gamma - 1} \frac{p}{\rho} \nabla \cdot \mathbf{u} = \frac{1}{\rho} \Phi + \frac{1}{\rho} \nabla \cdot (k \nabla T) + q. \quad (2.51)$$

The continuity and momentum equation, (2.1) and (2.2), will be rewritten in their conservation form.

The Navier-Stokes equations (2.1), (2.2), and (2.51) are non-dimensionalised. For this, reference values for the density  $\rho_{\text{ref}}$ , pressure  $p_{\text{ref}}$ , velocity  $u_{\text{ref}}$ , external force  $f_{\text{ref}}$  and length  $l_{\text{ref}}$  are used. (All other dimensions are derived from these; for example, the reference temperature  $T_{\text{ref}}$  follows from  $\rho_{\text{ref}}$  and  $p_{\text{ref}}$  with the equation of state (2.49).) The dimensionless Navier-Stokes equations then become:

$$\frac{\partial \rho}{\partial t} + \nabla \cdot (\rho \mathbf{u}) = 0, \quad (2.52)$$

$$(\rho \mathbf{u})_t + \nabla \cdot (\rho \mathbf{u} \otimes \mathbf{u}) + \frac{1}{M^2} \nabla p = G, \quad (2.53)$$

$$p_t + \mathbf{u} \cdot \nabla p + \gamma p \nabla \cdot \mathbf{u} = Q, \quad (2.54)$$

where  $\otimes$  denotes the tensor product, so that  $\mathbf{u} \otimes \mathbf{u} = u_i u_j$ , and  $G$  is the sum of friction and external forces:

$$G = \frac{1}{Fr_{\text{ref}}^2} \rho \mathbf{f} + \frac{1}{Re_{\text{ref}}} \frac{\partial}{\partial x_\beta} \tau_{\alpha\beta}, \quad (2.55)$$



with  $Re_{\text{ref}} = \frac{\rho_{\text{ref}} u_{\text{ref}} l_{\text{ref}}}{\mu_{\text{ref}}}$  and  $Fr_{\text{ref}} = \frac{u_{\text{ref}}}{\sqrt{f_{\text{ref}} l_{\text{ref}}}}$ . In (2.54)  $Q$  is the sum of heat conduction and heat release rate:

$$Q = \frac{\tilde{M}^2}{Re_{\text{ref}}} (\gamma - 1) \Phi + \frac{1}{Re_{\text{ref}} Pr_{\text{ref}}} \gamma \nabla \cdot (k \nabla T) + (\gamma - 1) \rho q, \quad (2.56)$$

where  $Pr_{\text{ref}} = \frac{c_p \mu_{\text{ref}}}{k_{\text{ref}}}$ ,  $q$  is the dimensionless heat release rate, and  $\Phi$  is given in (2.8). Furthermore,

$$\tilde{M} = \sqrt{\gamma} M, \quad M = \frac{u_{\text{ref}}}{\sqrt{\gamma p_{\text{ref}} / \rho_{\text{ref}}}}. \quad (2.57)$$

We will study the asymptotic properties of (2.52) - (2.54) as  $\tilde{M} \downarrow 0$ .

### Two-variable asymptotic expansion

A fast acoustic time scale

$$\tau = \frac{t_{\text{ref}}}{L / \sqrt{p_{\text{ref}} / \rho_{\text{ref}}}} = \frac{t}{\tilde{M}} \quad (2.58)$$

is introduced. This acoustic time scale corresponds to the time in which a particle moving with the reference speed of sound divided by  $\sqrt{\gamma}$  travels one length scale, whereas the flow time scale,  $L/U$ , corresponds to the time in which a particle with the reference flow speed travels one length scale. We postulate the following two time variable, single space variable asymptotic expansion in  $\tilde{M}$ :

$$p(\mathbf{x}, t, \tau) = p^{(0)}(\mathbf{x}, t, \tau) + \tilde{M} p^{(1)}(\mathbf{x}, t, \tau) + \tilde{M}^2 p^{(2)}(\mathbf{x}, t, \tau) + O(\tilde{M}^3). \quad (2.59)$$

For the other dependent variables similar expressions are introduced. By including  $O(\tilde{M})$  pressure perturbations, acoustic waves are allowed to affect the velocity field to leading order. Note that the time derivative at constant  $\mathbf{x}$  and  $\tilde{M}$  involves the flow time derivative  $\frac{\partial}{\partial t}$  and the acoustic time derivative  $\frac{\partial}{\partial \tau}$ :

$$\frac{\partial p}{\partial t} \Big|_{\mathbf{x}, \tilde{M}} = \left( \frac{\partial}{\partial t} + \frac{1}{\tilde{M}} \frac{\partial}{\partial \tau} \right) \left( p^{(0)} + \tilde{M} p^{(1)} + \tilde{M}^2 p^{(2)} + O(\tilde{M}^3) \right). \quad (2.60)$$

Substitution of the asymptotic expansion (2.59) into (2.52) gives the leading, first and second order continuity equations:

$$\frac{\partial \rho^{(0)}}{\partial \tau} = 0, \quad (2.61)$$

$$\frac{\partial \rho^{(1)}}{\partial \tau} + \frac{\partial \rho^{(0)}}{\partial t} + \nabla \cdot (\rho \mathbf{u})^{(0)} = 0, \quad (2.62)$$

$$\frac{\partial \rho^{(2)}}{\partial \tau} + \frac{\partial \rho^{(1)}}{\partial t} + \nabla \cdot (\rho \mathbf{u})^{(1)} = 0. \quad (2.63)$$

Substitution of the asymptotic expansion (2.59) into (2.53) gives the leading, first and second order momentum equations:

$$\nabla p^{(0)} = 0, \quad (2.64)$$

$$\frac{\partial(\rho \mathbf{u})^{(0)}}{\partial \tau} + \nabla p^{(1)} = 0, \quad (2.65)$$

$$\frac{\partial(\rho \mathbf{u})^{(1)}}{\partial \tau} + \frac{\partial(\rho \mathbf{u})^{(0)}}{\partial t} + \nabla \cdot (\rho \mathbf{u} \otimes \mathbf{u})^{(0)} + \nabla p^{(2)} = G^{(0)}. \quad (2.66)$$

Substitution of the asymptotic expansion (2.59) into (2.54) gives the leading, first- and second order energy equations:

$$\frac{\partial p^{(0)}}{\partial \tau} = 0, \quad (2.67)$$

$$\frac{\partial p^{(1)}}{\partial \tau} + \frac{\partial p^{(0)}}{\partial t} + \mathbf{u}^{(0)} \cdot \nabla p^{(0)} + \gamma p^{(0)} \nabla \cdot \mathbf{u}^{(0)} = Q^{(0)}, \quad (2.68)$$

$$\begin{aligned} \frac{\partial p^{(2)}}{\partial \tau} + \frac{\partial p^{(1)}}{\partial t} + \mathbf{u}^{(1)} \cdot \nabla p^{(0)} + \mathbf{u}^{(0)} \cdot \nabla p^{(1)} + \\ \gamma p^{(1)} \nabla \cdot \mathbf{u}^{(0)} + \mathbf{u}^{(0)} \cdot \nabla p^{(1)} = Q^{(1)}. \end{aligned} \quad (2.69)$$

### Manipulation of the equations

From (2.64) and (2.67) it follows that

$$p^{(0)}(\mathbf{x}, t, \tau) = p^{(0)}(t). \quad (2.70)$$

Furthermore, equation (2.61) gives  $\rho^{(0)}(\mathbf{x}, t, \tau) = \rho^{(0)}(\mathbf{x}, t)$ , so that the first order momentum equation (2.65) can be rewritten as

$$\frac{\partial \mathbf{u}^{(0)}}{\partial \tau} + \frac{1}{\rho^{(0)}} \nabla p^{(1)} = 0. \quad (2.71)$$

With (2.70) the first-order energy equation (2.68) becomes

$$\frac{\partial p^{(1)}}{\partial \tau} + \gamma p^{(0)} \nabla \cdot \mathbf{u}^{(0)} = Q^{(0)} - \frac{dp^{(0)}}{dt}. \quad (2.72)$$

When the divergence of (2.71) multiplied by  $\gamma p^{(0)}$  is subtracted from the acoustic time derivative of (2.72), we get an inhomogeneous linear wave equation:

$$\frac{\partial^2 p^{(1)}}{\partial \tau^2} - \nabla \cdot (a^{(0)2} \nabla p^{(1)}) = \frac{\partial Q^{(0)}}{\partial \tau}, \quad (2.73)$$

with  $a^{(0)2} = \gamma \frac{p^{(0)}(t)}{\rho^{(0)}(\mathbf{x}, t)}$ . Therefore, the first-order pressure  $p^{(1)}$  appears to be related to acoustics.

Equation (2.72) has an interesting consequence for the divergence of the zeroth order velocity:

$$\nabla \cdot \mathbf{u}^{(0)} = \frac{1}{\gamma p^{(0)}} Q^{(0)} - \frac{1}{\gamma p^{(0)}} \left( \frac{dp^{(0)}}{dt} + \frac{\partial p^{(1)}}{\partial \tau} \right). \quad (2.74)$$

This means that the divergence of  $\mathbf{u}^{(0)}$  is affected by heat conduction and heat release, by the change in time of the global pressure and by the acoustic change in time of the first-order pressure. When (2.74) is inserted into the first-order continuity equation (2.62), we get

$$\frac{\partial \rho^{(0)}}{\partial t} + \mathbf{u}^{(0)} \cdot \nabla \rho^{(0)} = -\frac{1}{a^{(0)2}} Q^{(0)} + \frac{1}{a^{(0)2}} \frac{dp^{(0)}}{dt} + \frac{\partial}{\partial \tau} \left( \frac{p^{(1)}}{a^{(0)2}} - \rho^{(1)} \right). \quad (2.75)$$

From this we can conclude that the zeroth order density of a fluid particle is changed by heat conduction and heat release, by the change in time of the global pressure and by the acoustic change in time of the first-order entropy, given by  $\frac{p^{(1)}}{a^{(0)2}} - \rho^{(1)}$ . Furthermore, since for a fully incompressible flow  $\nabla \cdot \mathbf{u} = 0$ , and since there is no generic reason for the different terms to cancel, it follows that in incompressible flow:

$$Q^{(0)} = \frac{dp^{(0)}}{dt} = \frac{\partial}{\partial \tau} \left( \frac{p^{(1)}}{a^{(0)2}} - \rho^{(1)} \right) = 0. \quad (2.76)$$

This is consistent with the conditions for incompressible flow that were derived in Section 2.3. There it was shown that in order to have incompressible flow 1) the heat release rate should be small, corresponding to  $Q^{(0)} = 0$ , 2) global compression should take place at a much smaller rate than the flow time scale, corresponding to  $\frac{dp^{(0)}}{dt} = 0$ , and 3) acoustic effects should be absent, corresponding to the last equality of equation (2.76).

## 2.4.2 Low Mach number flow versus incompressible flow equations

In this section it will be shown that the low Mach number flow equations, that is the equations for the leading terms in our asymptotic expansion, are equal to the incompressible flow equations, except for heat release rate and global pressure time change, which are not modelled in the incompressible flow equations.

### Low Mach number flow equations with acoustics removed

Now, acoustic effects are removed from the first order continuity and energy equation, (2.62) and (2.68), and from the second order momentum equation (2.66). For this removal of acoustics there are two ways. The first possibility is to separate acoustic and global time scales by integration over the acoustic time  $\tau$  over a period  $T_a$  assuming periodicity in  $\tau$ . For details on this approach see Müller [48] and Klein [37]. The second option is to assume that acoustic waves are not excited by the boundary and initial conditions. This implies that all  $\tau$ -derivatives become zero. In that case, the second order momentum equation (2.66) becomes

$$\frac{\partial \rho^{(0)} \mathbf{u}^{(0)}}{\partial t} + \nabla \cdot (\rho^{(0)} \mathbf{u}^{(0)} \otimes \mathbf{u}^{(0)}) + \nabla p^{(2)} = \mathbf{G}^{(0)}. \quad (2.77)$$

Similarly, the equation for the divergence of  $\mathbf{u}^{(0)}$  becomes:

$$\nabla \cdot \mathbf{u}^{(0)} = \frac{1}{\gamma p^{(0)}} Q^{(0)} - \frac{1}{\gamma p^{(0)}} \frac{dp^{(0)}}{dt}, \quad (2.78)$$

while the first-order continuity equation (2.75) becomes:

$$\frac{\partial \rho^{(0)}}{\partial t} + \mathbf{u}^{(0)} \cdot \nabla \rho^{(0)} = -\frac{1}{a^{(0)2}} Q^{(0)} + \frac{1}{a^{(0)2}} \frac{dp^{(0)}}{dt}. \quad (2.79)$$

Multiplying this equation by  $T$  an equation for the temperature can be derived using the equation of state  $p^{(0)}(t) = \rho^{(0)}(\mathbf{x}, t)T^{(0)}(\mathbf{x}, t)$  and  $T \frac{\partial p}{\partial t} = \frac{\partial(\rho T)}{\partial t} - \rho \frac{\partial T}{\partial t}$ . This equation for the temperature is:

$$\frac{\gamma}{\gamma-1} \rho^{(0)} \left\{ \frac{\partial T^{(0)}}{\partial t} + \mathbf{u}^{(0)} \cdot \nabla T^{(0)} \right\} - \frac{dp^{(0)}}{dt} = \frac{1}{\gamma-1} Q^{(0)}. \quad (2.80)$$

The low Mach number flow equations of Rehm and Baum [57] consist of (2.79), (2.77) and (2.80), where the global pressure  $p^{(0)}$  can be determined by integrating equation (2.78) over the computational domain, see Müller [48] p. 18. These low Mach number flow equations can be solved to compute low Mach number flows with heat release, for example low Mach number combustion.

The standard incompressible flow equations given in (2.46) and (2.47) arise from the compressible flow equations (2.1)-(2.7) when we assume  $D\rho/Dt = 0$ . Without heat release and heat conduction ( $Q^{(0)} = 0$ ) and without global compression ( $\frac{dp^{(0)}}{dt} = 0$ ), the low Mach number flow equations reduce to the standard incompressible flow equations. Assuming  $\rho^{(0)}$  and  $Q^{(0)}$  to be known, the velocity  $\mathbf{u}^{(0)}$  and the pressure  $p^{(2)}$  in the low Mach number flow equations can be determined from (2.77) and (2.78), analogously to incompressible flow. The low Mach number flow continuity equation (2.79) simply prescribes the advection of the leading order density distribution. The major difference between both systems of equations concerns the divergence of the velocity. In the incompressible flow equations the continuity equation describes the divergence of the velocity to be zero, whereas in the low Mach number flow equations it is the energy equation from which the constraint for  $\nabla \cdot \bar{\mathbf{u}}^{(0)}$  is derived. Furthermore, as stated in Section 2.2, in the low Mach number flow equations  $\nabla \cdot \bar{\mathbf{u}}^{(0)}$  is not necessarily equal to zero, but it depends on the heat conduction and heat release rate  $Q^{(0)}$  and the global pressure time change. This is due to the fact that for a flow to be incompressible also the conditions concerning heat release rate (2.42) and global compression (2.33) need to be satisfied. More details on this can be found in Klein [37].

### 2.4.3 Physical significance of pressure variables

The previous analysis reveals three physically distinct roles for the pressure as: 1) a thermodynamic variable, 2) an acoustic wave amplitude, and 3) the balancing agent for inertial forces guaranteeing compliance with a local divergence constraint, i.e. the pressure in incompressible flows.

Since the zeroth order pressure  $p^{(0)}(t)$  serves as the mean pressure in the energy equation (2.74), it represents the global thermodynamic pressure part. Since  $p^{(1)}(\mathbf{x}, t, \tau)$  is governed by the inhomogeneous wave equation (2.73),  $\bar{M}p^{(1)}(\mathbf{x}, t, \tau)$  can be identified as the acoustic part of the pressure. Since, analogous to incompressible flow, the

second-order pressure  $p^{(2)}(\mathbf{x}, t)$  is the balance-of-forces agent for ensuring compliance with the local divergence constraint (2.74),  $\bar{M}^2 p^{(2)}(\mathbf{x}, t)$  may be called the incompressible flow part of the pressure. For the incompressible flow Euler equations the acoustic time scale  $\tau$  is neglected. As a result  $p^{(1)}(\mathbf{x}, t, \tau)$  loses its function and the momentum and energy equation (2.77) and (2.80) are decoupled. The velocity and pressure can then be determined independently of the temperature.



# 3

## Computations for $M \downarrow 0$ , difficulties and remedies

### 3.1 Computational difficulties when $M \downarrow 0$

The main difficulties that arise when computing low Mach number flow are: bad convergence due to disparity of wave speeds, cancellation due to disparity between mean pressure field and pressure differences, pressure-density decoupling and a singular limit  $M \downarrow 0$ . In this chapter these problems are discussed.

#### 3.1.1 Bad convergence due to disparity of wave speeds

Deteriorating convergence or even breakdown is the major problem in computing flows with low Mach numbers. According to the steady one-dimensional compressible flow Euler equations, information travels at three speeds equal to the eigenvalues of the Jacobian of the flux function, namely  $\lambda_1 = u$ ,  $\lambda_2 = u + a$ , and  $\lambda_3 = u - a$ . Consequently, a disturbance in the flow induces an entropy wave travelling with the speed of convection of the flow,  $u$ , and two acoustic waves with the velocities  $u + a$  and  $u - a$ . For small Mach numbers, the wave speeds are very disparate, hence the system becomes stiff. This can be seen from the ratio between the largest and smallest wave speeds going to infinity when  $M \downarrow 0$ :

$$\frac{u + a}{u} = 1 + \frac{1}{M}. \quad (3.1)$$

As a result the numerical simulation of compressible flows with low Mach numbers is difficult. This is easy to understand for explicit time stepping schemes. For stability the time step must be chosen inversely proportional to the largest wave speed, which is  $|u| + a$ . More precisely, we typically have the following stability condition:

$$\Delta t \leq \nu \frac{\Delta x}{|u| + a}, \quad (3.2)$$

where  $\nu$  is some constant near 1, depending on the time stepping scheme used. However, there also is information transported with the flow velocity  $u$ . For low Mach numbers  $|u| \ll |u| + a$ , so that a fluid particle travels only a small distance during the small time step dictated by (3.2). Hence, thousands of time steps are required to reach steady state. For incompressible flow this difficulty does not exist, since then acoustics is neglected and the time step restriction is less severe than (3.2):

$$\Delta t_{inc} \leq \nu \frac{\Delta x}{|u|}. \quad (3.3)$$

When instead of time stepping to steady state an iterative steady state solver is used, a similar convergence problem appears. For these methods the convergence rate is inversely proportional to the condition number of the discrete system to be solved. Since this condition number for the steady one-dimensional Euler equations is equal to

$$\kappa(\cdot) = \frac{\lambda_{max}}{\lambda_{min}} = \frac{u+a}{u}, \quad (3.4)$$

which tends to infinity for  $M \downarrow 0$ , again convergence will be slow.

### 3.1.2 Cancellation due to disparity between mean pressure field and pressure differences

Next to bad convergence, also loss of accuracy can occur when the Mach number becomes low. As is shown by Sesterhehn and Müller [62, 48], this loss of accuracy is caused by the disparity between variations of quantities and their mean values. Perturbations of the velocity  $u$  by  $\delta u$  induce pressure, temperature and density changes. Since the total enthalpy  $H = \frac{a^2}{\gamma-1} + \frac{1}{2}u^2$  and entropy are constant in steady inviscid one-dimensional flow, the Bernoulli equation yields the following steady pressure change:

$$\frac{\delta p}{p} = -\frac{\rho u \delta u}{p} = -\gamma M^2 \frac{\delta u}{u}. \quad (3.5)$$

For  $M \rightarrow 0$  this ratio tend go to 0. A similar expression can be found for the temperature and density:

$$\frac{\delta T}{T} = \frac{\delta a^2}{a^2} = -\frac{(\gamma-1)u\delta u}{a^2} = -(\gamma-1)M^2 \frac{\delta u}{u}, \quad (3.6)$$

$$\frac{\delta \rho}{\rho} = -M^2 \frac{\delta u}{u}. \quad (3.7)$$

Both ratios will tend to 0 for  $M \rightarrow 0$ . Consequently, for low Mach numbers the pressure, density, and temperature differences are small compared to their mean values. The loss of accuracy is caused by the fact that finite precision computations of small



changes of large quantities lead to cancellation errors. For example, for the computation of the pressure difference:

$$\delta p = (p + \delta p) - p, \quad (3.8)$$

the computer would return:

$$\Delta p = ((p + \delta p)(1 + \epsilon_1) - p)(1 + \epsilon_2) = \delta p \left( 1 + \frac{p + \delta p}{\delta p} \epsilon_1 + \epsilon_2 \right), \quad (3.9)$$

with  $\epsilon_1$  and  $\epsilon_2$  the relative errors due to floating point arithmetic. For  $M \rightarrow 0$  the term  $\frac{p + \delta p}{\delta p}$  goes to infinity, as can be seen from (3.5), so that the error  $\epsilon_1$  is magnified.

### 3.1.3 Weak pressure-density coupling

Another feature to be aware of when computing low Mach number flow is the weak pressure-density coupling, which has consequences for the choice of the primary variables. The definition of incompressible flow is that changes in the density of a fluid particle are negligible, see (2.19). The pressure of fluid particles, on the other hand, still varies in incompressible flow, due to velocity changes, as can be seen from the low Mach number momentum equation (2.77). Hence, the pressure will vary with the same order of magnitude as  $u^2$ . Therefore, for low Mach number flow it is not a good idea to use density as a primitive variable and compute the pressure from the equation of state. In that case we would compute the zeroth order pressure which is not the pressure component we need.

### 3.1.4 Singularity of limit $M \downarrow 0$

Another difficulty is that the equations with the nondimensionalisation usually employed for compressible flows become singular in the limit  $M \downarrow 0$ . This can be seen from the asymptotic analysis of the previous chapter. If we work for low Mach number flow with the standard compressible variables, we will recover in the limit  $M \downarrow 0$  only the zeroth order equations. Hence the momentum equation becomes:  $\nabla p = 0$ , while we need the momentum equation for the 'incompressible' pressure component  $p^{(2)}$ , see (2.77). This can also be seen from the dimensional analysis to be performed in Chapter 5.

## 3.2 Previously proposed remedies and their shortcomings

At present various computational methods for the solution of flows with low Mach numbers can be found in the literature. They can be divided into three groups: 1) methods based on low Mach number asymptotics, 2) methods for compressible flow,

extended to incompressible flow, and 3) methods for incompressible flow, extended to compressible flow. The first type of methods only works for low Mach number flow, while the other two can in principle be used to compute flows at all speeds. In this section these methods will be touched upon.

### 3.2.1 Asymptotic expansion techniques

For low speed variable density flows, asymptotic methods based on series expansion in the Mach number, see Section 2.4.1, have been developed. In these flows the Mach number is low throughout the domain, but the density changes due to heat transfer or acoustics. Merkle and Choi [46] use an asymptotic expansion for the Euler equations in  $M_{\text{ref}}^2$  and solve the zeroth order equations by an implicit method. The result is an approximate set of equations valid only at low Mach numbers. Rapid and uniform convergence rates for Mach numbers between  $10^{-1}$  and  $10^{-5}$  were observed in [46]. With their choice of a power series in  $M_{\text{ref}}$  acoustics was neglected. For applications in combustion, Klein and Munz [37, 38] developed an asymptotic expansion in  $M_{\text{ref}}$  in which the long wave acoustics are present. Other papers describing similar methods are Guerra and Gustafsson [19], Oran and Boris [49], and Majda and Sethian [44]. The major limitation of the asymptotic expansion approach is that it is not valid at moderate and high speeds. These methods are often used for low Mach number combustion.

### 3.2.2 Extension of methods for compressible flows

When the numerical methods originally developed for compressible flows are applied to low Mach number flow, the computational difficulties mentioned in the previous section are encountered. Because large investments have been made in codes for compressible flows, much work has been done to improve the low Mach number behaviour of these codes, most notably to improve the convergence rate, see Section 3.1.1. For this two approaches have been developed: time derivative preconditioning and introduction of artificial compressibility. In both methods the physical acoustic modes are replaced by artificial acoustic modes, so that time-accurate behaviour is destroyed. Time-accuracy can be restored by using a pseudo time variable and a physical time variable, but the computing cost involved is considerable. A survey of these extensions of methods for compressible flows is given in this section.

#### Time derivative preconditioning methods

One approach is to improve the convergence rate of compressible methods at low Mach numbers by rescaling the wave speeds. This is done in preconditioning methods, which involve premultiplication of the time derivative in the governing equations by a matrix. The system of equations to be solved can be denoted by:

$$w_t + f_x + g_y = 0. \quad (3.10)$$

In preconditioning methods the system is replaced by:

$$P^{-1}w_t + f_x + g_y = 0, \quad (3.11)$$

with  $P$  the so-called preconditioning matrix. The choice of  $P$  is crucial, and is the subject of much research. The non-conservative form of (3.11) is

$$P^{-1}w_t + Aw_x + Bw_y = 0. \quad (3.12)$$

Multiplying by  $P$  we rewrite this as:

$$w_t + PAw_x + PBw_y = 0. \quad (3.13)$$

The matrix  $P$  has to be designed in such a way that the eigenvalues of  $P(\omega_1 A + \omega_2 B)$  are closer together than the eigenvalues of the original system. This is achieved by diminishing the acoustic speeds. Note that with (3.11) time accuracy is lost.

For the one-dimensional Euler equations the construction of an effective preconditioning matrix is relatively simple, because the characteristic speeds and directions are known without ambiguity, see Section 3.1.1. For the multi-dimensional equations the situation is much more complicated due to the omni-directional propagation of acoustic information: there is no unique decomposition of the flow field in terms of discrete waves. Consequently, preconditioning methods are not very robust. For some cases a given preconditioner will work, in other cases it may fail. Especially near flow singularities such as sonic and stagnation points these methods are not very reliable. Many researchers have developed preconditioners for various cases, see [11, 14, 18, 63, 71, 72, 76, 79, 86].

#### Artificial compressibility methods

Another possibility is to perturb the equations with artificial compressibility, replacing the physical acoustic modes by artificial acoustic modes [13, 19, 28, 45, 46, 47, 57, 78, 86]. These methods can be written in the form of (3.12). As a consequence, distinction between artificial compressibility and preconditioning methods is not very sharp. In both cases time-accuracy is destroyed, so that for the solution of instationary flows pseudo time-stepping is needed. This means that the system of equations is iterated in pseudotime until a steady state solution is reached at each physical time step, see [55, 63, 28]. Also, very small Mach numbers (less than 0.05, say) usually cannot be handled, or only at increasing expense, and the limit  $M \downarrow 0$  is frequently singular. Such low Mach numbers are a.o. encountered in flows with stagnation points.

#### 3.2.3 Extension of methods for incompressible flows

Alternatively, one may extend an incompressible flow method to the compressible flow case. Obviously, this gives the best prospects for handling the limit  $M \downarrow 0$ , assuming that in this limit a well-proven incompressible scheme is recovered. Methods for

incompressible flow use pressure as a primary variable. These methods are well established, with many variations possible, depending on the choice of the dependent variables and their arrangement, numerical grid, pressure correction algorithm, and differencing schemes. Extensions of these numerical algorithms for incompressible flows towards applicability at all speeds are less numerous in the literature than extensions of compressible methods. In this section an overview of compressible flow extensions of incompressible flow methods is given. These methods are time-accurate, semi-implicit, and the pressure is solved separately. In this way the efficiency problem of Section 3.1.1 is circumvented. First, methods using colocated grids, where all unknowns are located at the same position in grid cells, will be discussed. Then, staggered grid methods, where fluxes and scalars are not located at the same positions in grid cells, see Section 6.2, will be presented.

### Colocated methods

A colocated finite volume approach was followed by Demirdžić et al. [16]. The solution method is an extended SIMPLE method, while the equations are discretised on a colocated grid. In order to avoid spurious pressure oscillations at low Mach numbers pressure weighted interpolation, introduced by Rhie and Chow [58], is employed. Since they opted for SIMPLE, a certain iterative method for stationary flows, in [16] only results for stationary flows are reported. A different iterative solution method with the same discretisation techniques was used by Zhou and Davidson [88] to compute fully compressible stationary flows around airfoils. There are also a few publications on colocated finite element pressure correction methods for compressible flow: Zienkiewicz et al. [89], and Karimian and Schneider [33]; both need special regularising terms to avoid spurious pressure oscillations.

### Staggered methods

Staggered schemes have not caught on for compressible flows, because they seem to offer no advantage over nonstaggered schemes, and are more complicated to implement accurately in general coordinates. However, for incompressible flows they are attractive, because no artificial measures need to be taken to avoid spurious pressure oscillations, and the physical boundary conditions suffice. Furthermore, for the incompressible case, recently staggered discretizations in general coordinates have appeared; some references are: [15, 30, 39, 59, 69, 83, 92, 93].

A staggered grid was first used to compute compressible flows by Harlow and Amsden [21, 22], generalizing the MAC scheme of Harlow and Welch [23] to the compressible flow case, in orthogonal coordinates. Another early extension of an incompressible flow method was proposed by Hirt et al. [27], who used velocity components stored at control volume corners and scalar variables stored at cell centers. Their method suffered from oscillations due to pressure-velocity decoupling. Both Harlow and Welch [23] and Hirt et al. [27] use time-accurate pressure correction solution methods. The later extensions of incompressible flow methods can roughly be divided into those using SIMPLE-like iterative methods for the stationary flow case, and those using pressure

correction formulations for the nonstationary flow case.

A stationary flow method arises from the compressible flow extension of the SIMPLE method, in general curvilinear coordinates done by Shyy and Braaten [65, 66]; the corresponding original method for incompressible flow is described by Shyy and Sun [67]. Also results for the computation of viscous compressible flows were reported for this method in Shyy [64]. Karki and Patankar [34] use a compressible flow form of a SIMPLER method. Their shocks are badly smeared due to excessive numerical dissipation. A pressure correction method for nonstationary flows was used to solve the compressible flow Navier-Stokes equations on a staggered grid by Casulli and Greenspan [12]. They have obtained good results for the von Karman vortex street but do not study the low Mach number regime. Another nonstationary pressure correction method on staggered grids extended to compressible flows is the PISO method by Issa et al. [32, 31].

### The present staggered method

Here we will generalize the incompressible flow staggered scheme in general coordinates described in Zijlema et al. [92, 93] and Wesseling et al. [56, 83] to the nonstationary compressible flow case, also described in Bijl and Wesseling [6, 7, 8, 9, 5, 10]. Compared to the earlier work quoted above, we unify the following two existing methodologies, combining their advantages:

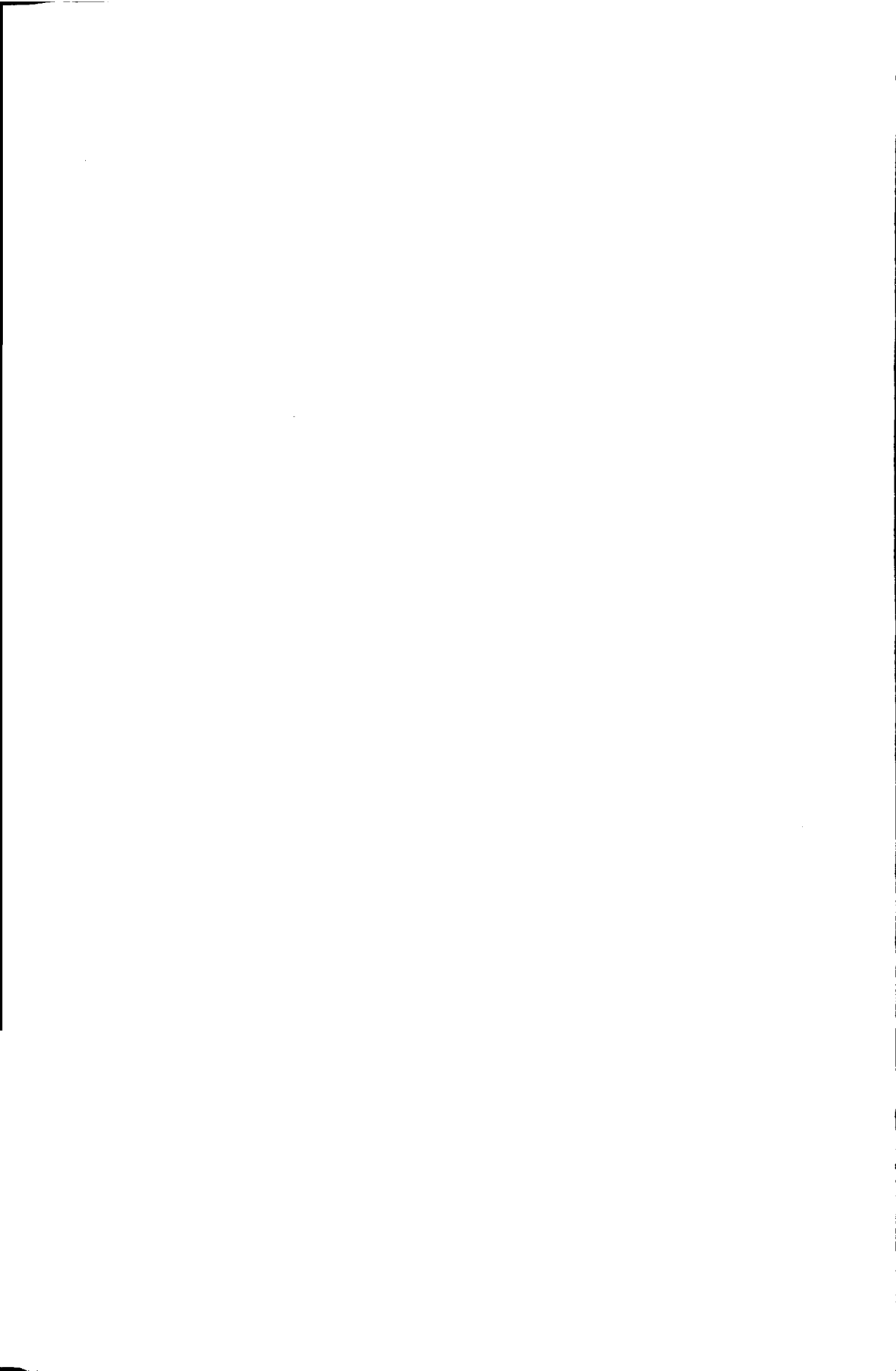
- a nondimensionalisation similar to that of Shuen et al. [63] that eliminates the singularity associated with  $M \downarrow 0$
- a general coordinate version of the staggered grid method of Harlow and Amsden [21, 22].

Shuen et al. [63] use a colocated scheme for compressible flows extended to weakly compressible flows by preconditioning, falsifying transients; it is not allowed to take  $M = 0$ . Harlow and Amsden [21, 22] do not eliminate the singularity associated with  $M \downarrow 0$ , which we will do by a special nondimensionalization. This avoids a difficulty hinted at on p. 203 of Harlow and Amsden [22], where it is advised to work with a scaled variable in solving the pressure equation under certain circumstances, and the stabilizing mass diffusion term used in [22] is not needed here.



## **Part II**

### **The present method**





## 4

# Mach-uniform formulation of the Euler equations

In most standard numerical methods for compressible flows a nondimensionalisation is employed that is appropriate only for flows with medium and high Mach numbers. There the reference pressure is chosen equal to the reference thermodynamic pressure from the equation of state. This choice will be shown to lead to badly scaled equations when the reference Mach number is low. Therefore, we have developed an alternative nondimensionalisation with a reference pressure equal to the reference dynamic pressure and reference values based on stagnation conditions. This choice gives a Mach-uniform formulation of the dimensionless flow equations, so that even when the reference Mach number is equal to zero the equations are well defined. Furthermore, for reasons of accuracy we will work with dimensionless pressure differences, by subtracting a background pressure. With this formulation we will be able to compute fully incompressible flows as well as compressible flows with medium Mach numbers.

In this chapter first the compressible flow equations are made dimensionless using arbitrary reference values. Thereafter it is shown that the standard compressible flow nondimensionalisation does not work when the reference Mach number tends to zero. Finally, the alternative nondimensionalisation is described. This is done for inviscid flow, since viscosity does not influence the difficulty under consideration. In Chapter 7 a straightforward extension to viscous flow is given.

A description of our method has been published in [10].

## 4.1 Dimensionless formulation for arbitrary reference values

Before we go into special choices of reference values to make the compressible Euler equations dimensionless, the formulation for arbitrary reference values is given. We will see that the coefficient  $\frac{p_r}{\rho_r w_r^2}$  reflects the ratio of the inertia term and the pressure gradient in the dimensionless momentum equation.

### Compressible flow Euler equations

For brevity the equations are presented in Cartesian tensor notation, although in fact they are solved in general coordinates, see Chapter 5. The dimensional governing equations to be used are:

$$\frac{\partial \rho}{\partial t} + (\rho u^\alpha)_{,\alpha} = 0, \quad (4.1)$$

$$\frac{\partial \rho u^\alpha}{\partial t} + (\rho u^\alpha u^\beta)_{,\beta} = -p_{,\alpha}, \quad (4.2)$$

$$\frac{\partial h}{\partial t} + u^\alpha h_{,\alpha} = -(\gamma - 1) h u_{,\alpha}^\alpha, \quad (4.3)$$

where  $u^\alpha = u_\alpha$  are the Cartesian velocity components,  $\rho$  is the density,  $p$  is the pressure,  $h$  is the enthalpy, and  $\gamma$  is the ratio of specific heats. The equation of state for a calorically perfect gas completes the system of equations:

$$\rho = \frac{\gamma - p}{\gamma - 1 h}. \quad (4.4)$$

Although a nonconservation form for the energy equation is used, the numerical scheme to be used turns out to converge to genuine weak solutions. The above nonconservation form is merely used for greater efficiency in the pressure correction time stepping scheme to be described, and could be replaced by the conservation form.

### Boundary conditions

The inflow and outflow boundaries are referred to by subscripts  $\infty$  and  $out$ , respectively. When the inflow is subsonic the boundary conditions are:

$$\begin{aligned} u_\infty^\alpha &= \text{a given function, } \alpha = 1, 2, 3 \\ h_\infty &= \text{a given function.} \end{aligned} \quad (4.5)$$

For supersonic inflow all variables should be specified on the inlet boundary so that in addition the pressure at the inflow  $p_\infty$  is given. On solid boundaries the impermeability condition is prescribed:  $u_\alpha n^\alpha = 0$  with  $\mathbf{n}$  the outward normal on the solid wall. At a subsonic outflow boundary the pressure is prescribed:

$$p_{out} = \text{a given function.} \quad (4.6)$$

At a supersonic outflow boundary nothing is prescribed. The initial conditions specify  $p$ ,  $\rho u^\alpha$ , and  $h$ .

### Dimensionless Euler equations for arbitrary reference values

The equations are made dimensionless by scaling the variables by reference quantities  $\rho_r$ ,  $h_r$ ,  $p_r$ ,  $w_r$ , the reference speed and  $L_r$ , the reference length, that still remain to be chosen. The time is made dimensionless by  $L_r/w_r$ . The following dimensionless Euler

equations are obtained:

$$\frac{\partial \rho}{\partial t} + (\rho u^\alpha)_{,\alpha} = 0, \quad (4.7)$$

$$\frac{\partial \rho u^\alpha}{\partial t} + (\rho u^\alpha u^\beta)_{,\beta} + \frac{p_r}{\rho_r w_r^2} p_{,\alpha} = 0, \quad (4.8)$$

$$\frac{\partial h}{\partial t} + u^\alpha h_{,\alpha} = -(\gamma - 1) h u_{,\alpha}^\alpha. \quad (4.9)$$

## 4.2 Breakdown of standard compressible formulation as $M \downarrow 0$

In the standard compressible flow formulation the density is used as primitive variable, and the pressure follows from the equation of state, so, quite naturally, for  $p_r$  the following choice is usually made:

$$p_r = \rho_r R T_r. \quad (4.10)$$

Since  $a^2 = \frac{\gamma p}{\rho}$ , the factor  $\frac{p_r}{\rho_r w_r^2}$  in the dimensionless momentum equation (4.8) becomes:

$$\frac{p_r}{\rho_r w_r^2} = \frac{1}{\gamma M_r^2}. \quad (4.11)$$

Therefore in the incompressible flow limit  $M_r \downarrow 0$  the momentum equations (4.8) degenerate to  $p_{,\alpha} = 0$ . This is exactly the equation for the zeroth order thermodynamical pressure  $p^{(0)}(t)$  in the asymptotic analysis of Section 2.3. As was shown there it is the second-order momentum equation, and not the zeroth order, which converges to the incompressible flow momentum equations when  $M_r \downarrow 0$ .

## 4.3 Alternative non-dimensionalisation, valid for $M \downarrow 0$

Since in the incompressible flow limit the density is independent of the incompressible pressure which balances inertial forces, the pressure field cannot be calculated from the density, and for this reason density-based methods fail. Therefore, a pressure-based formulation will be employed, as in most if not all publications on weakly compressible flows. Furthermore,  $(\rho u)^\alpha$  will be chosen as a basic variable in order to facilitate a straightforward pressure correction formulation in the next section. This means that  $(\rho u)^\alpha$ ,  $p$ , and  $h$  are chosen as unknown variables. The density can be found from pressure and enthalpy by the equation of state.

### 4.3.1 Reference pressure equal to reference dynamic pressure

In order to obtain a Mach-uniform formulation in which the limit  $M \downarrow 0$  is regular, the pressure is made dimensionless in a way that is different from the standard compressible

flow approach discussed in the previous section. In Panton [52] it is shown that the dimensionless pressure gradient is of the same order as the inertia terms if  $p_r$  is equal to  $\rho_r w_r^2$ , that is if the dimensionless pressure is defined to be:

$$p = \frac{p^* - p_c^*}{\rho_r w_r^2}, \quad (4.12)$$

with  $p_c^*$  a constant pressure level still to be chosen. Here and in the following an asterisk denotes a dimensional quantity. A similar dimensionless pressure is introduced by Shuen et al. [63]. This results in the following dimensionless form of the Euler equations:

$$\left(\frac{\partial \rho}{\partial p}\right)_h \frac{\partial p}{\partial t} + \left(\frac{\partial \rho}{\partial h}\right)_p \frac{\partial h}{\partial t} + (\rho u)_{,\alpha}^\alpha = 0, \quad (4.13)$$

$$\frac{\partial(\rho u)^\alpha}{\partial t} + ((\rho u)^\alpha u^\beta)_{,\beta} = -p_{,\alpha}, \quad (4.14)$$

$$\frac{\partial h}{\partial t} + u^\alpha h_{,\alpha} = -(\gamma - 1) h u_{,\alpha}^\alpha. \quad (4.15)$$

Since the reference Mach number  $M_r$  does not occur, the limit  $M_r \downarrow 0$  is obviously regular for this dimensionless system of equations.

The physical significance of the dimensionless pressure  $p$  (4.12) can be found when we return to the asymptotic analysis of Section 2.4. There the dimensional pressure was expanded in the two time scale, single space scale Mach number asymptotic analysis in (2.59). When we assume acoustic effects to be absent from the initial and boundary conditions, the acoustic time scale can be neglected. Since  $p^{(1)}$  was related to acoustics this variable also disappears from the equations. What is left is a single time scale, single space scale asymptotic expansion of the pressure, equal to:

$$p^*(\mathbf{x}, t) = p^{(0)*}(t) + \tilde{M}_r^2 p^{(2)*}(\mathbf{x}, t) + O(\tilde{M}_r^3), \quad (4.16)$$

where also equation (2.70) was used. This expression can be made dimensionless by division by a reference pressure  $p_r$ , which remains to be chosen:

$$p(\mathbf{x}, t) = \frac{p^*(\mathbf{x}, t)}{p_r} = p^{(0)}(t) + \tilde{M}_r^2 p^{(2)}(\mathbf{x}, t) + O(\tilde{M}_r^3), \quad (4.17)$$

where the dimensionless pressure components are equal to  $p^{(i)} = p^{(i)*}/p_r$ . From this follows:

$$p^{(2)} = \frac{p(\mathbf{x}, t) - p^{(0)}(t)}{\tilde{M}_r^2} = \frac{p_r(p^*(\mathbf{x}, t) - p^{(0)*}(t))}{\tilde{M}_r^2} = \frac{p^*(\mathbf{x}, t) - p^{(0)*}(t)}{\rho_r w_r^2}. \quad (4.18)$$

Comparison of (4.12) with (4.18) shows that the dimensionless pressure  $p$  in our method is equal to:

$$p = p^{(2)} + \frac{p^{(0)*}(t) - p_c^*}{\tilde{M}_r^2}. \quad (4.19)$$

From this it can be concluded that  $p = p^{(2)}$  when  $p^{(0)*}(t) = p_c^*$ , that is when the thermodynamic pressure variable  $p^{(0)*}$  is not a function of time, hence when there is no global compression. In that case our dimensionless pressure is exactly equal to the nondimensionalised pressure component  $p$  in the asymptotic analysis, which means that  $p$  balances inertial forces.

### 4.3.2 Reference values equal to stagnation conditions

Reference values based on boundary conditions and reservoir parameters are used. The Mach number at the inlet is defined by:

$$M_\infty = \frac{w_\infty^*}{a_\infty^*}, \quad (4.20)$$

where  $w_\infty^*$  is the velocity of the flow and  $a_\infty^* = \sqrt{(\gamma - 1)h_\infty^*}$  is the speed of sound. The reference quantities are chosen equal to the stagnation condition at the inlet, denoted by subscript 0:

$$h_0^* = \left(1 + \frac{\gamma - 1}{2} M_\infty^2\right) h_\infty^*, \quad (4.21)$$

$$a_0^{*2} = \left(1 + \frac{\gamma - 1}{2} M_\infty^2\right) a_\infty^{*2}, \quad (4.22)$$

$$\rho_0^* = \left(1 + \frac{\gamma - 1}{2} M_\infty^2\right)^{\frac{1}{\gamma - 1}} \rho_\infty^*, \quad (4.23)$$

$$p_0^* = \left(1 + \frac{\gamma - 1}{2} M_\infty^2\right)^{\frac{\gamma}{\gamma - 1}} p_\infty^*. \quad (4.24)$$

The dimensionless variables are defined by:

$$\begin{aligned} x^\alpha &= \frac{x^{\alpha*}}{L^*}, & t &= \frac{t^* w_\infty^*}{L^*}, \\ p &= \frac{p^* - p_{out}^*}{\rho_0^* w_\infty^{*2}}, & h &= \frac{h^*}{h_0^*}, \\ \rho &= \frac{\rho^*}{\rho_0^*}, & u^\alpha &= \frac{u^{\alpha*}}{w_\infty^*}, \quad \alpha = 1, 2, \end{aligned}$$

where we have chosen  $p_c^* = p_{out}^*$ .

### 4.3.3 Dimensionless equations and boundary conditions

The dimensionless Euler equations are presented in (4.13), (4.14), and (4.15). The equation of state (4.4) becomes:

$$\rho = \rho(p, h) = \frac{\gamma M_\infty^2}{1 + \frac{\gamma - 1}{2} M_\infty^2} \frac{p}{h} + \left[ p_v \left( \left(1 + \frac{\gamma - 1}{2} M_\infty^2\right)^{\frac{-\gamma}{\gamma - 1}} - 1 \right) + 1 \right] \frac{1}{h}, \quad (4.25)$$

where  $p_v$  is defined by:

$$p_v = \frac{p_{out}^* - p_0^*}{p_\infty^* - p_0^*}. \quad (4.26)$$

The dimensionless equation of state shows that  $\rho$  becomes independent of  $p$  as  $M_\infty \downarrow 0$ , which is precisely what we want, because this eliminates acoustic modes. Furthermore, in this limit the variation of  $p$  remains  $\mathcal{O}(1)$ . This dimensionless formulation includes the incompressible flow case, which is obtained by putting  $M_\infty = 0$ .

### Boundary conditions

The dimensionless subsonic boundary conditions become:

$$\begin{aligned} (\rho u)_\infty^1 &= \left(1 + \frac{\gamma-1}{2} M_\infty^2\right)^{\frac{-1}{\gamma-1}} \cos \alpha_\infty, \\ (\rho u)_\infty^2 &= \left(1 + \frac{\gamma-1}{2} M_\infty^2\right)^{\frac{-1}{\gamma-1}} \sin \alpha_\infty, \\ h_\infty &= \left(1 + \frac{\gamma-1}{2} M_\infty^2\right)^{-1}, \\ p_{out} &= 0, \end{aligned} \quad (4.27)$$

where  $\alpha_\infty$  is the flow angle at the inlet. For supersonic inflow  $p_\infty$  must also be prescribed. For supersonic outflow  $p_{out}$  is not prescribed.

## 5

# Discretisation of the compressible equations on a staggered grid

The system of dimensionless compressible Euler equations obtained in the previous chapter will now be discretised using a finite-volume technique in general boundary-fitted coordinates on a staggered grid. A staggered grid was chosen since for incompressible flow the differential equations can be discretized on a staggered grid in a straightforward way, and the physical boundary conditions suffice, furthermore, no measures have to be taken to avoid spurious pressure oscillations. The main difference between the present method and methods for the incompressible flow case is that the density is an unknown variable, which results in an extra term in the continuity equation and an extra equation: the equation of state. Our method will be chosen such that as  $M_\infty \downarrow 0$  the classical incompressible flow staggered grid method of Harlow and Welch [23] is recovered. This may be expected to give Mach-independent efficiency and accuracy for small and medium Mach numbers.

In this chapter first the equations are formulated in general coordinates. Thereafter, the mapping from the physical grid to the computational grid and its associated geometric quantities are discussed. This is followed by the finite volume discretisation of the compressible flow Euler equations in general coordinates on a staggered grid. Here, both central and first-order upwind discretisation is presented. In the last section of this chapter, we present the implementation of higher-order upwind methods and density-biased upwinding.

### 5.1 Invariant formulation in general coordinates

To begin with, the governing equations have to be recast in a form in which both independent and dependent variables are invariant with respect to change of coordinates. The compressible Euler equations in Cartesian coordinates, (4.13)-(4.15), are not tensor equations because  $\alpha$  occurs both as a free superscript and a free subscript. Raising subscripts as required by contraction with the metric tensor, see Aris [2], we obtain tensor

equations, which are then valid in general coordinates, according to Ricci's lemma:

$$\left(\frac{\partial \rho}{\partial p}\right)_h \frac{\partial p}{\partial t} + \left(\frac{\partial \rho}{\partial h}\right)_p \frac{\partial h}{\partial t} + (\rho U)_{,\alpha}^\alpha = 0, \quad (5.1)$$

$$\frac{\partial(\rho U)^\alpha}{\partial t} + ((\rho U)^\alpha U^\beta)_{,\beta} = -(g^{\alpha\beta} p)_{,\beta}, \quad (5.2)$$

$$\frac{\partial h}{\partial t} + U^\alpha h_{,\alpha} = -(\gamma - 1)h U_{,\alpha}^\alpha, \quad (5.3)$$

with  $(\rho U)^\alpha = \mathbf{a}^{(\alpha)} \cdot (\rho \mathbf{u})$  the contravariant momentum components, where the covariant and contravariant metric tensors are defined as:

$$g_{\alpha\beta} = \mathbf{a}_{(\alpha)} \cdot \mathbf{a}_{(\beta)}, \quad g^{\alpha\beta} = \mathbf{a}^{(\alpha)} \cdot \mathbf{a}^{(\beta)}, \quad (5.4)$$

respectively, with

$$\mathbf{a}_{(\alpha)} = \frac{\partial \mathbf{x}}{\partial \xi^\alpha}, \quad \mathbf{a}^{(\alpha)} = \nabla \xi^\alpha, \quad (5.5)$$

the covariant and contravariant base vectors with respect to the mapping

$$T : \mathbf{x} = \mathbf{x}(\xi). \quad (5.6)$$

Here,  $\mathbf{x}$  are the Cartesian coordinates in the physical domain  $\Omega$  and  $\xi$  are the boundary-conforming curvilinear coordinates in the rectangular computational domain  $G$ . The mapping is assumed to be regular, i.e. the Jacobian of the transformation, that will be denoted as  $\sqrt{g}$ , does not vanish.

Furthermore, for the covariant derivatives of a first order tensor,  $U^\alpha$ , and a second order tensor,  $T^{\alpha\beta}$ , we have:

$$U_{,\alpha}^\alpha = \frac{1}{\sqrt{g}} \frac{\partial \sqrt{g} U^\alpha}{\partial \xi^\alpha}, \quad U_{,\beta}^\alpha = \frac{\partial U^\alpha}{\partial \xi^\beta} + U^\gamma \left\{ \begin{matrix} \alpha \\ \beta \gamma \end{matrix} \right\}, \quad (5.7)$$

$$T_{,\beta}^{\alpha\beta} = \frac{1}{\sqrt{g}} \frac{\partial \sqrt{g} T^{\alpha\beta}}{\partial \xi^\beta} + T^{\beta\gamma} \left\{ \begin{matrix} \alpha \\ \beta \gamma \end{matrix} \right\}, \quad (5.8)$$

with  $\left\{ \begin{matrix} \alpha \\ \beta \gamma \end{matrix} \right\}$  the Christoffel symbol of the second kind, defined by

$$\left\{ \begin{matrix} \alpha \\ \gamma \beta \end{matrix} \right\} = \mathbf{a}^{(\alpha)} \cdot \frac{\partial \mathbf{a}_{(\gamma)}}{\partial \xi^\beta} = \frac{\partial \xi^\alpha}{\partial x^\delta} \frac{\partial^2 x^\delta}{\partial \xi^\beta \partial \xi^\gamma} = \left\{ \begin{matrix} \alpha \\ \beta \gamma \end{matrix} \right\}, \quad (5.9)$$

see Aris [2] Section 7.5.6 and 8.13.



## 5.2 Staggered grid and associated geometric quantities

In Figure 5.1 a two-dimensional grid cell in the physical domain  $\Omega$  and in the computational domain  $G$  is shown. They are related by the mapping  $T : \mathbf{x} = \mathbf{x}(\xi)$ , where  $\mathbf{x}$  are the Cartesian coordinates in the physical domain  $\Omega$  and  $\xi$  are the boundary-conforming curvilinear coordinates in the computational domain  $G$ . The surface element in physical space  $d\Omega$  is related to the surface element in computational space by

$$d\Omega = \sqrt{g}dG. \quad (5.10)$$

In  $G$  we choose a uniform grid such that the mesh-size  $\Delta\xi^\alpha = 1$ .

### Smoothness of the mapping

The mapping  $\mathbf{x}(\xi)$  is generated numerically for each cell individually. Because grid generation software gives us  $\mathbf{x} = \mathbf{x}(\xi)$  in the cell vertices, it is desirable to characterise a computational grid by the coordinates of the cell vertices only. Hence, we want to allow piecewise bilinear coordinate mappings. This implies that cell vertices are connected by straight lines. As a consequence, grid lines need not to be smooth in the physical domain. Owing to the piecewise bilinear mapping all the geometric quantities, (5.4) - (5.5), are continuous inside a cell. On the other hand, some of these quantities are discontinuous on cell faces. For instance,  $\mathbf{a}_{(\alpha)}$  is constant along  $\xi^\alpha$ -lines but the value of this constant changes from cell to cell. Hence, across cell faces, where  $\xi^\alpha = \text{constant}$ ,  $\mathbf{a}_{(\alpha)}$  jumps. Furthermore,  $\mathbf{a}_{(\alpha)}$  is found to be continuous at  $\xi^\beta = \text{constant}$  ( $\beta \neq \alpha$ ). The smoothness properties of the other geometric quantities follow from those for the covariant base vectors. It appears, for example, that  $\sqrt{g}$  and  $\mathbf{a}^{(\alpha)}$  are discontinuous at cell faces, whereas  $\sqrt{g}\mathbf{a}^{(\alpha)}$  is continuous. The discontinuity of aforementioned quantities can give problems on irregular grids with for example large jumps in grid size. Therefore, an improved discretisation was developed, see [73, 83, 85]. In this thesis the standard discretisation, as explained in this section, is used for most computations. Only for computation of flow around the airfoil the improved version was used. Note that the coordinate mapping is not differentiable.

### Computation of geometric quantities

The geometrical quantities presented in (5.4)-(5.5) are computed by central differences and linear interpolation. The covariant base vectors  $\mathbf{a}_{(\alpha)} = \frac{\partial \mathbf{x}}{\partial \xi^\alpha}$  are calculated in the centers of the edges of a cell  $G_{ij}$ . For example, at the two-dimensional cell edge 43 in Figure 5.1  $\mathbf{a}_{(2)}$  is computed by the difference:

$$\mathbf{a}_{(2)i+1/2,j} = \frac{1}{\Delta\xi^2}(\mathbf{x}_3 - \mathbf{x}_4) = (\mathbf{x}_3 - \mathbf{x}_4), \quad (5.11)$$

which is constant along the edge. Similarly,

$$\mathbf{a}_{(2)i-1/2,j} = (\mathbf{x}_2 - \mathbf{x}_1). \quad (5.12)$$

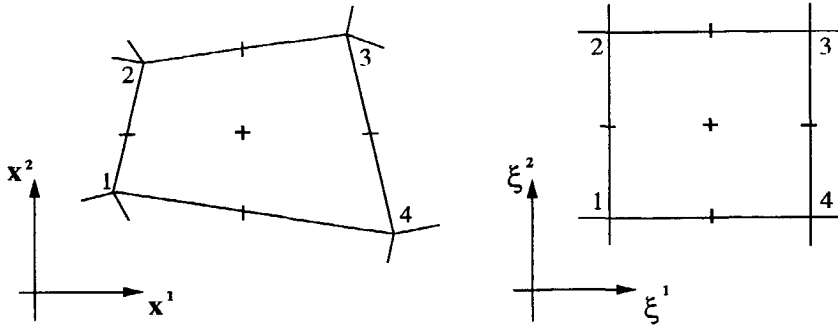


Figure 5.1: Cell in physical domain  $\Omega$ ; its image in the computational domain  $G$  is a square

Equations (5.11) and (5.12) show that  $\mathbf{a}_{(2)}$  is continuous along grid lines  $\xi^1 = \text{constant}$ . The same is true for  $\mathbf{a}_{(1)}$  along grid lines  $\xi^2 = \text{constant}$ . We have, for example,

$$\mathbf{a}_{(1);i,j-1/2} = (\mathbf{x}_4 - \mathbf{x}_1). \quad (5.13)$$

On the other hand,  $\mathbf{a}_{(2)}$  is discontinuous at grid lines  $\xi^2 = \text{constant}$ , and  $\mathbf{a}_{(1)}$  is discontinuous at grid lines  $\xi^1 = \text{constant}$ . In other points than centers of cell edges, i.e. cell centers or cell faces, the covariant base vectors are computed by averaging; for example,

$$\mathbf{a}_{(1);i,j} = \frac{1}{2}(\mathbf{a}_{(1);i,j-1/2} + \mathbf{a}_{(1);i,j+1/2}). \quad (5.14)$$

On faces where covariant base vectors are discontinuous they are defined by taking arithmetic averages of existing base vectors in the following way:

$$\mathbf{a}_{(1);i+1/2,j+1/2} = \frac{1}{4}(\mathbf{a}_{(1);i,j+1/2} + \mathbf{a}_{(1);i+1,j+1/2} + \mathbf{a}_{(1);i,j+1/2} + \mathbf{a}_{(1);i+1,j+1/2}). \quad (5.15)$$

For convenience we define the operator  $\otimes$  by

$$\mathbf{a} \otimes \mathbf{b} = a^1 b^2 - a^2 b^1. \quad (5.16)$$

The Jacobian  $\sqrt{g} = a_{(1)}^1 a_{(2)}^2 - a_{(1)}^2 a_{(2)}^1 = \mathbf{a}_{(1)} \otimes \mathbf{a}_{(2)}$  is computed in cell centres according to:

$$\sqrt{g}_{i,j} = \frac{1}{4\Delta\xi^1\Delta\xi^2}(\mathbf{x}_{34} - \mathbf{x}_{12}) \otimes (\mathbf{x}_{23} - \mathbf{x}_{14}) = (\mathbf{x}_{34} - \mathbf{x}_{12}) \otimes (\mathbf{x}_{23} - \mathbf{x}_{14}), \quad (5.17)$$

where we define  $\mathbf{x}_{mn} = \mathbf{x}_m + \mathbf{x}_n$ . Since  $\mathbf{x}_m \otimes \mathbf{x}_m = 0$  and  $\mathbf{x}_m \otimes \mathbf{x}_n = -\mathbf{x}_n \otimes \mathbf{x}_m$  this can be rewritten as

$$\sqrt{g}_{i,j} = (\mathbf{x}_4 - \mathbf{x}_2) \otimes (\mathbf{x}_3 - \mathbf{x}_1). \quad (5.18)$$

In other points than cell centers the Jacobian is computed with the same averaging processes as the covariant base vectors. Note that  $\sqrt{g}_{i,j}$  is discontinuous at all cell edges. The contravariant base vectors follow from their orthogonality to the covariant base vectors, they are:

$$\mathbf{a}^{(1)} = \frac{1}{\sqrt{g}} \begin{pmatrix} a_{(2)}^2 \\ -a_{(2)}^1 \end{pmatrix}, \quad \mathbf{a}^{(2)} = \frac{1}{\sqrt{g}} \begin{pmatrix} a_{(1)}^2 \\ -a_{(1)}^1 \end{pmatrix}. \quad (5.19)$$

Because  $\sqrt{g}$  is discontinuous at cell edges, so is  $\mathbf{a}^{(\alpha)}$ . The Christoffel symbols, defined in (5.9), are computed by central differences after computing  $\mathbf{a}_{(\alpha)}$  and  $\mathbf{a}^{(\alpha)}$  in the required points.

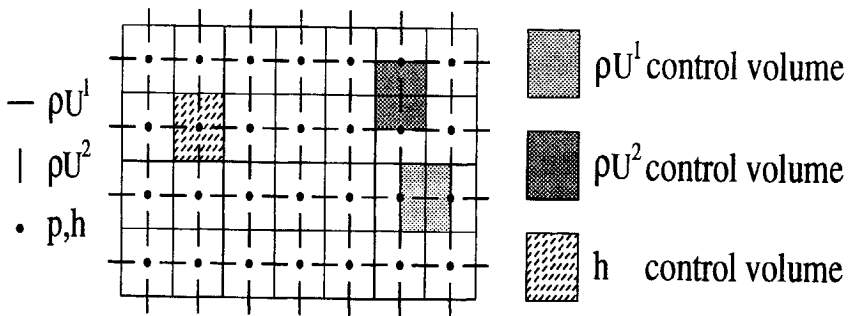


Figure 5.2: Grid in computational domain  $G$

### Grid and control volumes

The computational domain is divided into  $M \times N$  cells in the  $x^1$ - and  $x^2$ -direction respectively. Figure 5.2 shows part of the staggered computational grid, the control volumes and the numbering system. The pressure as well as all other scalars are given in the cell centers  $(i, j)$ , indicated by the symbol  $\bullet$ . The velocity and the momentum component in the  $x^1$ -direction,  $U^1$  and  $(\rho U)^1$ , are given in the centers of cell faces  $(i + 1/2, j)$ , indicated by the symbol  $-$ . The velocity and the momentum component in the  $x^2$ -direction,  $U^2$  and  $(\rho U)^2$ , are given in the centers of cell faces  $(i, j + 1/2)$ , indicated by the symbol  $|$ . The discretization of the system of equations will only be discussed for the interior of the domain. The discretisation of the boundary conditions will not be discussed here, but this is the same as for the incompressible flow equations, discussed in Segal et al. [61], with the only difference that here the momentum components  $(\rho U)^\alpha$  are used instead of the velocity components  $U^\alpha$ . The different control volumes for scalars, used for the continuity and the energy equation, for  $(\rho U)^1$ , used for the first momentum equation, and for  $(\rho U)^2$ , used for the second momentum equation, are shown in Figure 5.2 as well. Discretisation of these equations is obtained by integration over finite volumes, which correspond in the computational grid with the above mentioned control volumes. This is the subject of the following sections, i.e. Section 5.3 to 5.5.

### 5.3 The continuity equation

The continuity equation in the unknowns  $(\rho U)^\alpha$ ,  $p$  and  $h$  as presented in conservative formulation in (5.1) is given by

$$\left(\frac{\partial \rho}{\partial p}\right)_h \frac{\partial p}{\partial t} + \left(\frac{\partial \rho}{\partial h}\right)_p \frac{\partial h}{\partial t} + (\rho U)^\alpha = 0. \quad (5.20)$$

The density  $\rho$  depends on  $p$  and  $h$  through the equation of state (4.25).

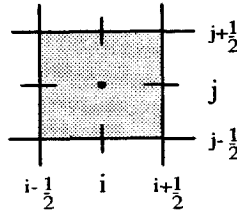


Figure 5.3: Control volume for the continuity equation in the computational domain

#### 5.3.1 Finite volume discretisation

Discretisation of (5.20) is obtained by integration over a finite volume  $G_{i,j}$  with center  $(i, j)$  as indicated in Figure 5.3. Since we have chosen  $\Delta \xi^\alpha = 1$ , we have

$$\begin{aligned} \int_{\Omega_{i,j}} (\rho U)^\alpha d\Omega &= \int_{G_{i,j}} (\rho U)^\alpha \sqrt{g} d\xi^1 d\xi^2 = \\ \int_{G_{i,j}} \frac{\partial \sqrt{g} (\rho U)^\alpha}{\partial \xi^\alpha} d\xi^1 d\xi^2 &= \int_{G_{i,j}} \frac{\partial (\rho V)^\alpha}{\partial \xi^\alpha} d\xi^1 d\xi^2, \end{aligned} \quad (5.21)$$

with  $(\rho V)^\alpha = \sqrt{g} (\rho U)^\alpha = \sqrt{g} \mathbf{a}^{(\alpha)} \cdot \rho \mathbf{u}$  the momentum flux components. Because  $\sqrt{g} \mathbf{a}^{(\alpha)}$  is smooth at cell face  $\xi^\alpha = \text{constant}$ , so is  $(\rho V)^\alpha$ . By partial integration we obtain

$$\begin{aligned} \int_{\Omega_{i,j}} (\rho U)^\alpha d\Omega &= \\ \left\{ \int_{\Gamma_{i+1/2,j}} - \int_{\Gamma_{i-1/2,j}} \right\} \rho V^1 d\Gamma &+ \left\{ \int_{\Gamma_{i,j+1/2}} - \int_{\Gamma_{i,j-1/2}} \right\} \rho V^2 d\Gamma \approx \\ (\rho V)^1 \Big|_{(i-1/2,j)}^{(i+1/2,j)} &+ (\rho V)^2 \Big|_{(i,j-1/2)}^{(i,j+1/2)}, \end{aligned} \quad (5.22)$$

where for the last step the midpoint rule is used. The time derivatives are integrated using the midpoint rule as well:

$$\int_{\Omega_{i,j}} \left(\frac{\partial \rho}{\partial p}\right)_h \frac{\partial p}{\partial t} d\Omega =$$

$$\int_{G_{i,j}} \left( \frac{\partial \rho}{\partial p} \right)_h \frac{\partial p}{\partial t} \sqrt{g} d\xi^1 d\xi^2 \approx \sqrt{g}_{(i,j)} \left( \frac{\partial \rho}{\partial p} \right)_h \Big|_{(i,j)} \frac{dp}{dt} \Big|_{(i,j)} \quad (5.23)$$

## 5.4 The momentum equations

The discretisation of the compressible flow momentum equations will be similar to the discretisation of the incompressible flow momentum equations in Wesseling et al. [84] with the difference that here  $(\rho U)^\alpha$ , instead of  $U^\alpha$ , is chosen to be a primitive variable. As can be seen in Figure 5.2, different control volumes are used for the two momentum equations, so they have to be treated separately. Here, we will only describe the discretisation of the first momentum equation in conservative formulation, (5.2) with  $\alpha = 1$ , given by

$$\frac{\partial(\rho U)^1}{\partial t} + (U^\beta(\rho U)^1)_{,\beta} = -(g^{1\beta} p)_{,\beta}. \quad (5.24)$$

The second momentum equation, (5.2) with  $\alpha = 2$ , is discretised along the same lines.

### 5.4.1 Finite volume discretisation

The control volume for the discretisation of the first momentum equation in point  $[x_{i-\frac{1}{2}}, y_j, t_{n+1}]$ , for  $i = 2, \dots, M$ ;  $j = 2, \dots, N - 1$ , is shown in Figure 5.4. The discretisation will be carried out using the same derivations as for the discretisation of the continuity equation.

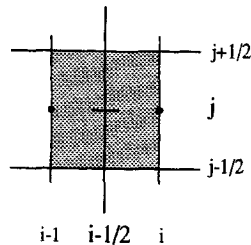


Figure 5.4: Control volume for the first momentum equation in the computational domain

#### Time derivative

The time derivative is integrated using the midpoint rule:

$$\int_{\Omega_{i-1/2,j}} \frac{\partial(\rho U)^1}{\partial t} d\Omega = \int_{G_{i-1/2,j}} \frac{\partial(\rho U)^1}{\partial t} \sqrt{g} d\xi^1 d\xi^2 \approx \sqrt{g} \Big|_{(i-1/2,j)} \frac{\partial(\rho U)^1}{\partial t} \Big|_{(i-1/2,j)} = \frac{d(\rho V)^1}{dt} \Big|_{(i-1/2,j)}. \quad (5.25)$$

**Pressure term**

For the pressure term we write

$$\int_{\Omega_{i-1/2,j}} (g^{1\beta} p)_{,\beta} d\Omega = \int_{G_{i-1/2,j}} g^{1\beta} p_{,\beta} \sqrt{g} d\xi^1 d\xi^2 \approx (g^{11} \sqrt{g})_{(i-1/2,j)} p \Big|_{((i-1,j))}^{((i,j))} + (g^{12} \sqrt{g})_{(i-1/2,j)} p \Big|_{((i-1/2,j-1/2))}^{((i-1/2,j+1/2))}. \quad (5.26)$$

Where necessary interpolation takes place to express  $p$  in terms of its values at cell centres.

**Convection term**

Furthermore, integration of the inertia term over  $\Omega_{i-1/2,j}$ , using (5.7) and (5.10) gives

$$\int_{\Omega_{i-1/2,j}} ((\rho U)^1 U^\beta)_{,\beta} d\Omega = \int_{G_{i-1/2,j}} \left( \frac{\partial \frac{1}{\sqrt{g}} (\rho V)^1 V^\beta}{\partial \xi^\beta} + \left\{ \frac{1}{\gamma\beta} \right\} \frac{1}{\sqrt{g}} (\rho V)^1 V^\gamma \right) d\xi^1 d\xi^2 \approx \left( \frac{1}{\sqrt{g}} V^1 (\rho V)^1 \right) \Big|_{((i-1,j))}^{((i,j))} + \left( \frac{1}{\sqrt{g}} V^2 (\rho V)^1 \right) \Big|_{((i-1/2,j-1/2))}^{((i-1/2,j+1/2))} + \left( \left\{ \frac{1}{\gamma\beta} \right\} \frac{1}{\sqrt{g}} (\rho V)^\gamma V^\beta \right)_{(i-1/2,j)} \quad (5.27)$$

Note that the Christoffel symbols in (5.27) are not continuous on cell faces. This can lead to inaccurate results on meshes with a rapid change in mesh-size. Our computations of inviscid flows did not suffer from this. When computing viscous flows, solving the discretised Navier-Stokes equations where more Christoffel symbols occur than in the Euler equations, we found inaccuracies for grids with large jumps in mesh size. The Christoffel symbols are avoided in the discretisation of the convection term, as discussed in Wesseling et al. [82], by using the fact that  $g_{\gamma}^{\alpha\beta} = 0$ . This method is only implemented for fully incompressible flows.

In equation (5.27) fluxes and momentum components are required in integration points where they are not defined, hence we have to approximate them. For this approximation there are several possibilities. We will discuss several options leading to central and first-order upwind discretisation, in the next section higher-order upwind methods will be discussed.

**5.4.2 Central approximation of convection term**

In this section the central approximation of the convection terms in the momentum equation (5.27) is discussed. We start with the central approximation of the first term

of equation (5.27). In this term  $V^1$  and  $(\rho V)^1$  can each be approximated by linear interpolation:

$$((\rho V)^1 V^1)_{(i,j)} = \frac{1}{4} [V^1_{(i-1/2,j)} + V^1_{(i+1/2,j)}] [(\rho V)^1_{(i-1/2,j)} + (\rho V)^1_{(i+1/2,j)}]. \quad (5.28)$$

This is a second order central discretisation. Of course, also the entire term can be linearly interpolated:

$$((\rho V)^1 V^1)_{(i,j)} = \frac{1}{2} \{ [V^1 (\rho V)^1]_{(i-1/2,j)} + [V^1 (\rho V)^1]_{(i+1/2,j)} \}, \quad (5.29)$$

which gives a second order central discretisation too. This term in (5.27) at location  $(i-1,j)$  is approximated in the same way. Both approximations (5.28) and (5.29) lead to a conservative discretisation since over the entire grid contributions at internal points cancel out. The results for the two approximations were for our applications very similar, see Chapters 8 and 9.

In the second term of equation (5.27),  $(V^2 (\rho V)^1)_{(i-1/2,j-1/2)}$ , linear interpolation of  $V^2$  and  $(\rho V)^1$  gives the following central discretisation:

$$(V^2 (\rho V)^1)_{(i-1/2,j-1/2)} = \frac{1}{4} [V^2_{(i,j-1/2)} + V^2_{(i-1,j-1/2)}] [(\rho V)^1_{(i-1/2,j)} + (\rho V)^1_{(i-1/2,j-1)}]. \quad (5.30)$$

The same term in (5.27) at position  $(i-1/2,j+1/2)$  is discretised in the same way. This also gives a conservative discretisation since the contributions at internal points cancel out. The second option for the first term (interpolation of the entire term) is for this term impossible, since the variables  $V^2$  and  $(\rho V)^1$  occupy different positions in the grid.

In the third term of equation (5.27) we have to approximate the following three terms:  $(\rho V)^1 V^1)_{(i-1/2,j)}$ ,  $(\rho V)^1 V^2)_{(i-1/2,j)}$ , and  $(\rho V)^2 V^2)_{(i-1/2,j)}$ . For the velocity and momentum components in the first of these terms no interpolation is needed. In the second term  $V^1$  is already in the right position,  $V^2$  can be approximated by the following interpolation:

$$V^2_{(i-1/2,j)} = \frac{1}{4} [V^2_{(i-1,j+1/2)} + V^2_{(i,j+1/2)} + V^2_{(i-1,j-1/2)} + V^2_{(i,j-1/2)}]. \quad (5.31)$$

The third term is a source term that is approximated by central interpolation. There are two obvious options:

$$\begin{aligned} ((\rho V)^2 V^2)_{(i-1/2,j)} &= \frac{1}{4} \{ [(\rho V)^2 V^2 (\rho V)^2 V^2]_{(i-1,j+1/2)} + \\ &\quad [(\rho V)^2 V^2 (\rho V)^2 V^2]_{(i,j+1/2)} + [(\rho V)^2 V^2 (\rho V)^2 V^2]_{(i-1,j-1/2)} + \\ &\quad [(\rho V)^2 V^2 (\rho V)^2 V^2]_{(i,j-1/2)} \}, \end{aligned} \quad (5.32)$$

and:

$$\begin{aligned} ((\rho V)^2 V^2)_{(i-1/2,j)} &= \frac{1}{16} [((\rho V)^2 V^2)_{(i-1,j+1/2)} + ((\rho V)^2 V^2)_{(i,j+1/2)} + \\ &\quad ((\rho V)^2 V^2)_{(i-1,j-1/2)} + ((\rho V)^2 V^2)_{(i,j-1/2)}]^2. \end{aligned} \quad (5.33)$$

In our computations we did not see a difference between these two options.

### 5.4.3 Upwind approximation of convection term

In this section the first order-upwind approximation of the convection terms in the momentum equation (5.27) are discussed. We start with the upwind approximation of the first term of the convection term of the first momentum equation (5.27), namely  $((\rho V)^1 V^1)_{(i,j)}$ . For  $V_{(i,j)}^1 = \frac{1}{2}[V_{(i-\frac{1}{2},j)}^1 + V_{(i+\frac{1}{2},j)}^1] > 0$  a first-order upwind discretisation is:

$$(\rho V)^1 V^1_{(i,j)} = (\rho V)_{(i-1/2,j)}^1 V_{(i,j)}^1, \quad (5.34)$$

while for  $V_{(i,j)}^1 < 0$  we take:

$$((\rho V)^1 V^1)_{(i,j)} = (\rho V)_{(i+1/2,j)}^1 V_{(i,j)}^1. \quad (5.35)$$

Note, that here only the momentum components  $(\rho V)^1$  are upwinded. Another possibility is to upwind the entire term. For  $V_{(i,j)}^1 > 0$  this gives:

$$((\rho V)^1 V^1)_{(i,j)} = [(\rho V)^1 V^1]_{(i-1/2,j)}, \quad (5.36)$$

while for  $V_{(i,j)}^1 < 0$  this gives:

$$((\rho V)^1 V^1)_{(i,j)} = [(\rho V)^1 V^1]_{(i+1/2,j)}. \quad (5.37)$$

The same term in (5.27) at location  $(i-1,j)$  is discretised in the same way. Both upwind discretisations are conservative. In our computations the second option, upwinding of the entire term (5.36)-(5.37), gave more accurate results than the first (5.34)-(5.35).

The second term of equation (5.27),  $((\rho V)^1 V^2)_{(i-1/2,j-1/2)}$  originates from an integral in the direction of  $V^2$ . Consequently, a first-order upwind discretisation of this term is for  $V_{(i-1/2,j-1/2)}^2 = \frac{1}{2}[V_{(i,j-1/2)}^2 + V_{(i-1,j-1/2)}^2] > 0$ :

$$((\rho V)^1 V^2)_{(i-1/2,j-1/2)} = (\rho V)_{(i-1/2,j-1)}^1 V_{(i-1/2,j-1/2)}^2, \quad (5.38)$$

while for  $V_{(i-1/2,j-1/2)}^2 < 0$  this gives:

$$((\rho V)^1 V^2)_{(i-1/2,j-1/2)} = (\rho V)_{(i-1/2,j)}^1 V_{(i-1/2,j-1/2)}^2. \quad (5.39)$$

This term in (5.27) at position  $(i-1/2,j+1/2)$  is discretised in the same way. This gives a conservative discretisation since the contributions at internal points cancel out. Upwind evaluation of the entire term is for this term impossible, since the variables  $V^2$  and  $(\rho V)^1$  occupy different positions in the grid.

For the third term of equation (5.27) the central interpolation of section 5.4.2 is used.

For  $\alpha = 2$ , finite volume integration of the momentum equation takes place over a control volume  $\Omega_{i,j-1/2}$  centered at a  $V^2$  grid point. Further details need not be given, because the method followed is the same as for  $\alpha = 1$ .



## 5.5 The energy equation

The energy equation in non-conservation formulation can be rewritten as

$$\frac{\partial h}{\partial t} + (U^\alpha h)_{,\alpha} = -(\gamma - 2) h U_{,\alpha}^\alpha, \quad (5.40)$$

which is also a non-conservation formulation. This non-conservation form is used because it allows a convenient formulation of our time-stepping method. For a discussion of other options we refer to Section 6.3. Our computations did not seem to suffer from this, the shock speeds were right in all cases. Only in the computation of contact discontinuities the non-conservation energy equation might be the cause of small inaccuracies.

### 5.5.1 Finite volume discretisation

The scalar control volume for the discretisation of the energy equation in point  $[x_i, y_j, t_{n+1}]$ , for  $i = 2, \dots, M-1$ ;  $j = 2, \dots, N-1$  is the same as the control volume for the continuity equation, see Figure 5.3. The time derivative in the energy equation is integrated using the midpoint rule:

$$\int_{\Omega_{i,j}} \frac{\partial h}{\partial t} d\Omega \approx \sqrt{g} \Big|_{(i,j)} \frac{dh}{dt} \Big|_{(i,j)}. \quad (5.41)$$

For the right hand side term we write:

$$\int_{\Omega_{i,j}} -(\gamma - 2) h U_{,\alpha}^\alpha d\Omega \approx -(\gamma - 2) h_{i,j} \left( V^1 \Big|_{(i-1/2,j)}^{(i+1/2,j)} + V^2 \Big|_{(i,j-1/2)}^{(i,j+1/2)} \right). \quad (5.42)$$

This is a non-conservative discretisation, since at the summation of the contributions of each control volume, the contribution of this term does not cancel in internal points. The convection term becomes:

$$\int_{\Omega_{i,j}} (U^\alpha h)_{,\alpha} d\Omega \approx (V^1 h) \Big|_{(i-1/2,j)}^{(i+1/2,j)} + (V^2 h) \Big|_{(i,j-1/2)}^{(i,j+1/2)}. \quad (5.43)$$

In this term, the variable  $h$  is needed in grid points where it is not given. Hence, we have to approximate it. For this approximation we can either use a central or an upwind approximation. A central approximation of the term  $(V^1 h)_{(i+1/2,j)}$  is:

$$(V^1 h)_{(i+1/2,j)} = V_{(i+1/2,j)}^1 \frac{1}{2} (h_{(i+1,j)} + h_{(i,j)}). \quad (5.44)$$

This is a conservative discretisation. A first order upwind approximation for  $V_{(i+1/2,j)}^1 > 0$  is:

$$(V^1 h)_{(i+1/2,j)} = V_{(i+1/2,j)}^1 h_{(i,j)}, \quad (5.45)$$

and for  $V_{(i+1/2,j)}^1 < 0$ :

$$(V^1 h)_{(i+1/2,j)} = V_{(i+1/2,j)}^1 h_{(i+1,j)}. \quad (5.46)$$

In this case only the enthalpy is upwinded. Of course, also the entire term can be approximated upwind, but then the velocity has to be interpolated. This gives for  $U_{(i+1/2,j)}^1 > 0$ :

$$(V^1 h)_{(i+1/2,j)} = \frac{1}{2}(V_{(i+1/2,j)}^1 + V_{(i-1/2,j)}^1)h_{(i,j)}, \quad (5.47)$$

and for  $U_{(i+1/2,j)}^1 < 0$ :

$$(V^1 h)_{(i+1/2,j)} = \frac{1}{2}(V_{(i+3/2,j)}^1 + V_{(i+1/2,j)}^1)h_{(i+1,j)}. \quad (5.48)$$

Both upwind versions are conservative. In the computations the first version gave better results.

## 5.6 The equation of state

The density in the cell centres follows from the equation of state (4.25)

$$\rho_{i,j} = \eta(M_\infty) \frac{p_{i,j}}{h_{i,j}} + \omega(M_\infty) \frac{1}{h_{i,j}}, \quad (5.49)$$

where  $\eta(M_\infty)$  and  $\omega(M_\infty)$  are the following functions

$$\eta(M_\infty) = \frac{\gamma M_\infty^2}{1 + \frac{\gamma-1}{2} M_\infty^2}, \quad \omega(M_\infty) = p_v \left( \left( 1 + \frac{\gamma-1}{2} M_\infty^2 \right)^{\frac{-\gamma}{\gamma-1}} - 1 \right) + 1. \quad (5.50)$$

Given  $\rho_{i,j}$ , the transformed velocity components  $V_{i-1/2,j}^\alpha$  follow from the transformed momentum components as follows:

$$V_{i-1/2,j}^1 = \frac{(\rho V^1)_{i-1/2,j}}{\frac{1}{2}(\rho_{i-1,j} + \rho_{i,j})} \quad (5.51)$$

$$V_{i,j-1/2}^2 = \frac{(\rho V^2)_{i,j-1/2}}{\frac{1}{2}(\rho_{i,j-1} + \rho_{i,j})}. \quad (5.52)$$

At the end of the entire computation the contravariant velocity components  $U^1$ ,  $U^2$  are recovered from  $V^1$ ,  $V^2$ . In the next chapter the equations will be discretised in time.

## 5.7 Upwind methods

In the previous sections both the second order accurate central discretisation and the first order upwind discretisation are described. The central discretisation is used in many subsonic and transonic calculations in channels and nozzles, see Chapter 8. For calculations of supersonic flow and nonstationary shock tube problems the simple first-order upwind method is used. In order to obtain second order accurate results and crisp resolution of contact discontinuities the same measures were taken as for standard compressible flow methods: higher order upwind biased TVD schemes with flux limiting were implemented using the defect-correction formulation as described by Zijlema [90]. Also upwind-biased density evaluation was implemented, which is beneficial for satisfying the entropy condition.

### Higher order upwind methods

Various higher order upwind biased TVD schemes with flux limiting were implemented using the defect-correction formulation as described in Zijlema [90]. These schemes are implemented as a limited correction to the first order upwind scheme. It suffices to briefly discuss the one-dimensional case. If  $u > 0$  in the momentum equation,  $m_{i+\frac{1}{2}}$  is approximated by:

$$m_{i+\frac{1}{2}} = m_i + \frac{1}{2}\Psi(r_{i+\frac{1}{2}}^+)(m_i - m_{i-1}), \quad (5.53)$$

where

$$r_{i+\frac{1}{2}}^+ = \frac{m_{i+1} - m_i}{m_i - m_{i-1}}, \quad (5.54)$$

whereas if  $u < 0$   $m_{i+\frac{1}{2}}$  is approximated by:

$$m_{i+\frac{1}{2}} = m_i - \frac{1}{2}\Psi(r_{i+\frac{1}{2}}^-)(m_{i+2} - m_{i+1}) \quad (5.55)$$

where

$$r_{i+\frac{1}{2}}^- = \frac{m_{i+1} - m_i}{m_{i+1} - m_{i+1}}. \quad (5.56)$$

Here  $\Psi(r)$  is a nonlinear function. For example, for the second order MUSCL scheme of van Leer [75] we have

$$\Psi(r) = \max[0, \min(2, \frac{1}{2}r + \frac{1}{2}, 2r)]. \quad (5.57)$$

For further details about flux limiting we refer to [91] and references quoted therein.

### Upwind-biased density evaluation

In supersonic flow regions the density is biased in the upwind direction in the continuity

equation, see also Hughes and Mallet [29], and Habashi and Hafez [20]. This introduces a measure of irreversibility which is beneficial for satisfying the entropy condition. For upwind-biased density evaluation a Mach-dependent shift operator is used. Assuming  $U^1$  to be the dominant velocity component, this is done as follows. In cells with a Mach number lower than  $1 - d$ , with  $d$  a parameter to be chosen (in the following,  $d = 0.1$ ), no upstream bias is employed, and central interpolation is used to evaluate the density in the velocity points. For cells with a Mach number above  $1 - d$  the density in the continuity equation is shifted upstream in the following way:

$$\left(\frac{\partial \rho}{\partial p}\right)_h \frac{\partial p}{\partial t} + \left(\frac{\partial \rho}{\partial h}\right)_p \frac{\partial h}{\partial t} + \left(\frac{\tilde{\rho}}{\rho}(\rho V)^1\right)\Big|_{i-\frac{1}{2},j}^{i+\frac{1}{2},j} + (\rho V)^2 \Big|_{i,j-\frac{1}{2}}^{i,j+\frac{1}{2}} = 0, \quad (5.58)$$

with  $\rho_{i+\frac{1}{2},j} = \frac{1}{2}(\rho_{i,j} + \rho_{i+1,j})$  the centrally evaluated density and  $\tilde{\rho}_{i+\frac{1}{2},j}$  the shifted evaluation of the density, given by:

$$\tilde{\rho}_{i+\frac{1}{2},j} = (0.5 - S_{i+\frac{1}{2},j})\rho_{i+1,j} + (0.5 + S_{i+\frac{1}{2},j})\rho_{i,j}. \quad (5.59)$$

Here  $S$  is a continuous switch function defined by:

$$S_{i+\frac{1}{2},j} = S(V_{i+\frac{1}{2},j}^1, M_{i+\frac{1}{2},j}) = \frac{V_{i+\frac{1}{2},j}^1}{|V_{i+\frac{1}{2},j}^1|} \min\left[\frac{1}{2}, \max\left[0, \frac{1}{4}\left(\frac{M_{i+\frac{1}{2},j} - 1}{d} + 1\right)\right]\right]. \quad (5.60)$$

The local Mach number in the cell center is computed as:

$$M_{i,j}^2 = \frac{M_\infty^2}{1 + \frac{\gamma-1}{2}M_\infty^2} \frac{(V_{i+\frac{1}{2},j}^1 + V_{i-\frac{1}{2},j}^1)^2 + (V_{i,j+\frac{1}{2}}^2 + V_{i,j-\frac{1}{2}}^2)^2}{4g\rho_{i,j}^2 h_{i,j}}. \quad (5.61)$$

$M_{i+\frac{1}{2},j}$  is found through linear interpolation. The switch function  $S$  varies between 0 (no bias) for  $M < 1 - d$  to  $\frac{1}{2}$  (full bias) for  $M > 1 + d$ . For ease of exposition it has been assumed that the flow is mainly in the  $\xi^1$ -direction. In the general case upwind-biased density evaluation is also employed in the  $\xi^2$ -direction.

# 6

## Solution strategy

After discretisation in space, explained in the previous chapter, the equations are discretised in time and solved. The system of equations is solved in an uncoupled manner by a pressure correction method. In this chapter first the time discretisation by the  $\theta$ -method is described. Thereafter, the pressure correction method for incompressible flows that arises after manipulation of the continuity and the momentum equation, described by Zijlema et al. [92, 93], is extended to incorporate compressibility. For gain of insight an overview of the solution algorithm is given, whereafter the solution algorithm is written out for the case of one-dimensional flow. The resulting method does not preserve contact discontinuities very well. This is the reason why we developed two alternative pressure correction equations for compressible flows. Of course, also in this case for  $M \downarrow 0$  the original incompressible pressure correction equation should be recovered. Finally, the uncoupled systems of equations are solved by the preconditioned GMRES method, as explained in the last section of this chapter.

### 6.1 Time integration by the $\theta$ -method

Our main goal here is to show Mach-uniform efficiency and accuracy. For computation of both stationary flows and time-accurate solutions of nonstationary flow problems time-stepping was used. This method is for stationary flow problems less efficient than direct application of a well-designed iterative method to the stationary flow discretised equations. But for our present purposes it suffices to show that efficiency and accuracy of the solver used do not degrade as  $M \downarrow 0$  or when the flow becomes supersonic, see Chapter 8.

For brevity, we leave the spatial derivatives undiscretised and write  $m^\alpha$  for  $\rho U^\alpha$ . In practice we discretise in space (as explained in Section 5.2) and incorporate the boundary conditions before discretising in time. The continuity and momentum equations are

discretised in time as follows:

$$\left(\frac{\partial \rho}{\partial p}\right)_h^n \frac{p^{n+1} - p^n}{\delta t} + \left(\frac{\partial \rho}{\partial h}\right)_p^n \frac{h^{n+1} - h^n}{\delta t} + \mu(m_{,\alpha}^\alpha)^{n+1} + (1 - \mu)(m_{,\alpha}^\alpha)^n = 0, \quad (6.1)$$

$$\begin{aligned} \frac{(m^\alpha)^{n+1} - (m^\alpha)^n}{\delta t} + \theta ((m^\alpha)^{n+1} (U^\beta)^{n+1})_{,\beta} + (1 - \theta)(m^\alpha U^\beta)_{,\beta}^n = \\ - (g^{\alpha\beta} (\theta p^{n+1} + (1 - \theta)p^n))_{,\alpha}. \end{aligned} \quad (6.2)$$

Depending on the parameters  $\mu$  and  $\theta$ , the discretisation is explicit or implicit. But in the incompressible flow case it is necessary to take  $\mu = 1$ , because then the pressure acts as a Lagrangian multiplier enabling satisfaction of the divergence freedom constraint. The convection term in the momentum equation (6.2) is linearised as follows:

$$((m^\alpha)^{n+1} (U^\beta)^{n+1})_{,\beta} \approx ((m^\alpha)^{n+1} (U^\beta)^n)_{,\beta}. \quad (6.3)$$

The energy equation is discretised implicitly, with the velocity always taken at the previous time level:

$$\begin{aligned} \frac{h^{n+1} - h^n}{\delta t} + \theta(h^{n+1}(u^\alpha)^\alpha)_{,\alpha} + (1 - \theta)(h^n(u^\alpha)^\alpha)_{,\alpha} = \\ -\theta(\gamma - 2)h^{n+1}(u^\alpha)^\alpha_{,\alpha} - (1 - \theta)(\gamma - 2)h^n(u^\alpha)^\alpha_{,\alpha}. \end{aligned} \quad (6.4)$$

In this way at each time step the energy equation can be solved first with the velocity at the new time level still unknown. The equation of state is given by (4.25). For an overview of the order in which the resulting systems of equations are solved, see Section 6.3 of this chapter.

## 6.2 Original pressure correction method

The standard workhorse to do time-stepping in the incompressible flow case is the pressure correction method, already introduced by Harlow and Welch [23]. This method will also be employed here, for all Mach numbers, in order to achieve Mach-uniform accuracy and efficiency. In this section the pressure correction method for incompressible flow as derived by manipulation of the continuity and the momentum equation by Zijlema et al. [92, 93] will be extended to compressible flow. In the incompressible flow case there is no time-derivative for the pressure. This is also the case in the present Mach-uniform formulation, as it should be; for  $M = 0$  the factor  $\frac{\partial \rho}{\partial p}$  in equation (5.58) is zero, according to the dimensionless equation of state.

### 6.2.1 Derivation of compressible pressure correction equation

With the pressure correction method, first, a prediction for the momentum field  $(m^\alpha)^*$  is computed from the momentum equation with the pressure at the old time level

$$\frac{(m^\alpha)^* - (m^\alpha)^n}{\delta t} + \theta ((m^\alpha)^* (U^\beta)^n)_{,\beta} + (1 - \theta)(m^\alpha U^\beta)_{,\beta}^n = - (g^{\alpha\beta} p^n)_{,\beta}. \quad (6.5)$$

Next, a pressure correction  $\delta p = p^{n+1} - p^n$  is computed. To find the correction equation, first (6.5) is subtracted from (6.2), neglecting the difference in the convection terms:

$$\frac{(m^\alpha)^{n+1} - (m^\alpha)^*}{\delta t} = -\mu (g^{\alpha\beta} (p^{n+1} - p^n))_{,\beta}. \quad (6.6)$$

Van Kan [74] has shown for the incompressible flow case that neglecting the difference in the convection term does not affect the temporal order of accuracy, and  $\theta = 1/2$ ,  $\mu = 1$  gives second order accuracy in time. Here, in the compressible flow case, at least first order accuracy is maintained. Next, the discrete divergence of the discretised version of (6.6) is taken, and in the resulting expression  $(m^\alpha)_{,\alpha}^{n+1}$  is substituted from (6.1), which after multiplication by  $\mu\delta t$  results in

$$\left(\frac{\partial\rho}{\partial p}\right)_h^n \frac{\delta p}{\delta t} - \mu^2 \delta t (g^{\alpha\beta} \delta p)_{,\alpha\beta} = -\mu(m^\alpha)_{,\alpha}^* + (1 - \mu)(m^\alpha)_{,\alpha}^n - \left(\frac{\partial\rho}{\partial h}\right)_p^n \frac{\delta h}{\delta t}. \quad (6.7)$$

This is called the pressure correction equation. For the computation of  $\partial\rho/\partial p$  and  $\partial\rho/\partial h$  the dimensionless equation of state (4.25) is used. Note that we have to know  $\delta h = h^{n+1} - h^n$  before the pressure correction equation can be solved. Due to the implicit discretisation of the energy equation (6.4), the enthalpy at the new time level only depends on  $h^n$  and  $u^n$ . Hence, the energy equation can be solved before the pressure correction equation. To obtain at the end of a time step the velocity components  $(u^\alpha)^{n+1}$  from  $(m^\alpha)^{n+1}$ , the mass fluxes are divided by  $\rho^{n+1}$ , which is computed from the equation of state. In practice the Euler equations are first discretised in space before the pressure correction method is applied, so that the equations referred to this section are linear algebraic systems. No boundary conditions for the pressure correction equation are required, since the physical velocity and pressure boundary conditions have already been incorporated in the continuity and momentum equations, from which the pressure correction equation is derived. The spatial discretisation in general coordinates is described in the previous chapter. In the next section the solution algorithm for one-dimensional flow is described. There the spatially discretised (in 1-D) form of the pressure correction equation is given.

#### Limit $M \downarrow 0$ in pressure correction equation

Having derived a compressible flow pressure correction, we now investigate the incompressible flow limit of this equation. The question is whether the incompressible flow limit of the compressible flow pressure correction is equal to the incompressible flow pressure correction equation. That this is indeed the case can be easily seen by

taking  $M_\infty = 0$ . Then from the dimensionless equation of state (4.25) it follows that  $\partial\rho/\partial p = 0$ . Consequently, the time derivative of the pressure disappears from the continuity equation (6.1), hence from the pressure correction equation (6.7). When, in addition, the enthalpy in the flow is constant, also the time derivative of the enthalpy disappears from the continuity equation, so that the continuity equation becomes  $m_\alpha^\alpha = 0$ . Furthermore, in the incompressible flow limit  $\mu = 1$  should be chosen in Eq. (6.1), so that the pressure acts as a Lagrangian multiplier. As a result, for a constant enthalpy flow with  $M_\infty = 0$  and  $\mu = 1$  the incompressible flow pressure correction equation:

$$-\delta t (g^{\alpha\beta} \delta p)_{,\alpha\beta} = -(m^\alpha)_{,\alpha}^* \quad (6.8)$$

as described by Zijlema et al. [92, 93], is recovered.

### 6.2.2 Overview of solution algorithm

In this section the algorithm process will be derived step by step. In the previous section the equations are derived omitting discretisation in space. In reality, the equations are first discretised in space, as explained in Section 5.2, then the boundary conditions are incorporated, thereafter the equations are discretised in time using the pressure correction formulation, as explained in the previous section. Gathering the grid function values  $h_{i,j}$ ,  $(\rho V)_{i+\frac{1}{2},j}^1$ ,  $(\rho V)_{i,j+\frac{1}{2}}^2$ ,  $p_{i,j}$  in algebraic vectors  $\mathbf{h}$ ,  $(\rho V)^1$ ,  $(\rho V)^2$ ,  $\mathbf{p}$ , and the derivatives  $\rho_{,p_{i,j}}$  and  $\rho_{,h_{i,j}}$  in diagonal of the matrices  $R_p$  and  $R_h$  respectively, the pressure correction method for the compressible Euler equations consists of the following steps:

- a) Find  $\mathbf{h}^{n+1}$  from

$$\frac{1}{\Delta t} (\mathbf{h}^{n+1} - \mathbf{h}^n) + N_h(\mathbf{h}^{n+1}) = 0$$

- b) Determine  $(\rho V)^{1*}$  and  $(\rho V)^{2*}$  from

$$\frac{1}{\Delta t} ((\rho V)^{1*} - (\rho V)^{1n}) + N_v^1(\rho V)^{1*} = -G_1 \mathbf{p}^n$$

$$\frac{1}{\Delta t} ((\rho V)^{2*} - (\rho V)^{2n}) + N_v^2(\rho V)^{2*} = -G_2 \mathbf{p}^n$$

- c) Find  $\delta \mathbf{p} = \mathbf{p}^{n+1} - \mathbf{p}^n$  from

$$((\Delta t)^2 D_1 G_1 + (\Delta t)^2 D_2 G_2 + R_p^n) \delta \mathbf{p} = -R_h^n \delta \mathbf{h} - \Delta t (D_1(\rho V)^{1*} + D_2(\rho V)^{2*}),$$

where  $\delta \mathbf{h} = \mathbf{h}^{n+1} - \mathbf{h}^n$ .

- d) Find  $(\rho V)^{1n+1}$  and  $(\rho V)^{2n+1}$  from

$$(\rho V)^{1n+1} = (\rho V)^{1*} - \Delta t G_1 \delta \mathbf{p},$$

$$(\rho V)^{2n+1} = (\rho V)^{2*} - \Delta t G_2 \delta \mathbf{p}.$$

- e) Compute  $\rho^{n+1}$  from the equation of state (5.49).

- f) Determine  $\mathbf{V}^{1n+1}$  and  $\mathbf{V}^{2n+1}$  by division of  $(\rho V)^{1n+1}$  and  $(\rho V)^{2n+1}$  by the density.



The operators  $N_h$ ,  $N_v^1$ ,  $N_v^2$  depend nonlinearly on the unknowns at  $t = t^n$ , as can be seen in the previous section. Each time step in step a), b) and c) a system of equations has to be solved, see Section 6.4 for further details.

### 6.2.3 Solution algorithm in one dimension

It is instructive to write down the fully discretised scheme for the one-dimensional flow case. We will first do this without upwind-biased density evaluation. First, the fully discretised continuity and momentum equations will be listed, from which the pressure correction equation is derived. This derivation is the same as in Section 6.2.1 of this chapter. We assume a uniform grid, and write  $\lambda = \delta t / \delta x$ ,  $m = m^1$ ,  $u = u^1$ ,  $\delta p = p^{n+1} - p^n$  etc. The one-dimensional discretised continuity equation is given by (5.20):

$$\delta \rho_j + \mu \lambda m^{n+1} \Big|_{j-\frac{1}{2}}^{j+\frac{1}{2}} + (1 - \mu) \lambda m^n \Big|_{j-\frac{1}{2}}^{j+\frac{1}{2}} = 0, \quad (6.9)$$

In this equation  $\delta \rho_j$  is replaced by  $\left(\frac{\partial \rho}{\partial p}\right)_j^n \delta p_j + \left(\frac{\partial \rho}{\partial h}\right)_j^n \delta h_j$ . The one-dimensional discretised momentum equation is given by:

$$m_{j+\frac{1}{2}}^{n+1} - m_{j+\frac{1}{2}}^n + \theta \lambda (m^{n+1} u^n) \Big|_{j-\frac{1}{2}}^{j+\frac{1}{2}} + (1 - \theta) \lambda (m u^n) \Big|_{j-\frac{1}{2}}^{j+\frac{1}{2}} = -\lambda (\mu p^{n+1} + (1 - \mu) p^n) \Big|_j^{j+1}, \quad (6.10)$$

where a first order upwind scheme is used, assuming  $u^n \geq 0$ .

The discretisation of the one-dimensional energy equation is given by

$$h_j^{n+1} - h_j^n + \frac{1}{2} \theta \lambda (u_{j-\frac{1}{2}}^n + u_{j+\frac{1}{2}}^n) h^{n+1} \Big|_{j-1}^j + \frac{1}{2} (1 - \theta) \lambda (u_{j-\frac{1}{2}}^n + u_{j+\frac{1}{2}}^n) h^n \Big|_{j-1}^j + \theta \lambda (\gamma - 1) h_j^{n+1} u^n \Big|_{j-\frac{1}{2}}^{j+\frac{1}{2}} + (1 - \theta) \lambda (\gamma - 1) h_j^n u^n \Big|_{j-\frac{1}{2}}^{j+\frac{1}{2}} = 0. \quad (6.11)$$

where a first order upwind scheme is used, assuming  $u^n \geq 0$ .

From these equations the predictor- and corrector momentum equations and the pressure correction equations are derived as described in the Section 6.2.1. In the solution algorithm, first  $\delta h$  is computed from (6.11). Next, the momentum is predicted according to

$$m_{j+\frac{1}{2}}^* - m_{j+\frac{1}{2}}^n + \theta \lambda (u^n m^*) \Big|_{j-\frac{1}{2}}^{j+\frac{1}{2}} + (1 - \theta) \lambda (u^n m^n) \Big|_{j-\frac{1}{2}}^{j+\frac{1}{2}} + \lambda p^n \Big|_j^{j+1} = 0. \quad (6.12)$$

Thereafter, the pressure correction is computed from:

$$-a_{j-1} \delta p_{j-1} + b_j \delta p_j - c_{j+1} \delta p_{j+1} = f_j, \quad (6.13)$$

where

$$a_{j-1} = \mu^2 \lambda \delta t, \quad (6.14)$$

$$b_j = \left( \frac{\partial \rho}{\partial p} \right)_j^n + 2\mu^2 \lambda \delta t, \quad (6.15)$$

$$c_{j+1} = \mu^2 \lambda \delta t, \quad (6.16)$$

$$f_j = -\mu \lambda m^* \Big|_{j-\frac{1}{2}}^{j+\frac{1}{2}} - (1-\mu) \lambda m^n \Big|_{j-\frac{1}{2}}^{j+\frac{1}{2}} - \delta h_j \left( \frac{\partial \rho}{\partial h} \right)_j^n. \quad (6.17)$$

For the derivation of this equation see Section 6.2.1. Once the pressure correction is computed, the momentum correction can be found from

$$m_{j+\frac{1}{2}}^{n+1} - m_{j+\frac{1}{2}}^* = -\mu \lambda \delta p \Big|_j^{j+1}. \quad (6.18)$$

From the pressure and enthalpy, now also the density is computed at  $t = t^{n+1}$  with the equation of state (5.49). As can be seen from (6.15) the compressibility term  $(\partial \rho / \partial p)_j^n$  has a positive contribution to the main diagonal, so that the compressible pressure correction equation is not harder to solve than the incompressible version.

### One-dimensional pressure correction equation with upwind-biased density evaluation

The same analysis is performed with upwind-biased density evaluation. Writing  $\sigma = \tilde{\rho} / \rho$ , see (5.59), the continuity equation becomes

$$\delta \rho_j + \mu \lambda (\sigma m)^{n+1} \Big|_{j-\frac{1}{2}}^{j+\frac{1}{2}} + (1-\mu) \lambda (\sigma m)^n \Big|_{j-\frac{1}{2}}^{j+\frac{1}{2}} = 0, \quad (6.19)$$

This equation is Newton-linearised as follows:

$$(\sigma m)^{n+1} \approx \sigma^n m^{n+1} + u^n \delta \tilde{\rho} - (u \sigma)^n \delta \rho. \quad (6.20)$$

This results in the following discrete continuity equation:

$$\delta \rho_j + \mu \lambda (\sigma^n m^{n+1} + u^n \delta \tilde{\rho} - u^n \sigma^n \delta \rho) \Big|_{j-\frac{1}{2}}^{j+\frac{1}{2}} + (1-\mu) \lambda (\sigma m)^n \Big|_{j-\frac{1}{2}}^{j+\frac{1}{2}} = 0. \quad (6.21)$$

It is assumed that  $u > 0$  and that the flow is supersonic, so that the first order upwind scheme is used and the density bias is in full force. This means that the switch function  $S$  in (5.60) is equal to  $\frac{1}{2}$ , so that  $\delta \tilde{\rho}_{j+\frac{1}{2}} = \delta \rho_j$ . As a result the continuity equation (6.21) becomes:

$$\begin{aligned} \delta \rho_j + \mu \lambda \left( \sigma_{j+\frac{1}{2}}^n m_{j+\frac{1}{2}}^{n+1} + u_{j+\frac{1}{2}}^n \delta \rho_j - u_{j+\frac{1}{2}}^n \sigma_{j+\frac{1}{2}}^n \frac{1}{2} (\delta \rho_{j+1} + \delta \rho_j) \right) - \\ \mu \lambda \left( \sigma_{j-\frac{1}{2}}^n m_{j-\frac{1}{2}}^{n+1} + u_{j-\frac{1}{2}}^n \delta \rho_{j-1} - u_{j-\frac{1}{2}}^n \sigma_{j-\frac{1}{2}}^n \frac{1}{2} (\delta \rho_j + \delta \rho_{j-1}) \right) \\ + (1-\mu) \lambda \left( \sigma_{j+\frac{1}{2}}^n m_{j+\frac{1}{2}}^n - \sigma_{j-\frac{1}{2}}^n m_{j-\frac{1}{2}}^n \right) = 0. \end{aligned} \quad (6.22)$$

In this equation  $\delta\rho_j$  is replaced by  $\left(\frac{\partial\rho}{\partial p}\right)_j^n \delta p_j + \left(\frac{\partial\rho}{\partial h}\right)_j^n \delta h_j$ . From this the pressure correction equation with density-biased upwinding is found to be

$$-a_{j-1}\delta p_{j-1} + b_j\delta p_j - c_{j+1}\delta p_{j+1} = f_j, \quad (6.23)$$

where

$$a_{j-1} = \mu\lambda\sigma_{j-\frac{1}{2}}^n + \left(\frac{\partial\rho}{\partial p}\right)_{j-1}^n \left(u_{j-\frac{1}{2}}^n + \frac{1}{2}(\sigma u)_{j-\frac{1}{2}}^n\right), \quad (6.24)$$

$$b_j = \mu\lambda(\sigma_{j+\frac{1}{2}}^n + \sigma_{j-\frac{1}{2}}^n) + \left(\frac{\partial\rho}{\partial p}\right)_j^n \left\{\frac{1}{\mu\lambda} + u_{j+\frac{1}{2}}^n - \frac{1}{2}\left((\sigma u)_{j+\frac{1}{2}}^n - (\sigma u)_{j-\frac{1}{2}}^n\right)\right\}, \quad (6.25)$$

$$c_{j+1} = \mu\lambda\sigma_{j+\frac{1}{2}}^n - \frac{1}{2}\left(\frac{\partial\rho}{\partial p}\right)_{j+1}^n (\sigma u)_{j+\frac{1}{2}}^n, \quad (6.26)$$

$$f_j = -(\sigma^n m^* + \left(\frac{1}{\mu} - 1\right)\sigma^n m^n)_{j-\frac{1}{2}}^{j+\frac{1}{2}} - \delta h_{j-1} \left(\frac{\partial\rho}{\partial h}\right)_{j-1}^n \left(u_{j-\frac{1}{2}}^n - \frac{1}{2}(\sigma u)_{j-\frac{1}{2}}^n\right) - \delta h_j \left(\frac{\partial\rho}{\partial h}\right)_j^n \left\{\frac{1}{\mu\lambda} + u_{j+\frac{1}{2}}^n - \frac{1}{2}(\sigma u)_{j-\frac{1}{2}}^{j+\frac{1}{2}}\right\} + \delta h_{j+1} \left(\frac{\partial\rho}{\partial h}\right)_{j+1}^n \frac{1}{2}(\sigma u)_{j+1}^n. \quad (6.27)$$

We see that now a directional bias has entered into the pressure correction equation. We have  $a_{j-1} > c_{j+1}$  if the solution is smooth, so that upstream conditions have a larger influence on  $\delta p$  than downstream conditions. This is in qualitative accordance with the fact that information travels in one direction only in supersonic flow. Furthermore, this directionality implies irreversibility in space. It is well-known that numerical schemes for hyperbolic conservation laws need to possess some irreversibility, in order to satisfy the entropy condition. The solution process remains the same as before.

### Boundary conditions

The pressure correction equation at the boundary is derived in the same way. First, the momentum equation is discretised across the boundary using virtual points. Thereafter, the virtual points are eliminated by linear interpolation:  $p_{J+1} = 2p_{J+\frac{1}{2}} - p_J$ , where the boundary is located at index  $J + \frac{1}{2}$ , so that  $J + 1$  is the index of the virtual point. Also, the physical velocity and pressure boundary conditions are incorporated in the continuity and momentum equations. Finally, the pressure correction equation at the boundary is derived in the same way as for the interior by substituting the momentum correction divergence into the discrete continuity equation.

### 6.3 Alternatives for better preservation of contact discontinuities

While testing the previously described pressure correction method on various shock tube problems, see Chapter 9, we found that the above pressure correction method does not entirely preserve contact discontinuities. In computation of nonstationary contact discontinuities, where the velocity is continuous and not equal to zero, and the pressure is continuous, while the density and temperature jump, wiggles arose in the pressure and velocity. This is probably due to the linearisation used in the continuity equation so that the equation  $\rho h = \eta p + \omega = \text{constant}$ , is not exactly satisfied. In this section an alternative for the original pressure correction method is proposed that does not suffer from this. This alternative pressure correction equation is derived using the preserved quantity,  $\rho h$ , and the energy equation. This method is expected to better preserve contact discontinuities. Of course, we should take care that the pressure correction equation converges to the incompressible pressure correction equation in the incompressible flow limit. The wiggles in the pressure and velocity in the solution of the contact discontinuity might also be due to our use of the non-conservation form of the energy equation. How to use a conservative formulation of the energy equation in the solution algorithm is also discussed in this section.

#### 6.3.1 Alternative pressure correction equation

It is possible to derive the equation for the pressure from the continuity and the energy equation; this works as follows. To begin with, the time derivative of the density is not rewritten into a time derivative of the pressure and the enthalpy, as before. But the continuity equation is multiplied by the enthalpy  $h$ , while the energy equation is multiplied by the density  $\rho$ :

$$h \frac{\partial \rho}{\partial t} + h \frac{\partial m}{\partial x} = 0, \quad (6.28)$$

$$\rho \frac{\partial h}{\partial t} + m \frac{\partial h}{\partial x} + (\gamma - 1) \rho h \frac{\partial u}{\partial x} = 0. \quad (6.29)$$

Addition of both equations gives:

$$\frac{\partial \rho h}{\partial t} + \gamma \frac{\partial m h}{\partial x} - (\gamma - 1) u \frac{\partial \rho h}{\partial x} = 0. \quad (6.30)$$

With the dimensionless equation of state  $\rho h = \eta(M_\infty)p + \omega(M_\infty)$  (with  $\eta \downarrow 0$  and  $\omega \rightarrow 1$  for  $M_\infty \downarrow 0$ ) this gives the following equation for the pressure:

$$\eta \frac{\partial p}{\partial t} + \gamma \frac{\partial m h}{\partial x} - (\gamma - 1) \eta u \frac{\partial p}{\partial x} = 0. \quad (6.31)$$

Note that the divergence freedom of the velocity in the incompressible flow limit follows from this equation: as  $M \downarrow 0$  we have

$$\gamma \frac{\partial m h}{\partial x} = \gamma \frac{\partial u(\eta p + \omega)}{\partial x} = 0 \quad \rightarrow \quad \gamma \frac{\partial u}{\partial x} = 0. \quad (6.32)$$

Now we will discretise the pressure equation (6.31) such that in the incompressible flow limit the original incompressible pressure correction equation is recovered. Discretisation in time is done as follows:

$$\eta \frac{\delta p}{\delta t} + \gamma \frac{\partial m^{n+1} h^{n+1}}{\partial x} - (\gamma - 1) \eta u^n \frac{\partial p^{n+1}}{\partial x} = 0, \quad (6.33)$$

which is equal to

$$\eta \frac{\delta p}{\delta t} + \gamma \frac{\partial \delta m h^{n+1}}{\partial x} + \gamma \frac{\partial m^* h^{n+1}}{\partial x} - (\gamma - 1) \eta u^n \frac{\partial \delta p}{\partial x} - (\gamma - 1) \eta u^n \frac{\partial p^n}{\partial x} = 0. \quad (6.34)$$

First order upwinding was used for the discretisation of the pressure gradient, which gives for  $u^n \geq 0$ :

$$\begin{aligned} \eta \delta p_j + \lambda \{ \gamma (\delta m h^{n+1})_{j+\frac{1}{2}} - \gamma (\delta m h^{n+1})_{j-\frac{1}{2}} - (\gamma - 1) \eta u_j^n (\delta p_{j+1} - \delta p_j) \} = \\ - \lambda \{ \gamma (m^* h^{n+1})_{j+\frac{1}{2}} - \gamma (m^* h^{n+1})_{j-\frac{1}{2}} - (\gamma - 1) \eta u_j^n (p_{j+1}^n - p_j^n) \}. \end{aligned} \quad (6.35)$$

Now the relation between the pressure correction and the momentum correction:

$$\delta m_{j+\frac{1}{2}} = m_{j+\frac{1}{2}}^{n+1} - m_{j+\frac{1}{2}}^* = -\mu \lambda \delta p_j^{j+1}, \quad (6.36)$$

which is obtained from the momentum equation, is substituted into (6.34), which gives:

$$\begin{aligned} \eta \delta p_j + \lambda \{ \mu \lambda \gamma (h_{j+\frac{1}{2}}^{n+1} (\delta p_j - \delta p_{j+1}) + \mu \lambda \gamma h_{j-\frac{1}{2}}^{n+1} (\delta p_j - \delta p_{j-1}) \\ - (\gamma - 1) \eta u_j^n (\delta p_{j+1} - \delta p_j) \} = \\ - \lambda \{ \gamma (m^* h^{n+1})_{j+\frac{1}{2}} - \gamma (m^* h^{n+1})_{j-\frac{1}{2}} - (\gamma - 1) \eta u_j^n (p_{j+1}^n - p_j^n) \}. \end{aligned} \quad (6.37)$$

In the low Mach number limit  $M \downarrow 0$  we have  $\eta \downarrow 0$ , so that the incompressible pressure correction equation is recovered. In Chapter 9 results for this alternative will be compared with results obtained with the original pressure correction formulation. There the alternative turns out to improve the preservation of contact discontinuities.

### 6.3.2 Conservative energy equation

In the previously derived alternative formulation, just as in the original pressure correction formulation, a non-conservation form of the energy equation is required to find  $h^{n+1}$ . By using a time-lag in the equation of state, in this alternative formulation also the conservation formulation of the energy equation can be used. This works as follows. The presence of  $h^{n+1}$  in the pressure correction equation (6.39), which forces us

to first solve the energy equation, is due to the fully implicit evaluation of the equation of state (5.49). When this equation is evaluated implicitly in the pressure, but explicitly in the enthalpy, as follows:

$$\rho^{n+1} = \eta(M_\infty) \frac{p^{n+1}}{h^n} + \omega(M_\infty) \frac{1}{h^n}, \quad (6.38)$$

the term  $h^{n+1}$  disappears from the pressure correction equation:

$$\frac{\eta}{\delta t} \frac{p^{n+1}}{h^n} - \frac{p^n}{h^n} + -\mu^2 \delta t (g^{\alpha\beta} \delta p)_{,\alpha\beta} = -\mu(m^\alpha)_{,\alpha}^* + (1 - \mu)(m^\alpha)_{,\alpha}^n. \quad (6.39)$$

This means that the energy equation can be solved after the pressure correction equation, when the velocity at the new time level  $u^{n+1}$  is known. Consequently, the conservation form of the energy equation can be used:

$$\frac{\partial \rho E}{\partial t} + \frac{\partial(\rho u E + up)}{\partial x} = 0, \quad (6.40)$$

with  $E = e + \frac{1}{2}u^2$ , and  $e = \frac{h}{\gamma}$ . A similar approach can be found in Harlow and Amsden [22]. We have not tried this approach.

## 6.4 Iterative solver: preconditioned GMRES

Per time step three systems of equations have to be solved. First, the system of discrete energy equations (6.4), then the system of discrete predictor momentum equations (6.5), and finally, the system of discrete pressure correction equations (6.7). The momentum correction and the density are found by substitution. The size of the system of discrete energy and pressure correction equations is  $n \times n$ , with  $n$  the total number of grid cells in the domain. Because a staggered grid is used, the number of  $m^\alpha$  grid points is slightly different from  $n$ . The total number of unknowns in the momentum equations is roughly  $nd$ , with  $d$  the number of space dimensions. The size of the system of the momentum equations also depends on the number of dimensions of the grid.

### GMRES

All three systems were solved by a Krylov subspace iterative method for unsymmetric matrices, namely GMRES. This method has been designed by Saad en Schultz [60] and applied to the incompressible flow Navier-Stokes equations in [80, 81, 87]. GMRES is a numerically stable method without possibility of breakdown. It is based on long recurrences and has certain optimality properties. The long recurrences imply that the amount of work per iteration and the required memory grow for increasing number of iterations. Consequently in practice one cannot afford to run the full algorithm, and it becomes necessary to use restarts or to truncate vector recursions. For GMRES we see in many cases superlinear convergence behaviour.

In order to improve the convergence behaviour of GMRES, preconditioners were

used. Since in our method only systems for one variable at a time need to be solved, different preconditioners could be chosen for the different systems. Both for solution of the energy and pressure equation the ILU preconditioner was used, whereas for the momentum equations ILUD sufficed. ILUD is the ILU decomposition with only the diagonal updated each time step. For further details see [80, 81, 87]

It is common to use the reduction of the residual as a stopping criterion, because GMRES requires calculation of the residual. Let the system to be solved be denoted by  $A\mathbf{x} = \mathbf{b}$ . After  $k$  iterations we have an approximate solution  $\mathbf{x}^{(k)}$  and the residual  $\mathbf{r}^{(k)} = \mathbf{b} - A\mathbf{x}^{(k)}$  is related to the error  $\epsilon = \mathbf{x} - \mathbf{x}^{(k)}$  by  $A\epsilon^{(k)} = \mathbf{r}^{(k)}$ . Hence, reduction of the residual results in reduction of the convergence error. The GMRES process stops at each time step if the ratio of the residual norm to the initial residual norm is small enough:  $\frac{\|\mathbf{r}^{(k)}\|_2}{\|\mathbf{r}^{(0)}\|_2} < tol$ . Here *tol* usually is of the order  $10^{-3}$  for both the momentum and energy equation and of order  $10^{-4}$  for the pressure equation. This appears to be a good stopping criterion, for further details see Vuik [80, 81].

In the subsonic case, the spatial discretisation is fully central and the time step must be small enough to sufficiently enhance the main diagonals of the systems for the mass flux components and enthalpy, if an implicit scheme is used. There is a trade-off here between size of time-step and number of iterations per time-step, as can be seen in Chapter 8. The pressure correction equation is always weakly diagonally dominant.





# 7

## Extension to the Navier-Stokes equations

In this chapter the viscous flow extension of the present method is given. Viscous flow is described by the Navier-Stokes equations, which will be non-dimensionalised, discretised and solved in the same way as described for the Euler equations in Chapters 4 to 6. The only difference with the Euler equations is the presence of the viscous stress term in the momentum equations and the heat diffusion and dissipation terms in the energy equation. In this chapter only instances where this leads to a difference with the previous analysis will be discussed. The presence of the viscous terms gives rise to a second dimensionless number: the Reynolds number.

### 7.1 Dimensionless equations

Viscous flow is described by the Navier-Stokes equations. The viscous momentum equation is equal to that of the Euler equation with a viscous stress term added. In the energy equation we will assume zero volumetric heat release, and neglect heat diffusion and dissipation of mechanical energy. The Navier-Stokes equations non-dimensionalised with the reference values discussed in Section 4.3 are:

$$\frac{\partial \rho}{\partial t} + (\rho u^\alpha)_{,\alpha} = 0, \quad (7.1)$$

$$\frac{\partial \rho u^\alpha}{\partial t} + (\rho u^\alpha u^\beta)_{,\beta} = -p_{,\alpha} + \left\{ \frac{1}{Re} (u_{,\beta}^\alpha + u_{,\alpha}^\beta - \frac{2}{3} u_{,\gamma}^\gamma \delta_{\alpha\beta}) \right\}_{,\beta}, \quad (7.2)$$

$$\frac{\partial h}{\partial t} + u^\alpha h_{,\alpha} = -(\gamma - 1) h u_{,\alpha}^\alpha, \quad (7.3)$$

with  $Re$  the Reynolds number defined by:

$$Re = \frac{\rho_0^* w_\infty^* L^*}{\mu^*}, \quad (7.4)$$

where  $\rho_0^*$ ,  $w_\infty^*$  and  $L^*$  are defined in Section 4.3.2. and  $\mu^*$  is the dynamic viscosity. The Reynolds number is a measure of the ratio of inertial forces (of order  $\rho_0^* w_\infty^{*2} / L^*$ )

and viscous forces (of order  $\mu^* w_\infty^* / L^{*2}$ ). For  $Re \gg 1$  inertia dominates, for  $Re \ll 1$  friction dominates. In the limit  $Re \rightarrow \infty$  the Euler equations are obtained.

## 7.2 Discretisation in general coordinates on a staggered grid

The difference with the Euler equations is the presence of the stress tensor in the momentum equation. Therefore, in this section the discretisation of the stress tensor in general coordinates on a staggered grid is described.

### Invariant formulation

First, the governing equations have to be recast in a form in which is invariant with respect to change of coordinates. The continuity (7.1) and energy equation (7.3) are the same as for inviscid flow, so that the coordinate invariant formulation is equal to eq. (5.1) and (5.3) in Section 5.1. Raising subscripts by contraction with the metric tensor the viscous momentum tensor equation valid in general coordinates is obtained in the same way as the inviscid momentum tensor equation:

$$\frac{\partial(\rho U)^\alpha}{\partial t} + ((\rho U)^\alpha U^\beta)_{,\beta} = -(g^{\alpha\beta} p)_{,\beta} + \tau_{,\beta}^{\alpha\beta}, \quad (7.5)$$

with  $\tau^{\alpha\beta}$  the deviatoric stress tensor given by

$$\tau^{\alpha\beta} = \frac{1}{Re} (g^{\alpha\gamma} U_{,\gamma}^\beta + g^{\gamma\beta} U_{,\gamma}^\alpha - \frac{2}{3} U_{,\gamma}^\gamma g^{\alpha\beta}). \quad (7.6)$$

Furthermore, for  $T_{,\beta}^{\alpha\beta}$ , some second order tensor, the expression is given in (5.8).

### The discretisation of the viscous stress tensor

Due to the presence of contravariant derivatives in the stress tensor, this part is the most complicated of all contributions to the momentum equations. Here the discretisation of the viscous stress term is discussed, for the discretisation of the other terms we refer to Chapter 5. The control volumes for the discretisation of the viscous momentum equations are the same as for the inviscid momentum equations, described in Section 5.2.2. The first momentum equation, (7.2) with  $\alpha = 1$ , is given by

$$\frac{\partial(\rho U)^1}{\partial t} + ((\rho U)^\beta U^1)_{,\beta} = -(g^{1\beta} p)_{,\beta} + \frac{1}{Re} (g^{1\gamma} U_{,\gamma}^\beta + g^{\gamma\beta} U_{,\gamma}^1 - \frac{2}{3} U_{,\gamma}^\gamma g^{1\beta})_{,\beta} \quad (7.7)$$

The control volume for the discretisation of the first momentum equation in point  $[x_{i-1/2}, y_j, t_{n+1}]$ , for  $i = 2, \dots, M$ ;  $j = 2, \dots, N-1$ , is shown in Figure 5.4. Using (5.7) integration of the viscous stress term in the first momentum equation over  $\Omega_{i-1/2,j}$ , gives:

$$\int_{\Omega_{i-1/2,j}} \tau_{,\beta}^{1\beta} d\Omega \approx \int_{\Omega_{i-1/2,j}} \frac{1}{\sqrt{g}} \frac{\partial \sqrt{g} \tau^{1\beta}}{\partial \xi^\beta} d\Omega + \int_{\Omega_{i-1/2,j}} \left\{ \frac{1}{\beta\gamma} \right\} \tau^{\beta\gamma} d\Omega = \quad (7.8)$$

$$\begin{aligned}
& \int_{G_{i-1/2,j}} \frac{\partial \sqrt{g} \tau^{1\beta}}{\partial \xi^\beta} d\xi^1 d\xi^2 + \int_{G_{i-1/2,j}} \sqrt{g} \left\{ \begin{matrix} 1 \\ \beta\gamma \end{matrix} \right\} \tau^{\beta\gamma} d\xi^1 d\xi^2 = \\
& \sqrt{g} \tau^{11} \Big|_{(i-1,j)}^{(i,j)} + \sqrt{g} \tau^{12} \Big|_{(i-1/2,j-1/2)}^{(i-1/2,j+1/2)} + \left\{ \begin{matrix} 1 \\ \beta\gamma \end{matrix} \right\} \tau^{\beta\gamma} \sqrt{g} \Big|_{(i-1/2,j)} = \\
& 2 \frac{1}{Re} \sqrt{g} (g^{11} U_{,1}^1 + g^{12} U_{,2}^1 - \frac{1}{3} (U_{,1}^1 + U_{,2}^2)) \Big|_{(i-1,j)}^{(i,j)} + \\
& \left[ \frac{1}{Re} (g^{11} U_{,1}^2 + g^{22} U_{,2}^1 + g^{12} U_{,1}^1 + g^{12} U_{,2}^2) \right] \Big|_{(i-1/2,j-1/2)}^{(i-1/2,j+1/2)} + \left\{ \begin{matrix} 1 \\ \beta\gamma \end{matrix} \right\} \tau^{\beta\gamma} \sqrt{g} \Big|_{(i-1/2,j)}.
\end{aligned}$$

Rewriting equation (7.8) in terms of the momentum components  $\rho V^\alpha = \rho \sqrt{g} U^\alpha$  to be computed, we get

$$\begin{aligned}
\int_{\Omega_{i-1/2,j}} \tau_{,\beta}^{1\beta} d\Omega & \approx 2 \frac{1}{Re} \sqrt{g} \left\{ g^{11} \left( \frac{1}{\sqrt{g\rho}} (\rho V^1)_{,1} \right) + g^{12} \left( \frac{1}{\sqrt{g\rho}} (\rho V^1)_{,2} \right) - \right. \\
& \left. \frac{1}{3} \left( \left( \frac{1}{\sqrt{g\rho}} (\rho V^1)_{,1} + \left( \frac{1}{\sqrt{g\rho}} (\rho V^2)_{,2} \right) \right) \right) \Big|_{(i-1,j)}^{(i,j)} + \right. \\
& \left. \frac{1}{Re} \left\{ g^{11} \left( \frac{1}{\sqrt{g\rho}} (\rho V^2)_{,1} \right) + g^{22} \left( \frac{1}{\sqrt{g\rho}} (\rho V^1)_{,2} \right) + g^{12} \left( \frac{1}{\sqrt{g\rho}} (\rho V^1)_{,1} \right) + \right. \right. \\
& \left. \left. g^{12} \left( \frac{1}{\sqrt{g\rho}} (\rho V^2)_{,2} \right) \right\} \Big|_{(i-1/2,j-1/2)}^{(i-1/2,j+1/2)} + \left\{ \begin{matrix} 1 \\ \beta\gamma \end{matrix} \right\} \tau^{\beta\gamma} \sqrt{g} \Big|_{(i-1/2,j)}. \tag{7.9}
\end{aligned}$$

The covariant derivative  $V_{,\beta}^\alpha$  is given by:

$$V_{,\beta}^\alpha = \frac{\partial V^\alpha}{\partial \xi^\beta} + \left\{ \begin{matrix} \alpha \\ \gamma\beta \end{matrix} \right\} V^\gamma, \tag{7.10}$$

which introduces extra Christoffel symbols. For the second momentum equation,  $\alpha = 2$ , finite volume integration takes place over a control volume  $\Omega_{i,j-1/2}$  centered at a  $V^2$  point. Further details need not be given, because the method followed is the same as for  $\alpha = 1$ .

Note that due to the presence of Christoffel symbols the mapping should be twice differentiable. In practice it has been found, see Zijlema [90], that accurate results are obtained if the grid points are smoothly distributed in the physical domain, even though the coordinate mapping has been constructed to be piecewise bi- or trilinear. However, for practical purposes it might be desirable to allow rapid changes of mesh-sizes. If this is the case the method described before can give inaccurate results. For inviscid computations mesh-size jumps did not lead to inaccuracies, while for viscous

computations some problems arose with the above discretisation, see Chapter 8. It is not surprising that viscous computations with our method suffer more from grid size jumps, since in those equations more Christoffel symbols appear. For grids with jumps in mesh-size an improved discretisation was developed for the incompressible flow Navier-Stokes equations as described in [85, 83, 90]. The implementation of this improved discretisation for the compressible Navier-Stokes equations did not receive priority, since we concentrate on the Euler equations, where we did not suffer from aforementioned inaccuracies, so that it is not finished yet. Therefore, the improved discretisation will not be discussed here.

### 7.3 Solution strategy

#### Time discretisation by the $\theta$ -method

For brevity, we leave the spatial derivatives undiscretised, assume Cartesian coordinates and write  $m^\alpha$  for  $\rho U^\alpha$ . In practice we discretise in space in general coordinates and incorporate the boundary conditions before discretising in time. The viscous momentum equations are discretised in time as follows:

$$\begin{aligned} & \frac{(m^\alpha)^{n+1} - (m^\alpha)^n}{\delta t} + \theta ((m^\alpha)^{n+1} (u^\beta)^n)_{,\beta} + (1 - \theta) ((m^\alpha)^n (u^\beta)^n)_{,\beta} = \\ & - (g^{\alpha\beta} (\theta p^{n+1} + (1 - \theta) p^n))_{,\alpha} + \frac{\theta}{Re} \left( (u^\alpha)_{,\beta}^{n+1} + (u^\beta)_{,\alpha}^{n+1} - \frac{2}{3} \delta_{\alpha\beta} (u^\gamma)_{,\gamma}^{n+1} \right)_{,\beta} \\ & + \frac{1 - \theta}{Re} \left( (u^\alpha)_{,\beta}^n + (u^\beta)_{,\alpha}^n - \frac{2}{3} \delta_{\alpha\beta} (u^\gamma)_{,\gamma}^n \right)_{,\beta}. \end{aligned}$$

#### Original pressure correction method

The pressure correction method is the same as for the Euler equations described in Section 6.2 except for the predictor momentum equation. After solving the viscous predictor momentum equation:

$$\begin{aligned} & \frac{(m^\alpha)^* - (m^\alpha)^n}{\delta t} + \theta ((m^\alpha)^* (u^\beta)^n)_{,\beta} + (1 - \theta) ((m^\alpha)^n (u^\beta)^n)_{,\beta} = \\ & - (g^{\alpha\beta} p^n)_{,\alpha} + \frac{\theta}{Re} \left( (u^\alpha)_{,\beta}^* + (u^\beta)_{,\alpha}^* - \frac{2}{3} \delta_{\alpha\beta} (u^\gamma)_{,\gamma}^* \right)_{,\beta} \\ & + \frac{1 - \theta}{Re} \left( (u^\alpha)_{,\beta}^n + (u^\beta)_{,\alpha}^n - \frac{2}{3} \delta_{\alpha\beta} (u^\gamma)_{,\gamma}^n \right)_{,\beta}. \end{aligned}$$

the pressure correction equation (6.7) is solved. In the derivation of this equation not only the difference in convection terms, but also the difference in diffusion terms is neglected. Van Kan [74] has shown for the incompressible flow case that neglecting both terms does not affect the temporal order of accuracy, and  $\theta = 1/2, \mu = 1$  gives second order accuracy in time. Once the pressure correction  $\delta p = p^{n+1} - p^n$  is found, the momentum can be computed from (6.6). The rest of the solution process is described in Section 6.2.2. Just as for the Euler equations the systems of discrete Navier-Stokes equations are solved by preconditioned GMRES, see Section 6.4.



## **Part III**

# **Results obtained with the present method**





## 8

# Demonstration of Mach-uniform accuracy and efficiency

In this chapter we will show that flows with Mach numbers varying from 0 to supersonic can be efficiently and accurately computed. Two stationary test problems especially suited for testing computing methods with varying Mach numbers have been selected. The first is flow through a channel with a bump, also treated in [17, 65, 34, 33]. The second is flow through a converging-diverging nozzle, also treated by Shuen et al. [63]. The parameters are chosen such that regions with very low and medium or high Mach numbers occur simultaneously in the flow domain. Standard methods for computing incompressible or compressible flow cannot cope with these flows, or at best in an inefficient manner. Also a nonstationary nozzle flow is computed to show that the scheme is suitable for nonstationary weakly and fully compressible flow. Validation of the method by testing on fully compressible nonstationary Riemann problems is described in the following chapter.

Reports on some of our experiments have been published in [6, 7, 8, 9, 5, 10].

### 8.1 Channel with bump

Results for inviscid flow in channels with bumps with inlet Mach numbers from 0 to 1.65 will be shown. Also a result for subsonic viscous flow will be shown. Mach-uniform efficiency follows from timings performed for all subsonic computations. We use time-stepping starting from rest to converge to steady state, with  $\theta = 1$  and  $\mu = 1$ . The following termination criterion is used:  $\max_{i,j} ((U_{i,j}^\alpha)^{n+1} - (U_{i,j}^\alpha)^n) \leq 10^{-6} \delta t$ . First, it will be shown that the present method gives for fully incompressible flow with  $M_\infty = 0$  exactly the same results as a method for incompressible flows.

### 8.1.1 Inviscid incompressible flow

In this section results for the present method for flows at all speeds with  $M_\infty = 0$ , that is with infinite speed of sound, will be compared with results obtained with the method for incompressible flow described in [90, 93, 94] of which the present method is an extension. The present method was designed such that in the limit  $M \downarrow 0$  this method for incompressible flow is recovered. This is tested in this section. Note that the original method for incompressible flow is based on the assumption  $\rho = \text{constant}$  and on the incompressible flow equations.

Inviscid fully incompressible flow, with  $M_\infty = 0$ , in a channel with a bump equal to 10% of the channel height is computed. All equations are discretised using central differences. The size of the channel is  $[0, 3] \times [0, 1]$ , in which a boundary fitted nonuniform grid of  $63 \times 22$  cells is generated, see Figure 8.1. The boundary conditions are:  $\alpha_\infty = 0$  (i.e. the inlet flow angle is equal to zero), and  $p_v = 1$ . From the iso-pressure lines resulting from computations of the present method for compressible flow, shown in Figure 8.2, it can be seen that the computed solution is symmetric, as it should be for incompressible flow. In Figure 8.3 the pressure coefficient along the upper and lower boundary of the channel computed by the present method is compared with the pressure coefficient resulting from the method for incompressible flows, described by Zijlema [90]. The pressure coefficient equal to  $p - p_{out}$  computed with the present method is exactly the same as the pressure coefficient computed by the method for incompressible flows. What is more, exactly the same number, that is 203, of time steps was required to converge to steady state. This is as it should be, since in the limit  $M \downarrow 0$  the method for incompressible flow should be recovered.

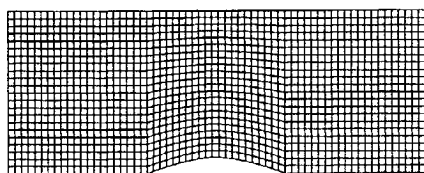


Figure 8.1: Grid of size  $63 \times 22$  used for subsonic and transonic computations

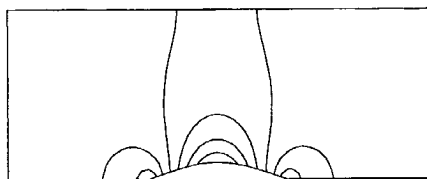


Figure 8.2: Isobars for  $M_\infty = 0$

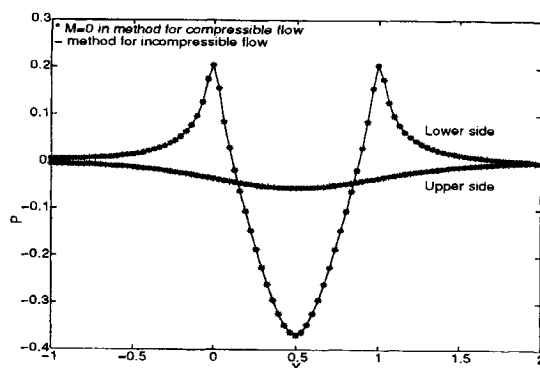


Figure 8.3: Pressure coefficient at upper and lower boundary of channel with bump for  $M_\infty = 0$  compared with the equivalent method for incompressible flows

### 8.1.2 Inviscid subsonic flow

The same boundary fitted nonuniform grid of  $63 \times 22$  cells is used as for the fully incompressible computations, see Figure 8.1. In this section results are given for  $M_\infty = 10^{-6}, 0.01, 0.1,$  and  $0.5$ . The boundary conditions are:  $\alpha_\infty = 0, p_v = 1$ . For an inlet Mach number of  $M_\infty = 1 \cdot 10^{-6}$  and  $0.5$  the resulting iso-Mach lines are shown in Figure 8.4 and Figure 8.5. Note that the pattern is symmetric, as it should be for subsonic flow through the specified channel. The computed Mach number distributions on the upper and lower boundary of the channel are compared to results obtained by Eidelman et al. [17] in Figure 8.6. The results are very similar. Our central scheme gives better symmetry than the (much more computationally intensive) second order upwind-biased Godunov scheme of [17], and contains less numerical diffusion, resulting in a 4% higher maximum Mach number.

#### *Efficiency at low Mach numbers*

The number of iterations and CPU time (using an HP9000-735 workstation) required are listed in Table 8.1. Neither the number of iterations nor the CPU time deteriorate at low Mach numbers. For increasing Mach numbers the flow takes more time to settle down to steady state, but CPU time per time step does not increase (in fact, decreases somewhat).

### 8.1.3 Inviscid transonic flow

Although our primary aim is to cover the no-man's land between incompressible and compressible flow, we show in the following examples that the present staggered grid pressure correction method is quite suitable for compressible flow as well. In the channel discussed above we take  $M_\infty = 0.675$  and obtain transonic flow. In regions of transonic flow the upwind-biased evaluation of the density as explained in Chapter 5.7

Table 8.1: Channel with 10% bump,  $\delta t = 0.1$

Mach	CPU [s]	time steps	GMRES iterations	
			total	iter/t.step
0.5	151	509	6108	12
0.1	73	220	3960	18
0.01	74	200	4200	21
$10^{-6}$	74	200	4200	21
0	75	203	4263	21

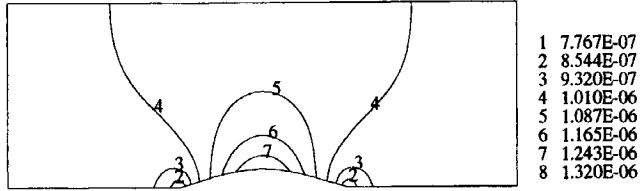


Figure 8.4: Mach number contour plot for  $M_\infty = 1.10^{-6}$

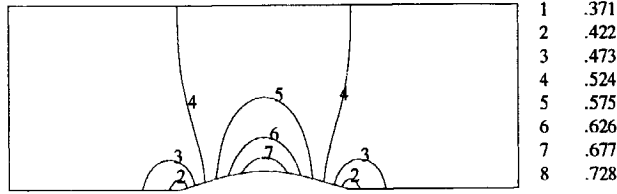


Figure 8.5: Mach number contour plot for  $M_\infty = 0.5$

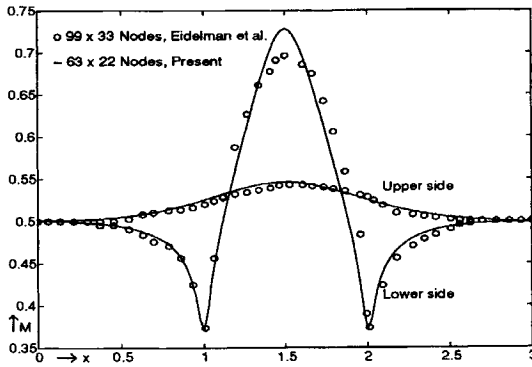


Figure 8.6: Mach number at upper and lower boundary of channel with bump for  $M_\infty = 0.5$  compared with a second order Godunov method

is used. Furthermore, for the energy equation a first order upwind scheme is employed. Again, a boundary fitted grid of  $63 \times 22$  cells is used, see Figure 8.1. Mach number contours are shown in Figure 8.7. The location of the shock was at 70% of the bump, while Eidelman et al. [17] found the shock to be at 72%. The maximum Mach number is 1.33 against 1.32 in [17]. This agreement is quite satisfactory. At the bump, the shock is captured in 4 cells. We see that the staggered scheme is accurate for transonic flow. Computing time was a bit higher than for  $M_\infty = 0.5$ .

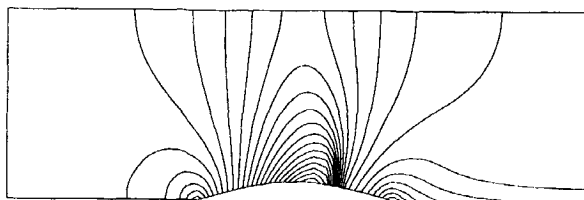


Figure 8.7: Mach number contour plot for  $M_\infty = 0.675$ ,  $\Delta M = 0.036$

#### 8.1.4 Inviscid supersonic flow

Supersonic flow is computed for a channel with 4% bump and  $M_\infty = 1.65$ . For this type of flow the first order upwind scheme is used for the momentum and energy equations. In Figure 8.9 the Mach number contours are shown for the computation on a  $190 \times 55$  grid, shown in Figure 8.8. The leading edge shock reflects from the top wall and intersects with the shock leaving the trailing edge. All shocks are resolved fairly well, although the reflecting one is somewhat smeared, as is to be expected with a first order upwind method. In Figure 8.9 a few dents in the Mach contours above the right corner of the bump can be observed. These dents might be due to the discretisation in general coordinates. As discussed in Section 5.2, some geometrical quantities, such as the Christoffel symbols, are discontinuous at cell faces, which may lead to problems on irregular grids. When the improved discretisation is used the dents should disappear. In Figure 8.10 one can see that the agreement between our first order accurate results and the results for the second order Godunov method in [17] (where the grid size is not mentioned) is good; locations of the shocks are the same. Furthermore, it is interesting to note that the shock position does not change with grid refinement, see Figure 8.11. The shocks we computed are as sharp as in [17], except for the reflected shock on the upper boundary in the neighbourhood of  $x = 2$ , and our extreme values are lower than those in [17]. This is most likely due to the use of a first order upwind scheme for the momentum equations. Compared to the results in [17] for a first order Godunov method it is found that the present scheme gives better crispness of resolution. A second order upwind-biased scheme with a limiter can be easily implemented, but our aim here is merely to show the suitability of our scheme for computing supersonic flow.

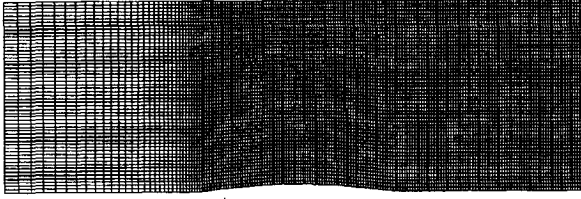


Figure 8.8: Grid size  $190 \times 55$  used for supersonic computations.

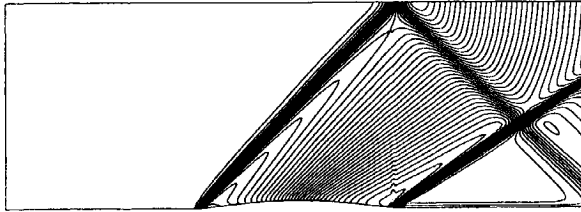


Figure 8.9: Mach number contour plot for  $M_\infty = 1.65$ ,  $\Delta M = 0.14$

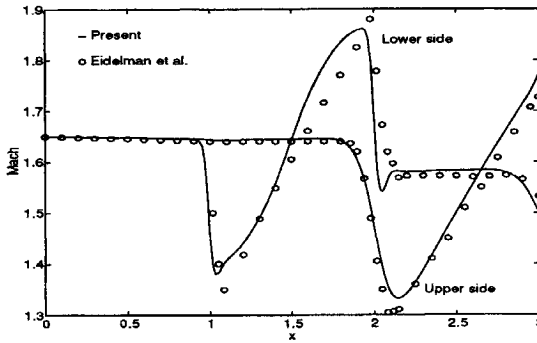


Figure 8.10: Mach number at upper and lower boundary of channel with bump for  $M_\infty = 1.65$  compared with a second order Godunov method

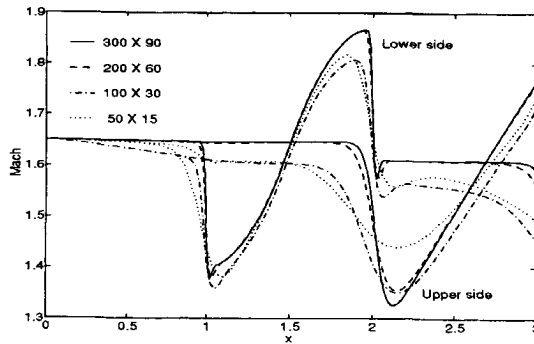


Figure 8.11: Mach number at upper and lower boundary of channel with bump with  $M_\infty = 1.65$  for different grid sizes

### 8.1.5 Viscous subsonic flow

Extension to the Navier-Stokes equations is discussed in Chapter 7. We give results for the channel with 10% bump with a uniform inlet Mach number of 0.45, just as the case studied by Shyy in [64]. The grid of  $99 \times 49$  cells is refined near the wall, see Figure 8.12. A laminar flow computation was performed for a Reynolds number of  $4 \times 10^5$ . The resulting Mach number contours are shown in Figure 8.13. These contours are very similar to the results obtained by Shyy [64], except for the dents in the contour line crossing the channel, and in the contour line occurring in the center of the channel near the outlet. These deviations are caused by the discretisation in general coordinates. As discussed in Section 5.2, some geometrical quantities, such as the Christoffel symbols, are discontinuous at cell faces, which may lead to problems on non-uniform grids. Since when written in general coordinates the Navier-Stokes equations have more Christoffel symbols than the Euler equations, this problem is encountered here. When the improved discretisation is used the dents will disappear. This was tested for incompressible flows only, since for compressible flows the improved discretisation is not implemented yet. The thickness of the computed boundary layer is in agreement with results in Shyy [64]. The velocity vectors near the right corner of the bump, shown in Figure 8.14 is also similar to the laminar results obtained by Shyy [64].

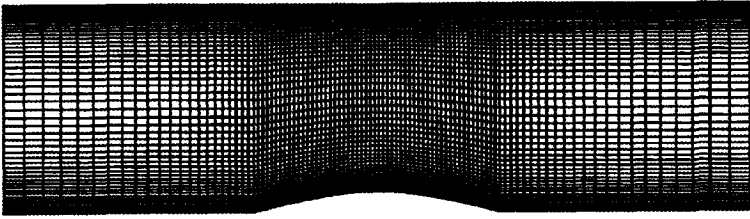


Figure 8.12: Grid of size  $99 \times 49$  used for viscous computation

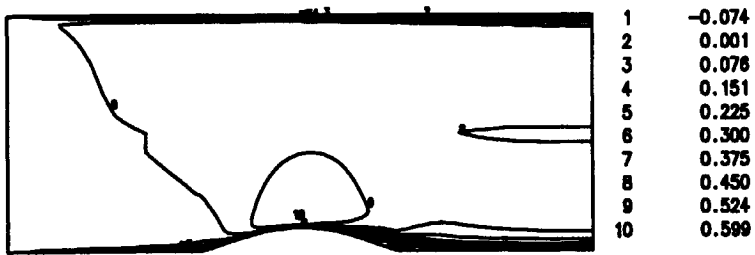


Figure 8.13: Mach number contours for  $M_\infty = 0.45$  and  $Re = 4 \times 10^5$ .

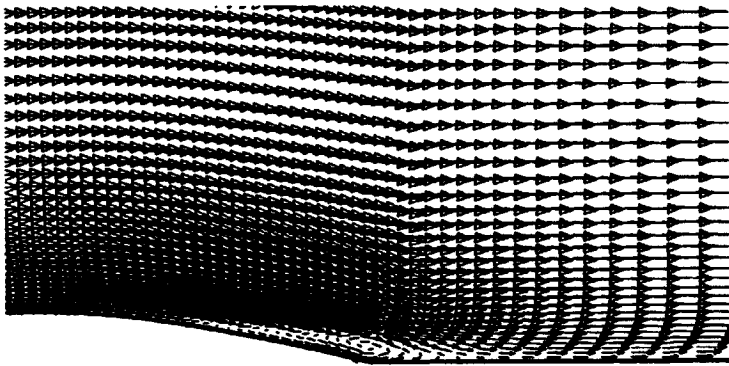


Figure 8.14: Velocity vectors near the right corner of the bump  $M_\infty = 0.45$  and  $Re = 4 \times 10^5$ .



## 8.2 Converging-diverging nozzle

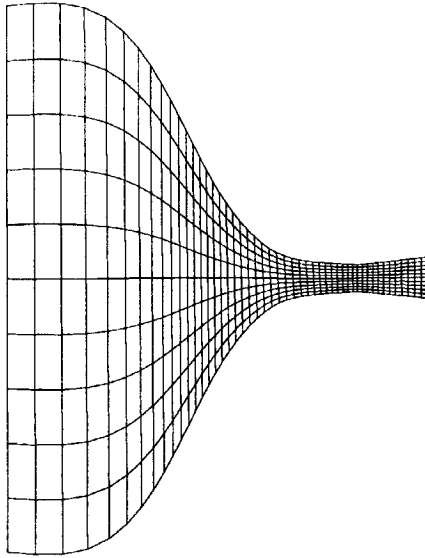
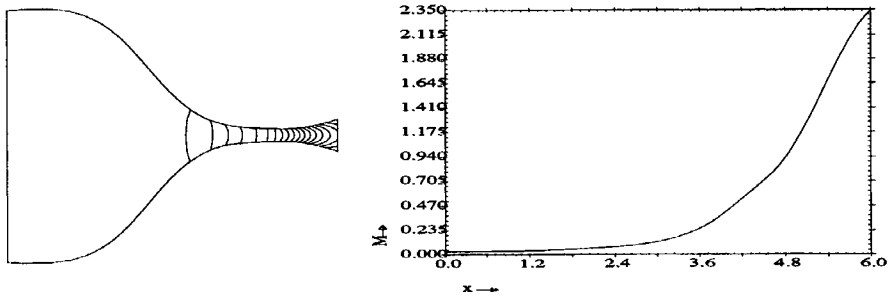
Next, the flow is computed in a converging/diverging nozzle with the following contraction ratios: 5, 10, and 20. We use time-stepping starting from rest to converge to steady state, with  $\theta = 0.5$  and  $\mu = 1$ , with the following termination criterion:  $\max_{i,j} ((U_{i,j}^\alpha)^{n+1} - (U_{i,j}^\alpha)^n) \leq 10^{-6} \delta t$ . The inlet Mach number is kept constant at 0.045. The height of the throat is kept constant at 0.4, and the height of the outlet is kept constant at 2.5 times the height of the throat. For all computations we have used a  $49 \times 10$  nonuniform grid of the type shown in Figure 8.15. The time step was kept constant at  $\delta t = 0.01$ . First order upwind discretisation was used both in the energy and in the momentum equations. In the computations for the flow in nozzles with contraction ratios 5 and 10, the pressure ratio was chosen as  $p_v = 1$ , and the flow remained subsonic. The maximum Mach numbers that occurred are listed in Table 2. For a contraction ratio of 15 and 20,  $p_v = 60$  was chosen so that supersonic outflow occurred. In this case a large range of Mach numbers from 0.045 up to 2.34 arose, see Figure 8.16. Such a flow cannot be computed by standard methods for compressible flow, due to the presence of a low-Mach number flow region of significant size. When the solution is computed on a grid with four times as many grid cells, the solution did not change. To obtain convergence on this grid, the time step had to be halved to 0.005.

### *Efficiency at low Mach numbers*

In the nozzle with a contraction ratio of 5 the flow remains virtually incompressible. The maximum Mach number is 0.25. For a contraction ratio of 10 the maximum Mach number is 0.53, for 15 it is 1.82, and for 20 it is 2.67. The CPU time and number of iterations for the nozzle do not increase significantly for lower Mach numbers, that is smaller contraction ratios. On the contrary, there is an increase of computing time with increasing contraction ratio. This increase of CPU time is caused by the fact that the flow takes longer to settle down to steady state. But the results suffice to illustrate our main point, namely that accuracy and efficiency do not degrade in the presence of low Mach numbers.

Table 8.2: Nozzle with inlet Mach number of 0.045,  $\delta t = 0.01$

contraction ratio	maximum Mach nr.	CPU [s]	time steps	GMRES iterations	
				total	iter/t.step
20	2.67	761	6792	95088	14
15	1.82	750	6790	95060	14
10	.53	220	1866	26124	14
5	.25	300	2744	38416	14

Figure 8.15: Grid of size  $49 \times 10$ Figure 8.16: Nozzle with contraction ratio of 20,  $p_v = 60$ ; a) Mach number contour plot for  $M_\infty = 0.045$ , b) Mach number at centerline of nozzle

*Nonstationary nozzle*

As stated before, one of the advantages of our method over preconditioning methods is that in our method the transient behaviour is not falsified. We will show that nonstationary compressible flows can be computed accurately with two test examples. The first example is a standard test for compressible flow codes, namely the shock tube problem, which will be discussed in the next chapter. The second test example is a nonstationary flow in a nozzle with low Mach numbers. We have computed the flow in the converging/diverging nozzle with a contraction ratio of 5 with nonstationary inflow. The inlet Mach number  $M_\infty$  varied between 0 and 0.045 with a period of 0.5 s. Furthermore,  $\mu = 1$ , and  $\theta = 1$ . The time step was 0.001. The resulting Mach number plot between  $t = 20$  and  $t = 21$  is shown in Figure 8.17. In Figure 8.18 the Mach number at the centerline of the nozzle at  $t = 20$  is plotted for time steps equal to 0.1, 0.01, and 0.001. There it can be seen that for the instationary nozzle flow convergence to the solution is obtained only with a time step  $\delta t \leq 0.01$ . We see that weakly compressible nonstationary flow is computed without trouble.

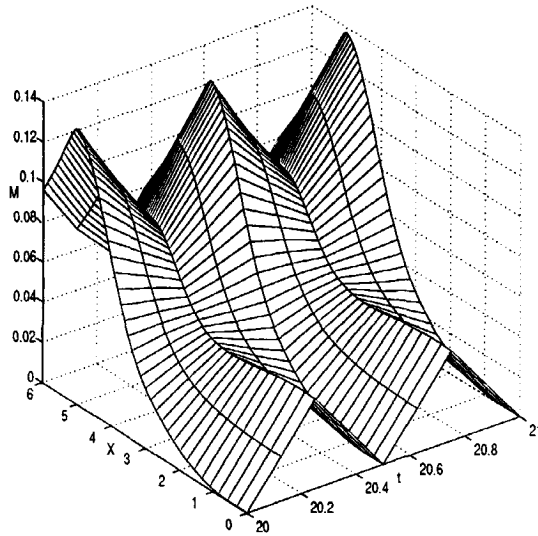


Figure 8.17: Nonstationary nozzle: Mach number distribution along centerline,  $\delta t = 0.001$ .

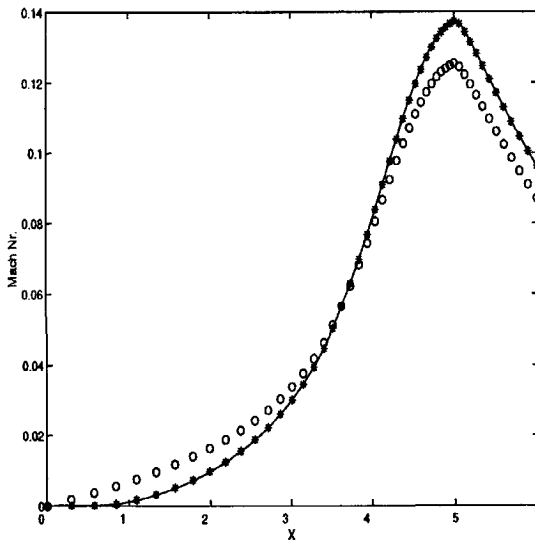


Figure 8.18: Nonstationary nozzle: Mach number distribution along centerline at  $t = 20$  computed with  $\delta t = 0.1(o)$ ,  $\delta t = 0.01(*)$ , and  $\delta t = 0.001(-)$

## 9

# Validation for Riemann problems

As stated before, one of the advantages of our method over preconditioning methods is that in our method the transient behaviour is not falsified. In this chapter we will discuss applications with time dependence. For an important standard test case for compressible codes, namely the Riemann problem, we will compare the solution obtained with the present staggered method with the exact solution and with the numerical solution obtained with the Osher method, which has a solid theoretical foundation and for which convergence to the correct weak solution has been proved in [51]. Such a solid theoretical foundation is the exception rather than the rule for numerical schemes for nonlinear hyperbolic systems. Also for the present staggered scheme there is no proof of convergence available. Therefore, we validate the scheme by application to Riemann problems, for which exact solutions are available. Quality is judged by comparison of our results with those of the Osher scheme, which is known to be quite accurate. We will find that the quality of the staggered scheme is comparable to that of the Osher scheme. Only in strong contact discontinuities the present method produces small wiggles.

First, analytical aspects of Riemann problems are discussed, and the computation of the exact solution is explained. Then, for four test cases results are shown for both the present staggered method and the Osher method. These test cases are: Sod's shock tube problem, the test case of Lax, a supersonic flow test case and a non-stationary contact discontinuity.

## 9.1 Analytical aspects

For the exact solution of the Riemann problem we need the jump conditions for shocks, contact discontinuities and expansion waves. Therefore, these conditions are derived before construction of the exact solution is discussed. For a more elaborate explanation of the theory we refer the reader to Anderson [1], and Liepmann and Roshko [42].

### 9.1.1 Stationary shock waves

We first consider a stationary normal shock wave separating state 1 and 2. For this case the equations for conservation of mass, momentum and energy are given by the Rankine-Hugoniot jump conditions:

$$\rho_1 u_1 = \rho_2 u_2, \quad (9.1)$$

$$p_1 + \rho_1 u_1^2 = p_2 + \rho_2 u_2^2, \quad (9.2)$$

$$h_1 + \frac{1}{2}u_1^2 = h_2 + \frac{1}{2}u_2^2, \quad (9.3)$$

where  $u_1$  is velocity of the gas ahead of the shock wave and  $u_2$  the velocity of the gas behind the shock wave. By manipulation of these equations (9.1)-(9.3) we can derive useful relations in the following way.

First, we divide Eq. (9.2) by Eq. (9.1), and with  $a^2 = \gamma p/\rho$  we obtain:

$$u_1 - u_2 = \frac{a_2^2}{\gamma u_2} - \frac{a_1^2}{\gamma u_1}. \quad (9.4)$$

Since  $h = c_p T = a^2/(\gamma - 1)$  Eq. (9.3) can be rewritten as:

$$\frac{1}{2}u_1^2 + \frac{1}{\gamma - 1}a_1^2 = \frac{1}{2}u_2^2 + \frac{1}{\gamma - 1}a_2^2. \quad (9.5)$$

The sonic condition is defined as the condition in which  $u = a$ , and is denoted by an asterisk. Hence, Eq. (9.5) can be written as:

$$\frac{1}{2}u_1^2 + \frac{1}{\gamma - 1}a_1^2 = \frac{1}{2}u_2^2 + \frac{1}{\gamma - 1}a_2^2 = \frac{\gamma + 1}{2(\gamma - 1)}a^{*2}. \quad (9.6)$$

Solution of  $a_1$  and  $a_2$  from Eq. (9.6) and substitution in (9.4) gives:

$$u_1 u_2 = a^{*2}. \quad (9.7)$$

This equation (called the Prandtl-Meyer relation) shows that either  $|u_1| > a^*$  and  $|u_2| < a^*$  or  $|u_2| > a^*$  and  $|u_1| < a^*$ , so that the flow at one side of the shock is always supersonic, while the flow at the other side is subsonic.

We will now show that the ratios of all quantities depend on only one parameter, for which we first will take the Mach number  $M_1 = u_1/a_1$ . Dividing (9.6) by  $u_1^2$ , we find for  $M_1^* = u_1/a^*$

$$M_1^{*2} = \frac{(\gamma + 1)M_1^2}{2 + (\gamma - 1)M_1^2}. \quad (9.8)$$

It follows from Eq. (9.1) and (9.7) that

$$\frac{\rho_2}{\rho_1} = \frac{u_1}{u_2} = \frac{u_1^2}{u_1 u_2} = \frac{u_1^2}{a^{*2}} = M_1^{*2}. \quad (9.9)$$

Substituting Eq. (9.8) into (9.9), we obtain

$$\frac{\rho_2}{\rho_1} = \frac{u_1}{u_2} = \frac{(\gamma + 1)M_1^2}{2 + (\gamma - 1)M_1^2}. \quad (9.10)$$

To obtain the pressure ratio, we return to the momentum equation (9.2), which combined with Eq. (9.1) yields

$$p_2 - p_1 = \rho_1 u_1 (u_1 - u_2) = \rho_1 u_1^2 \left(1 - \frac{u_2}{u_1}\right). \quad (9.11)$$

Dividing this equation by  $p_1$ , and recalling  $a_1^2 = \gamma p_1 / \rho_1$ , we obtain

$$\frac{p_2 - p_1}{p_1} = \gamma M_1^2 \left(1 - \frac{u_2}{u_1}\right), \quad (9.12)$$

which simplifies to

$$\frac{p_2}{p_1} = 1 + \frac{2\gamma}{\gamma + 1} (M_1^2 - 1). \quad (9.13)$$

Equation (9.13) can be solved for  $M_1^2$  to give

$$M_1^2 = 1 + \frac{\gamma + 1}{2\gamma} \left(\frac{p_2}{p_1} - 1\right). \quad (9.14)$$

With this equation  $M_1^2$  in Eq. (9.10) can be replaced, so that all variables can also be expressed depending solely on the pressure ratio  $p_2/p_1$ , instead of the Mach number  $M_1$ . This pressure ratio is also called the shock strength. For the ratio of densities and velocities this gives:

$$\frac{\rho_2}{\rho_1} = \frac{u_1}{u_2} = \frac{(\gamma + 1) \left[1 + \frac{\gamma + 1}{2\gamma} \left(\frac{p_2}{p_1} - 1\right)\right]}{2 + (\gamma - 1) \left[1 + \frac{\gamma + 1}{2\gamma} \left(\frac{p_2}{p_1} - 1\right)\right]}, \quad (9.15)$$

which can be rewritten as

$$\frac{\rho_2}{\rho_1} = \frac{u_1}{u_2} = \frac{1 + \frac{\gamma + 1}{\gamma - 1} \frac{p_2}{p_1}}{\frac{\gamma + 1}{\gamma - 1} + \frac{p_2}{p_1}}. \quad (9.16)$$

To obtain the temperature ratio, recall the equation of state  $p = \rho RT$ . Hence,

$$\frac{T_2}{T_1} = \left(\frac{p_2}{p_1}\right) \left(\frac{\rho_1}{\rho_2}\right). \quad (9.17)$$

When this is substituted into Eq. (9.16), we obtain

$$\frac{T_2}{T_1} = \frac{p_2}{p_1} \frac{\frac{\gamma + 1}{\gamma - 1} + \frac{p_2}{p_1}}{1 + \frac{\gamma + 1}{\gamma - 1} \frac{p_2}{p_1}}. \quad (9.18)$$

### 9.1.2 Moving normal shock waves

In the case of a shock moving with speed  $W$  the jump relations can be obtained from the jump relations for a stationary shock by regarding the velocities relative to the moving shock. The thermodynamic quantities do not change under this transformation, but the velocities  $u_1$  and  $u_2$  have to be taken relative to the moving shock, so that  $u_1$  and  $u_2$  have to be replaced by  $u_1 - W$ , the velocity ahead of the shock wave, relative to the wave, and  $u_2 - W$ , the velocity behind the shock wave, relative to the wave. That is, we switch to an observer moving with speed  $-W$ , who sees the originally stationary shock move with velocity  $W$ . As a result Eqs. (9.1) and (9.2) become

$$W(\rho_2 - \rho_1) = \rho_2 u_2 - \rho_1 u_1, \quad (9.19)$$

$$W(\rho_2 u_2 - \rho_1 u_1) = p_2 + (\rho_2 u_2)^2 / \rho_2 - p_1 - (\rho_1 u_1)^2 / \rho_1, \quad (9.20)$$

For  $W = 0$  we obtain the original stationary shock relations as derived above. With  $M_s = |u_1 - W|/a_1$  we obtain from Eq. (9.13):

$$\frac{p_2}{p_1} = 1 + \frac{2\gamma}{\gamma + 1}(M_s^2 - 1). \quad (9.21)$$

Hence,

$$M_s = \sqrt{1 + \frac{\gamma + 1}{2\gamma} \left( \frac{p_2}{p_1} - 1 \right)}. \quad (9.22)$$

As a result, the shock speed  $W$  is equal to:

$$W = u_1 + a_1 \sqrt{1 + \frac{\gamma + 1}{2\gamma} \left( \frac{p_2}{p_1} - 1 \right)}. \quad (9.23)$$

Equation (9.23) relates the wave velocity of the moving shock wave to the pressure ratio across the wave and the speed of sound of the gas into which the shock is propagating. For the velocity behind the shock wave we find

$$u_2 = \frac{\rho_1}{\rho_2}(u_1 - W) + W = W \left( 1 - \frac{\rho_1}{\rho_2} + \frac{u_1}{W} \right). \quad (9.24)$$

### 9.1.3 Expansion fans

Next we consider an expansion fan as shown in Figure 9.1. The head of the expansion wave moves to the left into region 4, the tails borders on region 3. The expansion wave is assumed to be a left-travelling wave. Within the expansion wave, the induced velocity is  $u$ , and is directed to the right. The temperature and hence  $a$  is reduced inside the wave. Therefore, although the head of the wave advances into region 4 with the speed of sound other parts of the wave propagate at slower velocities. Note that the tail



of the wave propagates at the velocity  $dx/dt = u_3 - a_3$ .

In Fig. 9.1 the  $C_-$  and  $C_+$  characteristics, which are defined as:

$$J_+ = u + \frac{2a}{\gamma - 1} = \text{constant (along a } C_+ \text{ characteristic)} \quad (9.25)$$

$$J_- = u - \frac{2a}{\gamma - 1} = \text{constant (along a } C_- \text{ characteristic)}, \quad (9.26)$$

are shown. From Eqs. (9.25) and (9.26) it follows that

$$a = \frac{\gamma - 1}{4}(J_+ - J_-), \quad u = \frac{1}{2}(J_+ + J_-). \quad (9.27)$$

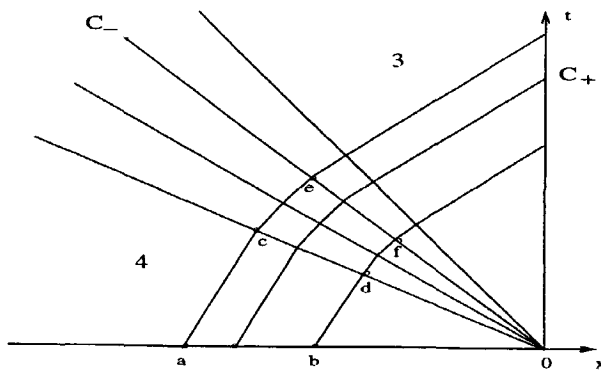


Figure 9.1:  $C_+$  and  $C_-$  characteristics in  $x - t$  diagram of an expansion wave

We now will show that the  $C_-$  characteristics for left moving expansion fans are straight lines, as drawn in Fig 9.1. In the constant property region 4,  $u_4$  and  $a_4$  are constant. Thus, in region 4, all  $C_+$ -characteristics have the same slope. Moreover,  $J_+$  is the same everywhere in region 4. Hence, considering two points  $a$  and  $b$  in Fig 9.1, we have

$$(J_+)_a = (J_+)_b. \quad (9.28)$$

However, a constant value of  $J_+$  is carried along a  $C_+$  characteristic. Hence, in Fig. 9.1 we see that

$$(J_+)_a = (J_+)_c = (J_+)_e, \quad (J_+)_b = (J_+)_d = (J_+)_f. \quad (9.29)$$

Comparing Eq. (9.28) with (9.29) we find

$$(J_+)_e = (J_+)_f. \quad (9.30)$$

Points  $e$  and  $f$  are by definition on the same  $C_-$  characteristic, so that

$$(J_-)_e = (J_-)_f. \quad (9.31)$$

Thus, substituting Eqs. (9.30) and (9.31) into (9.27) we have,  $a_e = a_f$  and  $u_e = u_f$ . With this we have shown that the values of  $u$  and  $a$  (and hence of  $\rho, p, T$ ) are constant along the  $C_-$  characteristic, since the slope  $dx/dt = u - a$  is the same at all points. Furthermore, we have shown that  $J_+$  is constant through the expansion wave. From Eq. (9.25), therefore,

$$u + \frac{2a}{\gamma - 1} = u_4 + \frac{2a_4}{\gamma - 1} = \text{constant through the wave.} \quad (9.32)$$

Consequently,

$$\frac{a}{a_4} = 1 + \frac{\gamma - 1}{2} \left[ \frac{u_4}{a_4} - \frac{u}{a_4} \right]. \quad (9.33)$$

Since the process is isentropic  $p/p_4 = (\rho/\rho_4)^\gamma$ , and since  $a^2 = \gamma p/\rho$  we have

$$\frac{p}{p_4} = \left[ 1 + \frac{\gamma - 1}{2} \left( \frac{u_4}{a_4} - \frac{u}{a_4} \right) \right]^{2\gamma/(\gamma-1)}. \quad (9.34)$$

### 9.1.4 Contact discontinuities

The interface between two gases is called a or contact surface. Across a contact discontinuity the entropy changes discontinuously, but the pressure and velocity are continuous. Suppose there is a contact discontinuity separating a gas in region 3 from a gas in region 2. This discontinuity travels with speed

$$u_2 = u_3 = W. \quad (9.35)$$

Substitution of this into the conservation equations (9.19) and (9.20) gives

$$\rho_2 - \rho_3 = \rho_2 - \rho_3 \quad (9.36)$$

$$W^2(\rho_2 - \rho_3) = W^2(\rho_2 - \rho_3) + p_2 - p_3. \quad (9.37)$$

It follows that  $p_2 = p_3$ , but  $\rho$  can jump.

### 9.1.5 Analytical solution of the Riemann problem

The Riemann problem consists of solving the one-dimensional Euler equations for a special class of initial conditions, namely a constant (left) state for  $-\infty < x < x_0$  and a different constant (right) state for  $x_0 < x < \infty$ . The left state will be indicated by subscript 4 and the right state will be indicated by subscript 1. So the initial conditions are:

$$\begin{aligned} u &= u_4, p = p_4, \rho = \rho_4, & x < x_0, t = 0; \\ u &= u_1, p = p_1, \rho = \rho_1, & x > x_0, t = 0. \end{aligned} \quad (9.38)$$

An important observation is that the complete solution of the Riemann problem is only a function of the ratio  $x/t$  and the initial conditions (9.38). The Riemann problem can be solved analytically using the exact jump conditions, discussed in the previous section, and the right order and presence of the following three phenomena: shocks, contact discontinuities, and expansion waves. This will be done here for the case  $p_4 > p_1$ . For the time being we take  $u_1 = 0$ . (If also  $u_4 = 0$  the Riemann problem is called the shock tube problem.)

We will assume that the solution consists of four states separated in the following way. States 1 and 2 are assumed to be separated by a shock, states 2 and 3 are assumed to be separated by a contact discontinuity, while state 3 and 4 are assumed to be separated by an expansion fan. The situation is sketched in Figure 9.2. If we succeed in solving the shock tube problem with this structure, then the assumed structure is correct. Now we will compute the exact solution of the shock tube, applying the appropriate jump conditions from the previous section to the separations of the states.

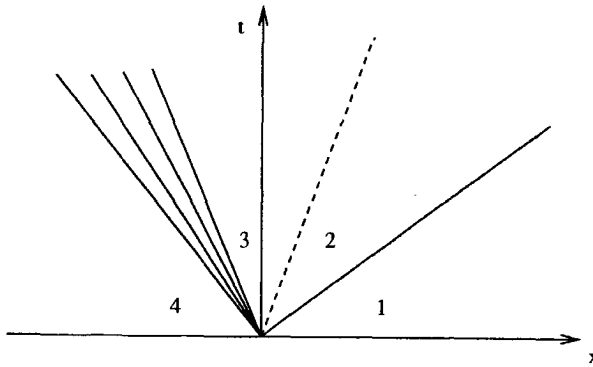


Figure 9.2:  $x - t$  diagram of solution of the Riemann problem, with an expansion fan, contact discontinuity (- -) and shock (-)

### Shock

We start with the shock separating region 1 and 2. Substituting Eq. (9.15) and (9.23) into (9.24), with  $u_1 = 0$  we find for  $u_2$ :

$$u_2 = \frac{a_1}{\gamma_1} \left( \frac{p_1}{p_2} - 1 \right) \left( \frac{\frac{2\gamma_1}{\gamma_1 + 1}}{\frac{p_2}{p_1} + \frac{\gamma_1 - 1}{\gamma_1 + 1}} \right)^{\frac{1}{2}}, \quad (9.39)$$

with  $a_1$  the speed of sound in region 1.

### Expansion fan

Next we consider the expansion fan separating states 3 and 4. We apply Eq. (9.34),

with  $u_4 = 0$ , this gives

$$u_3 = \frac{2a_4}{\gamma_4 - 1} \left[ 1 - \left( \frac{p_3}{p_4} \right)^{\frac{\gamma_4 - 1}{2\gamma_4}} \right]. \quad (9.40)$$

### Contact discontinuity

As discussed before, pressure and velocity are continuous across a contact discontinuity, so that  $p_2 = p_3$  and  $u_2 = u_3$ . With  $p_3 = p_2$  (9.40) becomes

$$u_3 = u_4 + \frac{2a_4}{\gamma_4 - 1} \left[ 1 - \left( \frac{p_2}{p_4} \right)^{\frac{\gamma_4 - 1}{2\gamma_4}} \right]. \quad (9.41)$$

And with  $u_2 = u_3$  (9.39) and (9.41) can be equated as

$$\frac{a_1}{\gamma_1} \left( \frac{p_1}{p_2} - 1 \right) \left( \frac{\frac{2\gamma_1}{\gamma_1 + 1}}{\frac{p_2}{p_1} + \frac{\gamma_1 - 1}{\gamma_1 + 1}} \right)^{\frac{1}{2}} = \frac{2a_4}{\gamma_4 - 1} \left[ 1 + \frac{\gamma - 1}{2} \frac{u_4}{c_4} - \frac{p_2}{p_4} \frac{\gamma_4 - 1}{2\gamma_4} \right], \quad (9.42)$$

which can be rearranged to give

$$\frac{p_4}{p_1} = \frac{p_2}{p_1} \left\{ 1 - \frac{(\gamma_4 - 1)(a_1/a_4)(p_2/p_1 - 1)}{\sqrt{2\gamma_1[2\gamma_1 + (\gamma_1 + 1)(p_2/p_1 - 1)]}} \right\}^{-2\gamma_4/(\gamma_4 - 1)}. \quad (9.43)$$

From this equation  $p_2/p_1$  has to be determined numerically, after which the solution can be constructed. Equation (9.43) gives the incident shock strength  $p_2/p_1$  as an implicit function of the diaphragm pressure ratio  $p_4/p_1$ . Although it is difficult to see from Eq. (9.43), this relation shows that for a given diaphragm pressure ratio  $p_4/p_1$ , the shock strength  $p_2/p_1$  will be made stronger as  $a_1/a_4$  is made smaller.

### Solution process

The analysis of the flow of a perfect gas in a shock tube is now straightforward. Along with the initial conditions of the gases,  $p_4/p_1$  uniquely defines the strengths of the shock and expansion waves. For a given diaphragm ratio  $p_4/p_1$ :

1. Calculate  $p_2/p_1$  from Eq. (9.43). This defines the strength of the shock wave.
2. Calculate all other shock properties from Eqs. (9.23), (9.16) and (9.18).
3. Calculate  $p_3/p_4 = (p_3/p_1)/(p_4/p_1) = (p_2/p_1)/(p_4/p_1)$ . This defines the strength of the expansion wave.
4. All other thermodynamic properties immediately behind the expansion wave can be found from the isentropic relations

$$\frac{p_3}{p_4} = \left( \frac{\rho_3}{\rho_4} \right)^\gamma = \left( \frac{T_3}{T_4} \right)^{\gamma/(\gamma-1)}. \quad (9.44)$$

5. The local properties inside the expansion wave can be found from Eq. (9.34) for  $p/p_4$ , and the isentropic relations

$$\frac{p}{p_4} = \left( \frac{\rho}{\rho_4} \right)^\gamma = \left( \frac{T}{T_4} \right)^{\gamma/(\gamma-1)}. \quad (9.45)$$

## 9.2 Numerical results

In the previous section the analytical solution of Riemann problems was discussed. In this section we will compute the solution of several Riemann problems with our numerical method and compare the results with results for the Osher method. Results shown for the Osher method in this chapter were kindly provided by professor Wesseling. For a description of the Osher scheme we refer to [51]

Numerical schemes must converge to a genuine weak solution. This means that numerical shocks must move at the correct speed. Furthermore, the entropy condition must be satisfied. This means that the entropy of fluid particles is not allowed to decrease, which rules out expansion shocks. These conditions are easily violated by numerical schemes. From the numerical solutions it can be seen that our method which uses a staggered grid accurately computes shocks, contact discontinuities and expansion waves, and computes the right shock speed.

Since in some test cases  $w_\infty = 0$  we cannot use the previous nondimensionalisation. Instead we use

$$\rho_r = \rho_A \quad p_r = p_A \quad h_r = h_A \quad w_r = 1. \quad (9.46)$$

When not stated explicitly the domain is  $[0, 1]$ , with at  $t = 0$  the separation between the left and right state at  $x_0 = 0.5$ . For the time discretisation we have chosen the parameters  $\theta = \mu = 1$ . This results in the implicit Euler method so that we do not encounter a stability restriction on the time step. However, since we will compute non-stationary flows, we have to choose the time step in accordance with the time scale of the physical phenomena to be computed. Furthermore, since our aim is comparison of our method with a standard compressible flow method, for which we have chosen the explicit Osher method, we will choose our time step such that the CFL number

$$\nu = \frac{(|u| + a)\delta t}{\delta x} = \frac{(|u| + a)}{\lambda} < 1, \quad (9.47)$$

with  $\lambda = \delta x / \delta t$ . We used 100 grid cells, so that  $\delta x = 0.01$ .

### 9.2.1 Sod's shock tube problem

When  $u_1 = u_4 = 0$  the Riemann problem is called the shock tube problem. It can be realised experimentally by the sudden removal of a diaphragm in a long one-dimensional tube separating two initial gas states at rest at different pressures and densities. Sod's shock tube problem [68] is a Riemann problem with the following left and right states:

$$u_4 = 0, \quad p_4 = 1.0, \quad \rho_4 = 1.0, \quad u_1 = 0, \quad p_1 = 0.1, \quad \rho_1 = 0.125. \quad (9.48)$$

The exact solution can be determined in the way described in the previous section and is shown as a continuous line in Figure 9.3.

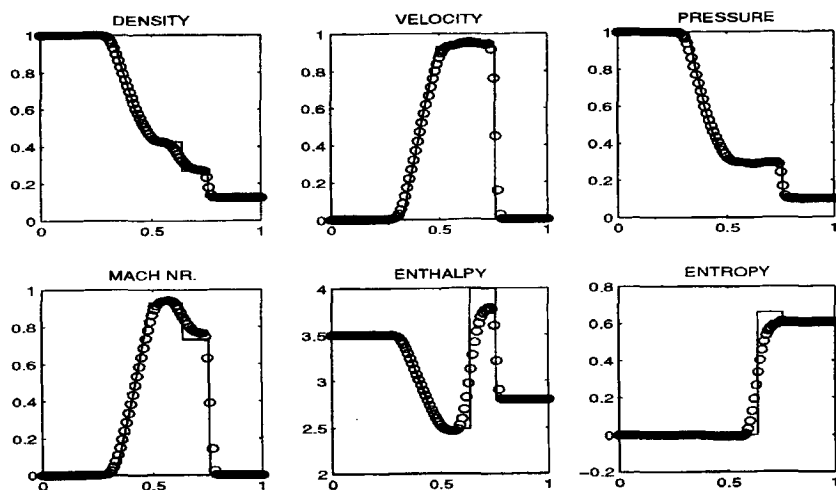


Figure 9.3: Sod's shock tube problem; comparison of staggered first-order upwind scheme with exact solution at  $t = 0.15$

As can be seen from the Mach number plot the flow remains subsonic. The maximum wave speed in the flow is  $\bar{u}_m = \max(|u| + a) = 2.2$ . Consequently, with  $\delta x = 0.01$  the time step restriction for the explicit Osher method is for this test problem  $\delta t < 0.0045$ . In the computations of Sod's shock tube problem we use  $\delta t = 0.004$ . Some publications showing numerical results for this test case are Sod [68], Harten et al. [24, 25], Hirsch [26], Arora and Roe [3], and Toro [70].

For the space discretisation of the convection terms in the momentum and energy equation the first-order upwind scheme was used. Because the flow is subsonic no upwind bias for the density is applied. The difficulties in computing Sod's shock tube problem are to compute the expansion wave and the discontinuities accurately and to compute the right shock speed. Our solution at  $t = 0.15$  is compared with the exact solution at this time in Figure 9.3. There it can be seen that our scheme converges to the correct weak solution and satisfies the entropy condition, which states that the entropy of fluid particles does not decrease. Of course, over the contact discontinuity the entropy decreases, but since fluid particles do not cross the contact discontinuity, the entropy of the particles does not decrease. Due to the use of first order upwind spatial discretisation, the contact discontinuity is smeared as can be seen from the enthalpy and entropy plots, and to a lesser extent from the density plot. But the shock resolution is crisp. The numerical shock is seen to move at the correct speed, and the approximation of the expansion wave is smooth.

Solution of Sod's shock tube problem with Osher's approximate Riemann solver [50, 51] is shown in Figure 9.4. Comparison of Fig. 9.3 with Fig. 9.4 shows our method to be about as accurate as the Osher scheme.

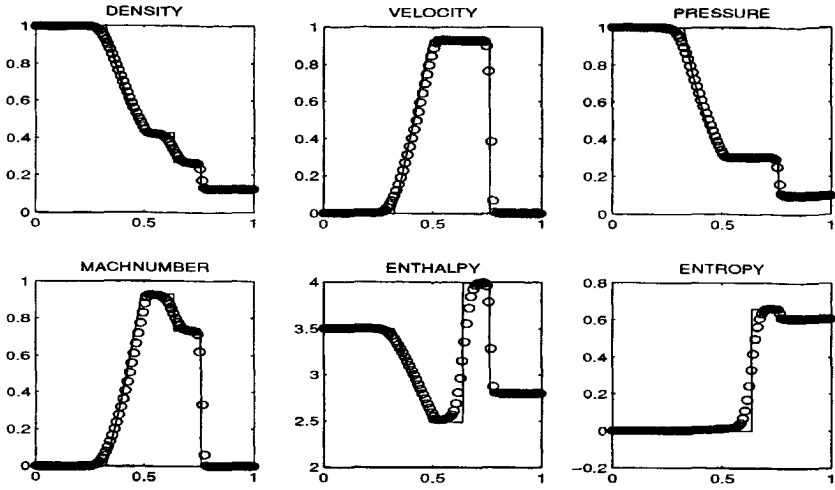


Figure 9.4: Sod's shock tube problem; comparison of Osher scheme with exact solution at  $t = 0.15$

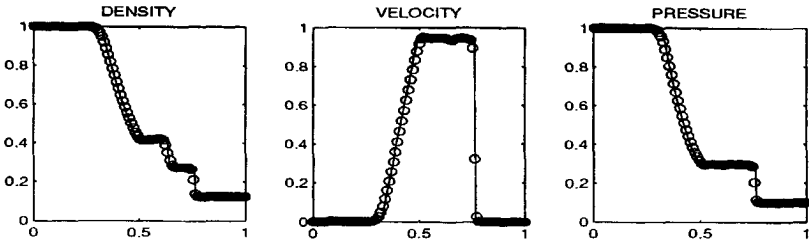


Figure 9.5: Sod's shock tube problem; comparison of staggered MUSCL scheme with exact solution at  $t = 0.15$

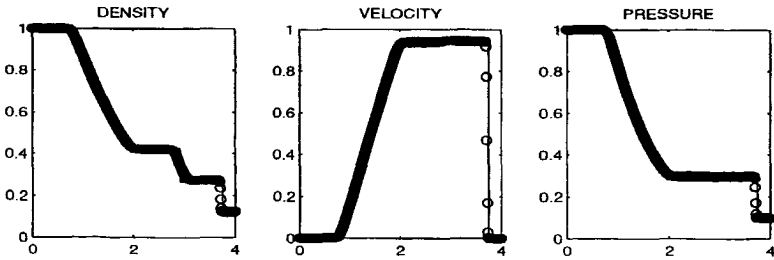


Figure 9.6: Sod's shock tube problem; comparison of numerical solution with exact solution at  $t = 1$ .

The accuracy of the present method can be improved by using a higher order upwind biased scheme. For this we follow the MUSCL approach, see Van Leer [75], as explained in Section 4.6. In Figure 9.5 the solution obtained with the MUSCL scheme is compared to the exact solution. The shock and especially the contact discontinuity have become more crisp. A tiny wiggle is formed in front of the contact discontinuity, which might be due to the non-conservative discretisation of the energy equation. The quality of the results in Figure (9.5) is about the same as for standard colocated approximate Riemann solvers enhanced with the MUSCL approach (results not shown).

In order to check the computed shock speed a computation over a longer time, i.e.  $t = 1$ , has been carried out. In this computation the domain was larger:  $[0, 4]$ , with the separation between the left and right state at  $x_0 = 2$ . Also in this computation  $\delta x = 0.01$ , and  $\delta x = 0.004$ . The result is shown in Fig. 9.6. There it can be seen that even after computation over a longer time the computed shock position is still right. Although our method is not fully conservative, due to use of the non-conservation form of the energy equation, this does not result in a wrong shock speed. Apparently, use of the conservation form of the continuity and momentum equations is good enough.

### 9.2.2 Test case of Lax

Another frequently used test problem is the test case of Lax [41]. The initial state is specified by

$$u_4 = 0.698, \quad p_4 = 3.528, \quad \rho_4 = 0.445, \quad u_1 = 0, \quad p_1 = 0.571, \quad \rho_1 = 0.5. \quad (9.49)$$

The exact solution can be determined in the way described in Section 9.1.5 and is shown as a continuous line in Figure 9.7. As can be seen from the Mach number-plot, the flow remains subsonic. The contact discontinuity and the shock are stronger than in Sod's shock tube problem, shown in Fig 9.3. The maximum wave speed in the flow is  $\bar{\mu}_m = \max(|u| + a) = 4.7$ . Consequently, with  $\delta x = 0.01$  the time step restriction for the explicit Osher method is for this test problem  $\delta t < 0.0021$ . In the computations of the test case of Lax we use  $\delta t = 0.002$ . Some publications showing numerical results for this test case are Harten et al. [24, 25], Arora and Roe [3], and Toro [70].

For the space discretisation of the convection terms in the momentum and energy equation the first-order upwind scheme was used. Because the flow is subsonic no upwind bias for the density is applied. The solution at  $t = 0.1$  obtained with the present method is compared with the exact solution in Figure 9.8. It is seen that our scheme converges to the correct weak solution.

Solution of the Lax test case with Osher's approximate Riemann solver [50, 51] is shown in Figure 9.9. Comparison of Fig. 9.8 with Fig. 9.9, shows our method to about be as accurate as the Osher scheme. Both the staggered scheme and the Osher scheme smear the contact discontinuity. For the staggered scheme there is an overshoot of the variables right before the shock, whereas the Osher scheme does not compute entirely the right form of the expansion wave for the velocity and pressure.



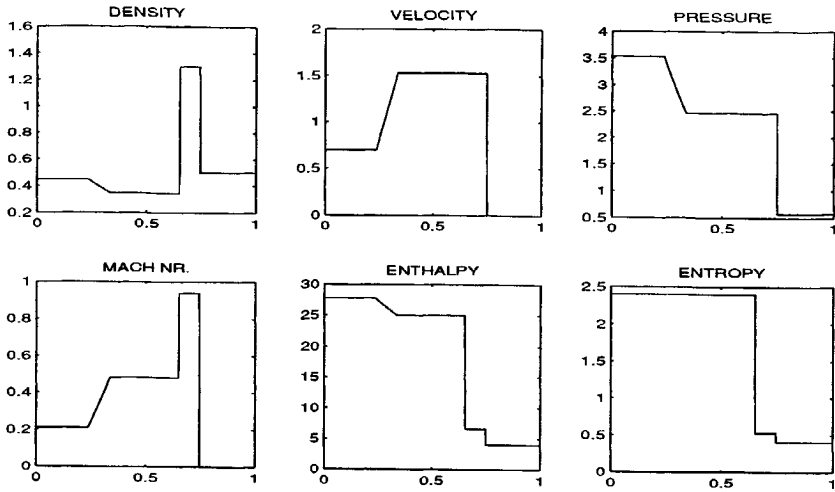


Figure 9.7: Test case of Lax; exact solution at  $t = 0.1$

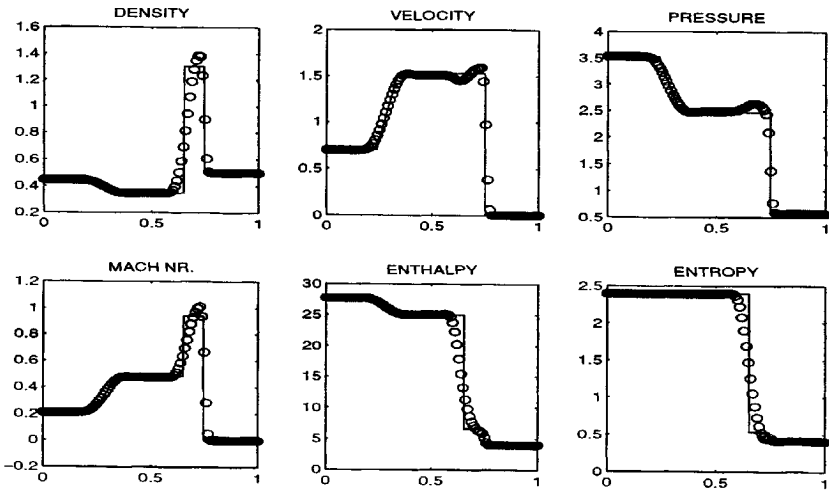


Figure 9.8: Test case of Lax; comparison of staggered first-order upwind scheme with exact solution at  $t = 0.1$

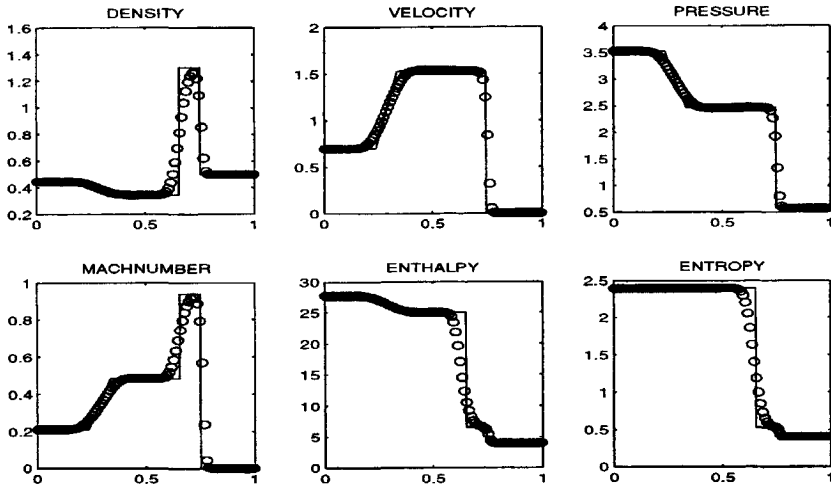


Figure 9.9: Test case of Lax; comparison of Osher scheme with exact solution at  $t = 0.1$

### 9.2.3 Supersonic flow test case

In the previous two test cases the flow remained subsonic. Supersonic flow may bring additional difficulties. Therefore, we will also consider the Mach 3 test case of Arora and Roe [3]. The initial state is specified by

$$u_4 = 0.92, p_4 = 10.333, \rho_4 = 3.857, \quad u_1 = 3.55, p_1 = 1, \rho_1 = 1. \quad (9.50)$$

The exact solution can be determined in the way described in the Section 9.1.5 and is shown as a continuous line in Figure 9.10. The flow is characterised by a strong expansion fan. The maximum Mach number is equal to 3. The maximum wave speed in the flow is  $\bar{\mu}_m = \max(|u| + a) = 5.0$ . Consequently, with  $\delta x = 0.01$  the time step restriction for the explicit Osher method is for this test problem  $\delta t < 0.002$ . In the computations of the test case of Lax we use  $\delta t = 0.002$ , which did not cause problems.

For the space discretisation of the convection terms in the momentum and energy equation the first order upwind scheme was used. For this test problem the right solution was obtained even without density biased upwinding. The solution obtained with the present method at  $t = 0.088$  is compared with the exact solution in Figure 9.11. There it can be seen that our scheme converges to the correct weak solution.

Solution of the Mach 3 test case with Osher's approximate Riemann solver [50, 51] is shown in Figure 9.12. There it can be seen that the Osher scheme suffers from a 'sonic glitch'. That is, near the sonic point the expansion fan shows a discontinuity. But the entropy condition is not violated, as can be seen from the entropy plot, and is in accordance with the theoretical results of [51]. As can be seen from Fig. 9.11 our scheme does not suffer from this. The contact discontinuity is smeared more with our

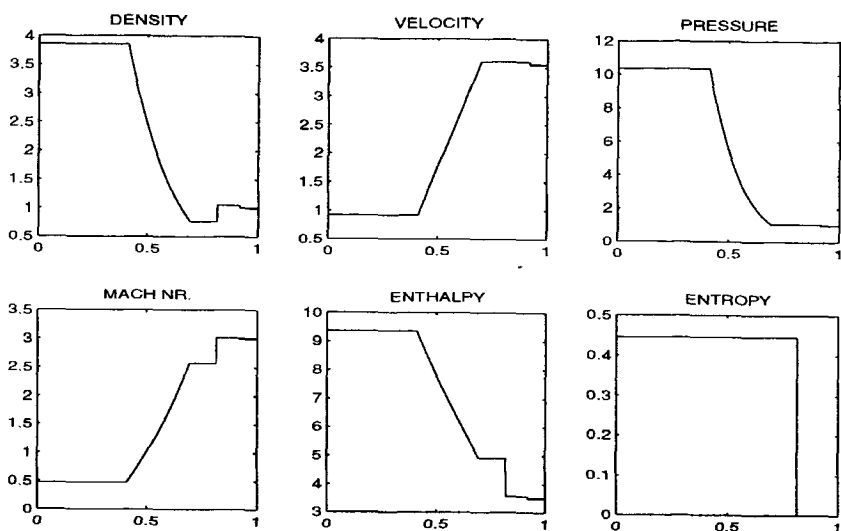


Figure 9.10: Mach 3 test case; exact solution at  $t = 0.088$

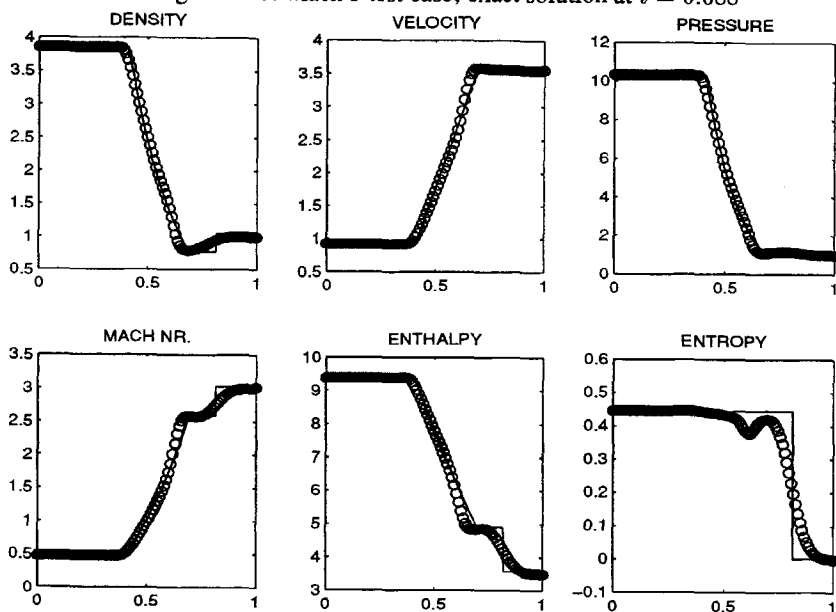


Figure 9.11: Mach 3 test case; comparison of staggered first-order upwind scheme with exact solution at  $t = 0.088$

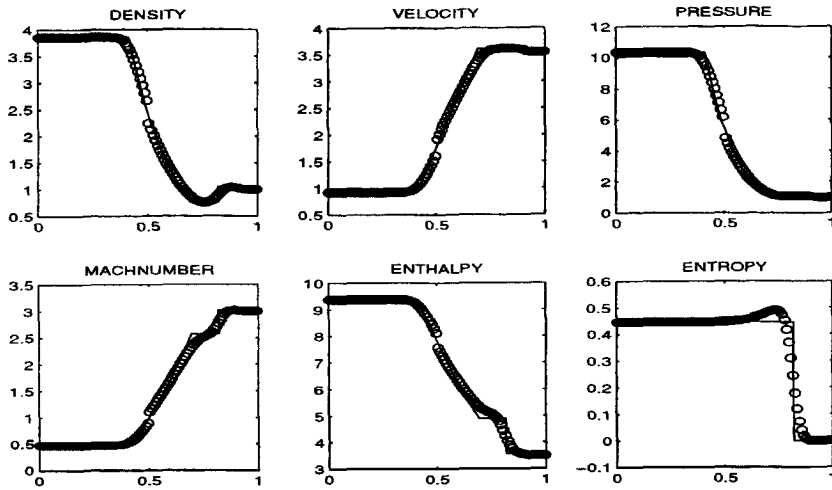


Figure 9.12: Mach 3 test case; comparison of Osher scheme with exact solution at  $t = 0.088$

method.

The accuracy of the numerical solution obtained with the present method is improved by use of the higher order MUSCL scheme. In Figure 9.13 the solution obtained with the MUSCL scheme is compared to the exact solution. The (weak) shock and especially the contact discontinuity have become more crisp. Again we conclude that the staggered scheme seems to be as accurate as the nonstaggered Osher scheme. Near the sonic point our scheme is even better.

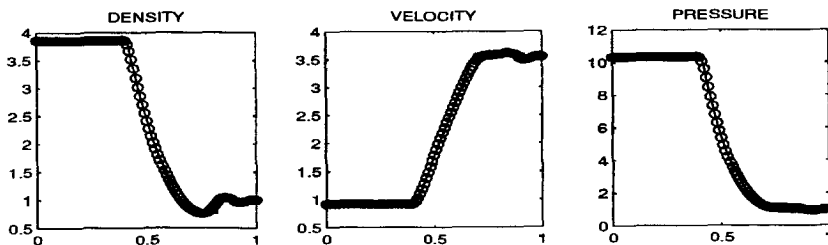


Figure 9.13: Mach 3 test case; comparison of staggered MUSCL upwind scheme with exact solution at  $t = 0.088s$ .

### 9.2.4 Test case with nonstationary contact discontinuity

Finally, a test problem with a non-stationary contact discontinuity is considered. The initial conditions are:

$$u_4 = 0.6, p_4 = 1, \rho_4 = 1, \quad u_1 = 0.6, p_1 = 1, \rho_1 = 0.7. \quad (9.51)$$

The exact solution is a contact discontinuity which propagates with speed  $u = 0.6$  to the right. In a contact discontinuity the density jumps, while the velocity and pressure remain constant. The exact solution at  $t = 1$  is shown as a continuous line in Fig. 9.14. The maximum wave speed in the flow is  $\bar{\mu}_m = \max(|u| + a) = 1.2$ . Consequently, with  $\delta x = 0.01$  the time step restriction for the explicit Osher method is for this test problem  $\delta t < 0.0083$ . We use  $\delta t = 0.008$ .

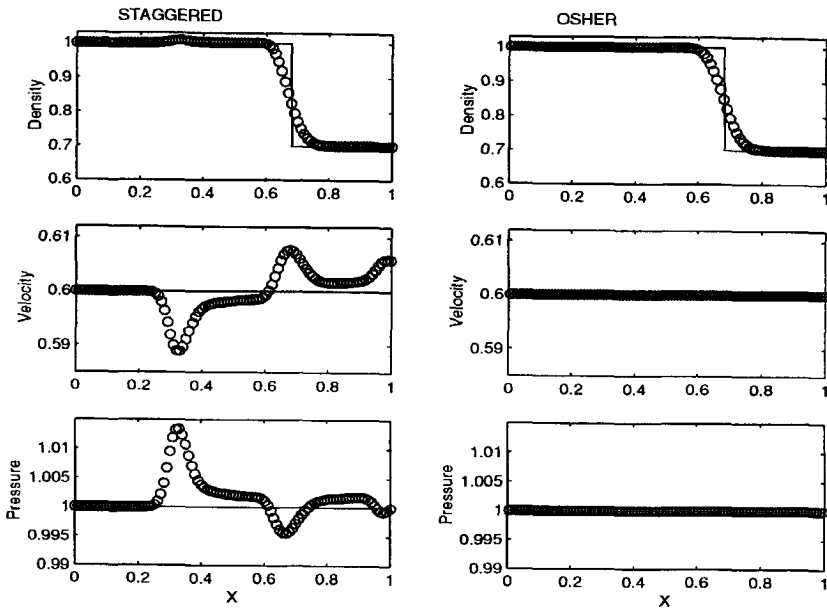


Figure 9.14: Contact discontinuity; comparison of staggered first order upwind and Osher method with the exact solution at  $t = 1$

In Fig. 9.14 the solution of the non-stationary contact discontinuity obtained with the present staggered method is compared with the exact solution, and the solution obtained with the Osher method. There it can be seen that with the present staggered method the contact discontinuity is not preserved exactly, since there are spurious wiggles in the solution of the pressure and velocity. The amplitude of the wiggles is of the order of 1%. The Osher method does not produce spurious wiggles. We can think of four possible causes for the spurious wiggles: 1) the interpolation/extrapolation necessary for the

staggered method, 2) implementation of boundary conditions, 3) the non-conservative form of the energy equation, 4) the formulation of the pressure correction equation. To begin with, on our grid variables occupy different positions in the grid, so that for solution of the equations they have to be interpolated, which might be the cause of the wiggles. This is not the case for the Osher method, which uses a collocated grid. Secondly, we use reflecting boundary conditions, whereas in the Osher method characteristic boundary conditions are used. Waves reflecting at the boundaries might also be the cause of the wiggles. Then, as stated before, in our method a non-conservative formulation of the energy equation is used; we have a term  $hu_x^\alpha$ . Especially when  $h$  jumps and  $u$  does not this might lead to problems. Finally, the formulation of the pressure correction equation might not be suited very well for strong contact discontinuities.

Only the last hypothesis was investigated. As discussed in Section 6.3 the original pressure correction equation can be improved for contact discontinuities by replacing  $\rho h$  by  $p$  at strategic points. This resulted in an alternative pressure correction equation. In Figure 9.15 results of this improved pressure correction is compared with those of the original method. The amplitude of the wiggles is now 0.5%. Wiggles within this limit might be acceptable for applications. Unfortunately, we did not have time to check the other possible causes for the remaining wiggles.

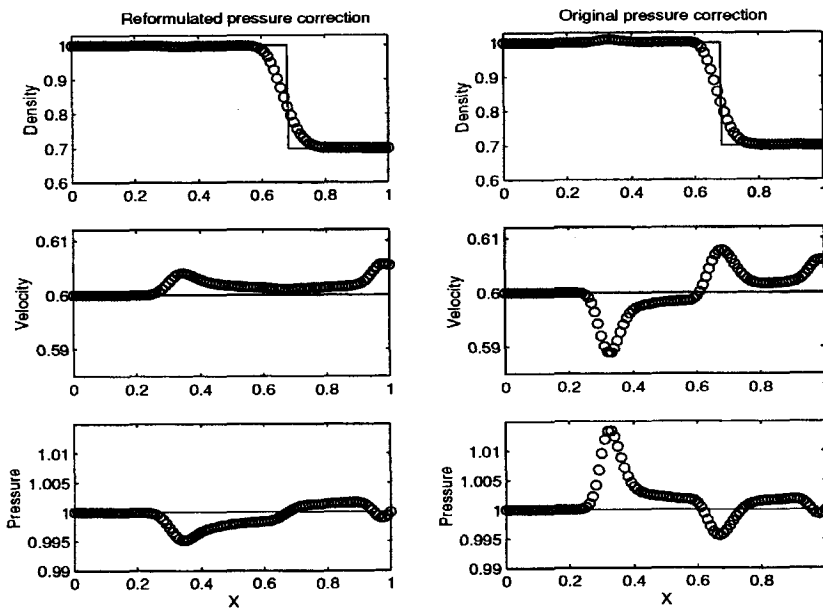


Figure 9.15: Contact discontinuity; solution at  $t = 1$

In Fig. 9.16 we zoom in to the density just before the jump. As can be seen the alternative pressure correction equation certainly improves the quality of the numerical

solution. Furthermore, also the Osher method is not exact and suffers from smearing.

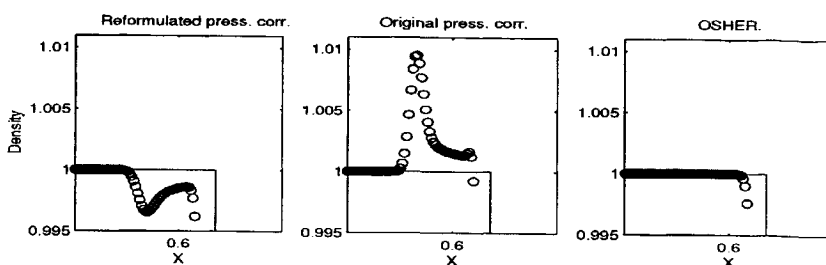


Figure 9.16: Contact discontinuity; density jump at  $t = 1$

### 9.2.5 Final remarks

Although, as for most methods in current use, a theoretical basis is lacking, on the basis of the experiments described above we have every reason to believe that our scheme approximates genuine weak solutions of the Euler equations that satisfy the entropy condition. Furthermore, our method seems less computing-intensive than collocated methods using approximate Riemann solvers (such as schemes of Osher, Roe and van Leer) or artificial viscosity (Jameson). This is because we use only central and/or upwind differences, which is much cheaper than approximate solutions of Riemann problems to determine numerical fluxes at finite volume boundaries, or using solution dependent second and fourth order artificial dissipation terms.





# 10

## Applications

After validation of accuracy and efficiency of our method for well known one-dimensional shock tube problems, and two-dimensional channel and nozzle flows, in this chapter two more challenging applications are discussed. These applications are: flow inside an industrial blower configuration and flow around an airfoil.

### 10.1 Industrial application

In this section results of the computation of flow in an industrial blower configuration of AKZO Nobel will be shown. This industrial blower is used in the fiber production for transportation and strengthening of the fibers. The blower configuration is shown in Figure 10.1. In this blower air from two high pressure vessels is blown into the fiber channel under an angle of  $20^\circ$ , resulting in a shear stress on the filaments. Due to this shear stress the molecules in the fibers align so that they become stronger, also the fibers are transported. Due to the high pressure in the vessel the Mach number of the air leaving the vessel is  $M = 1$ , while the Mach number at the fiber inlet and outlet is approximately equal to 0.1 and 0.3, respectively. This combination of both medium high and low Mach numbers provides a good test application for our method. We will compare our results with experimental measurements performed by Persoon [54].

The main question concerning flow in the blower is how a widening of the fiber channel influences the general flow pattern. Therefore, we have performed computations for both a straight channel and a channel with a widening. In order to test the numerical method we will compare for the straight channel results obtained for viscous and inviscid flow. In the following section conditions concerning the flow in the blower will be discussed. That is assumptions of flow properties, boundary conditions and scaling parameters. Thereafter, in the next two sections inviscid and viscous flow results of the computations will be shown.

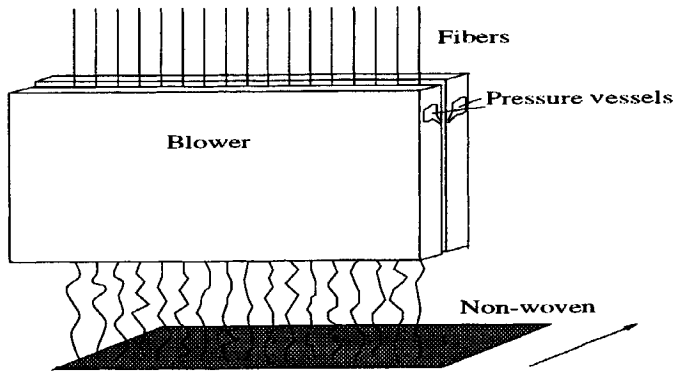


Figure 10.1: The blower configuration

### 10.1.1 Flow type and domain

In this section, first assumptions concerning the flow pattern are made in order to simplify the computations. Thereafter, the computational domain and grid are shown. Finally, appropriate boundary conditions and scaling parameters are derived.

#### Assumptions concerning the flow pattern

In order to simplify the problem we will make the following assumptions concerning the flow:

- a) The flow is two-dimensional
- b) The flow is laminar
- c) The flow is stationary
- d) The flow inside the slit is symmetric
- e) The fiber has no significant influence on the flow pattern
- f) The air is a perfect gas

In reality not all of these assumptions are completely satisfied. For example, the fiber in the middle of the channel oscillates, so that assumption c) and d) are false. Nevertheless, since our main goal is to gain insight into the general flow pattern, we will use the above simplifying assumptions.

#### Geometry and mesh

As discussed above, we assume the flow to be two-dimensional and symmetric, so that the computational geometry can consist of half of the cross section of the blower, as shown in Figure 10.2 a). Inside this domain a multiblock mesh is generated. As shown in Figure 10.2 b) we use two blocks. One block of  $4 \times 175$  mesh points from the fiber inlet to the fiber outlet, and one block of  $8 \times 183$  mesh points from the air inlet to the air outlet. In Figure 10.3 a close-up of the mesh in the area where the air inlet meets

the fiber channel is shown. It was hard to generate a smooth mesh in this area. Unfortunately, we only succeeded to create one acceptable mesh without large jumps in grid size, so that we were unable to perform test on grid dependence of the solution. In the computations for the blower with a widening, the same domain was used, except at a certain point in the fiber channel, the channel becomes wider.

The flow pattern in the domain is as follows. Air from a high pressure vessel is blown into the slit through the air inlet,  $B_1$ . This air entrains air from the fiber inlet,  $B_2$ . At the fiber outlet,  $B_{out}$ , the air leaves the channel. The angle between the air inlet and the main channel is  $20^\circ$ . The pressure in the vessel is  $p_0^* = 7 \text{ bar} = 7 \cdot 10^5 \text{ Pa}$ . From this information, combined with measurements and one-dimensional gas dynamic analysis, boundary conditions are derived. This is the subject of the next section.

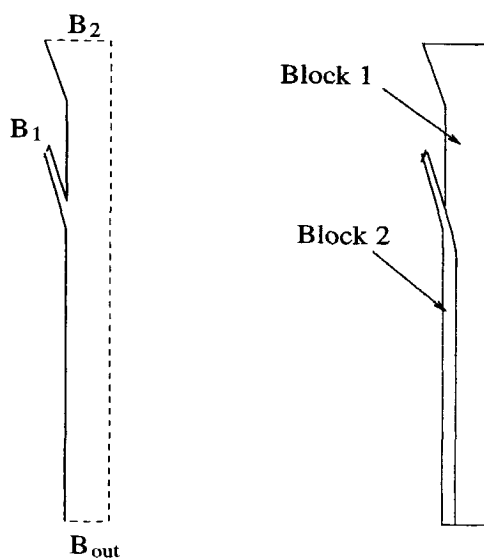


Figure 10.2: a) Computational domain: half of the cross section of the blower, b) Multi-block mesh with two blocks

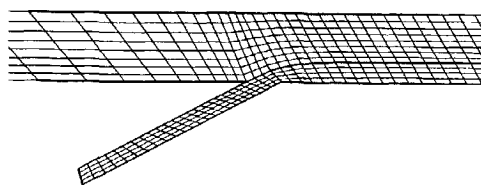


Figure 10.3: Close-up of mesh at air inlet

### 10.1.2 Boundary conditions

For the quantities necessary for the determination of the scaling parameters and boundary conditions, we use a combination of one-dimensional gas dynamic analysis and measurements performed by Persoon [54]. First, we will derive the mass flux at the inlet and the appropriate stagnation pressure. Then, the non-dimensional boundary conditions and scaling parameters will be discussed.

#### Mass flux at air inlet

Due to the high pressure in the vessel, the flow at the air inlet is transonic,  $M_1 = 1$ . With this information the mass flux at the inlet can be approximately derived from the reservoir temperature and pressure in the vessel with one-dimensional inviscid gas dynamic theory. In doing so we assume that the gas flows isentropically from a hypothetical infinite reservoir into the air inlet. Since this theory does not take into account losses due to viscous stresses upstream from the air inlet, the computed mass flux will be larger than the inlet mass flux as measured by Persoon. Having shown this, we will derive a lower stagnation pressure which will give us in one-dimensional gas dynamic theory the same mass flux as found by Persoon. With this new stagnation pressure we will perform the dimensionless computations, as explained later.

#### Mass flux according to inviscid gas dynamic theory unequal to flux measured

Dimensional quantities are denoted by an asterisk. From the reservoir pressure  $p_0^* = 7 \cdot 10^7 \text{ Pa}$ , and the reservoir temperature  $T_0^* = 285^\circ \text{ K}$ , measured by Persoon, and  $R^* = 287 \text{ J/kg K}$ , we can compute  $\rho_0^*$  with the equation of state:

$$\rho_0^* = \frac{p_0}{RT_0} = \frac{7 \cdot 10^5}{287 \cdot 285} = 8.56 \text{ kg/m}^3. \quad (10.1)$$

The state variables at the air inlet follow from the one-dimensional gas dynamic relations:

$$\rho_1^* = \left(1 + \frac{\gamma - 1}{2} M_1^2\right)^{-\frac{1}{\gamma - 1}} \rho_0^* = \frac{\rho_0^*}{(1.2)^{2.5}} = 5.4 \text{ kg/m}^3, \quad (10.2)$$

$$p_1^* = \left(1 + \frac{\gamma - 1}{2} M_1^2\right)^{-\frac{\gamma}{\gamma - 1}} p_0^* = \frac{p_0^*}{(1.2)^{3.5}} = 3.7 \cdot 10^5 \text{ Pa}, \quad (10.3)$$

$$T_1^* = \left(1 + \frac{\gamma - 1}{2} M_1^2\right)^{-1} T_0^* = \frac{T_0^*}{1.2} = 237.5^\circ \text{ K}. \quad (10.4)$$

From  $M_1 = \frac{u_1}{a_1} = 1$ , we find

$$u_1^* = a_1^* = \sqrt{\gamma R^* T_1^*} = \sqrt{1.4 \cdot 287 \cdot 237.5} = 309 \text{ m/s}. \quad (10.5)$$

Consequently,

$$\rho_1^* u_1^* = 1669 \text{ kg/m}^2 \text{ s}. \quad (10.6)$$

With a surface of the air inlet equal to  $A_1^* = 6.25 \cdot 10^{-5} \text{ m}^2$ , the mass flux at the air inlet is

$$\rho_1^* u_1^* A_1^* = 1669 \cdot 6.25 \cdot 10^{-5} \text{ kg/s} = 0.6 \text{ kg/s} \quad (10.7)$$

$$= \frac{2160}{1.2} \text{ Nm}^3/\text{h} = 1800 \text{ Nm}^3/\text{h}, \quad (10.8)$$

where  $\text{Nm}^3$  is a normal cubic, is equal to  $1 \text{ m}^3$  of air of density  $1.2 \text{ kg/m}^3$ , hence  $1 \text{ Nm}^3 = 1.2 \text{ kg}$ . Persoon measured a mass flux of only  $250 \text{ Nm}^3/\text{h}$  at the air inlet. The difference between our  $1800 \text{ Nm}^3/\text{h}$  and Persoon's  $250 \text{ Nm}^3/\text{h}$  is caused by the viscous losses, neglected in our mass flux computation. In order to do realistic computations we need to prescribe the same mass flux as Persoon. Therefore, we will use in our computations a stagnation pressure in the vessel which is consistent with the measured flux. This new stagnation pressure is derived as follows.

#### Adaption of stagnation pressure to obtain realistic mass flux

We will assume that friction does not influence the temperature significantly, so that we can use the temperatures as computed with the inviscid flow equations in the previous paragraph. This means that  $u_1^* = a_1^* = 309$ , see (10.5), does not change. For the mass flux we have

$$D_1^* = \rho_1^* u_1^* A_1^* = 250 \text{ Nm}^3/\text{h} = 0.083 \text{ kg/s}. \quad (10.9)$$

From the inviscid flow relation for the density (10.2) and from the equation of state (10.1) we find

$$\rho_1^* = (1.2)^{-2.5} \frac{p_0}{RT_0^*}. \quad (10.10)$$

The expression of  $p_0$  can now be found from

$$\rho_1^* u_1^* = \left(1 + \frac{\gamma - 1}{2} M_1^2\right)^{-\frac{1}{\gamma-1}} \frac{p_0^*}{R^* T_0^*} u_1, \quad (10.11)$$

so

$$p_0^* = \frac{D_1^* R^* T_0^*}{A_1^* u_1} (1.2)^{2.5} = 5.5 \cdot 10^5 \text{ Pa}. \quad (10.12)$$

This is 79% of the real stagnation pressure of  $7 \cdot 10^5 \text{ Pa}$ , so that the pressure loss from friction between the vessel and the air inlet is 21%. From (10.3) we find the pressure at the air inlet,

$$p_1^* = 2.9 \cdot 10^5 \text{ Pa}, \quad (10.13)$$

which according to one-dimensional inviscid theory agrees with the inlet mass flux measured.

### Dimensionless boundary conditions at air inlet

The flow in the blower is determined by the flow of air from the pressure vessel. Hence we will choose the parameters at the air inlet and their associated stagnation conditions in the vessel as scaling parameters. With  $M_1 = 1$ , the dimensionless boundary conditions at the air inlet, see (4.27), are:

$$\begin{aligned}(\rho u)_1^n &= \left(1 + \frac{\gamma-1}{2} M_1^2\right)^{\frac{-1}{\gamma-1}} \cos \alpha_1 = 0.634, \\(\rho u)_1^t &= \left(1 + \frac{\gamma-1}{2} M_1^2\right)^{\frac{-1}{\gamma-1}} \sin \alpha_1 = 0, \\h_1 &= \left(1 + \frac{\gamma-1}{2} M_1^2\right)^{-1} = 0.83,\end{aligned}\tag{10.14}$$

with  $(\rho u)_1^n$  the mass flux component normal to the inlet, and  $(\rho u)_1^t$  the mass flux component tangential to the inlet.

### Dimensionless boundary conditions at fiber inlet

From Persoon's measurements [54] we know that the flow at the fiber inlet is subsonic. He also found that the temperature in the entire flow field only varies approximately 5%. Therefore, we will assume the temperature at the fiber inlet to be equal to the temperature at the air inlet. Furthermore, following measurements of Persoon we will assume the mass flux at the fiber inlet to be 10% of the mass flux at the air inlet. This determines the boundary conditions at the fiber inlet:

$$(\rho u)_1^n = 0.0634,\tag{10.15}$$

$$(\rho u)_1^t = 0,\tag{10.16}$$

$$h_1 = 0.83.\tag{10.17}$$

Of course, it would be better not to prescribe the mass flux entrained by the flow and let the method compute the appropriate amount. Unfortunately, this is mathematically impossible since the mass flux or velocity needs to be prescribed at an inlet. Persoon also measured the outflow at the fiber outlet to be subsonic. Consequently, the dimensionless outlet pressure is prescribed as:

$$p_{out} = 0.\tag{10.18}$$

### Boundary conditions at walls and symmetry plane

The boundary conditions at the walls and symmetry plane are different for the Euler and Navier-Stokes equations. At the symmetry plane we will assume free slip boundary conditions, for Euler equations this implies only:

$$u_n = 0,\tag{10.19}$$

while for viscous flow also

$$\sigma_{nt} = 0.\tag{10.20}$$

For the inviscid flow computations we prescribe freeslip at the walls too, so

$$u_n = 0, \quad (10.21)$$

while for the viscous flow computations for all walls except the walls of the air inlet no-slip boundary conditions are prescribed at the wall, hence

$$u_n = u_t = 0. \quad (10.22)$$

In the air inlet for viscous flow computations free-slip was prescribed too, since with no-slip the computations would not converge to a stationary solution. Apparently the flow had problems to push through the air inlet channel with no-slip boundaries, but the exact reason for this is unknown.

### Scaling parameters

We also need to determine the nondimensional pressure ratio  $p_w$  which appears in the non-dimensional equation of state (6.27):

$$\frac{p_{out}^* - p_0^*}{p_1^* - p_0^*} = \frac{1 \cdot 10^5 - 5.5 \cdot 10^5}{2.9 \cdot 10^5 - 5.5 \cdot 10^5} = 1.73, \quad (10.23)$$

where we assumed the dimensional outlet pressure  $p_{out}^*$  to be equal to atmospheric pressure, and where we used the stagnation and inlet pressure  $p_0^*$  and  $p_1^*$  as derived above. Note that this ratio is very sensitive to changes in the dimensional pressure variables. For the Navier-Stokes equations also the Reynolds number

$$Re = \frac{\rho_0^* w_1^* L^*}{\mu^*} \quad (10.24)$$

needs to be determined. For  $L^*$  we take 1m, since in our computations we work with the real dimensions of the system. The dynamic viscosity  $\mu^*$  is for air  $1.789 \cdot 10^{-5} \text{ kg/m s}$ . The characteristic speed is given above  $w_1^* = \sqrt{(u_1^n)^2 + (u_1^t)^2} = 309 \text{ m/s}$ . The stagnation density follows from the stagnation temperature and pressure:  $\rho_0^* = p_0^*/(R^*T_0^*) = 6.7 \text{ kg/m}^3$ . With this our Reynolds number becomes

$$Re = \frac{\rho_0^* w_1^* L^*}{\mu^*} = \frac{p_0^*/(R^*T_0^*) w_1^* L^*}{\mu^*} = 1.2 \cdot 10^8. \quad (10.25)$$

### 10.1.3 Computational results for straight fiber channel

In this section results of computations of both viscous and inviscid flow in the blower with a straight fiber channel will be shown. This is done to see whether our method computes satisfactorily solutions for both types of flows. The maximum Mach number for viscous flow will be lower than for the inviscid case, due to losses caused by viscous stress on the walls. The outlet Mach number for viscous flows will turn out to be

approximately equal to the Mach number measured by Persoon, whereas the inviscid outlet Mach number is approximately two times too large.

### Computational results for inviscid flow

We first assume the flow in the blower to be inviscid and use the Euler equations to compute the flow for a blower with a straight fiber channel. The results will be compared with the results for viscous flow in the same domain. In the computations we used the original compressible pressure correction formulation and first order upwind discretisation in the momentum and energy equation. We used the boundary conditions as previously discussed and chose  $\Delta t = 0.001$ . After 830 time steps a stationary solution was obtained, that is  $\|\mathbf{u}^{k+1} - \mathbf{u}^k\| < \frac{1-\lambda}{\lambda}(c_1 + \|\mathbf{u}^k\|c_2)$ , with  $c_1 = 10^{-6}$  the absolute stationary accuracy and  $c_2 = 10^{-2}$  the relative stationary accuracy and  $\lambda$  the computed speed of convergence.

The resulting Mach number in the domain is shown in Figure 10.4. For clarity, this figure is not to scale, but has been compressed in the longitudinal direction. A close-up of the iso Mach contours in the air inlet is presented in Figure 10.5. The Mach number at the boundary of the air inlet is  $M = 1$ . As can be seen from Figure 10.5 the Mach number is high at the end of the air inlet, up to  $M = 1.239$ , where it merges into the fiber channel. At this point the flow expands. Note that the jet into the fiber channel in the beginning very much stays near the lower wall. This is due to an under pressure in the right corner of air and fiber inlet, which causes the flow to be sucked around the corner. At the left corner the subsonic flow from the fiber inlet and the transonic flow from the air inlet meet, and a flow separation can be observed. Half way the fiber inlet there is a small recirculation zone (not shown). This recirculation is probably caused by the diffusive first order upwind scheme, since in inviscid flow recirculations should not appear. As can be seen from Figure 10.6 the flow is uniform at the end of the fiber channel. This is again the result of the upwinding. The Mach number at the outlet is  $M_{out} = 0.59$ , which is approximately twice as large as the Mach number measured. This is not unexpected since in our inviscid flow computations we did not take into account the losses due to viscous stresses, except for the small amount of dissipation due to the first order upwind method.

### Computational results for viscous flow

In the computations we used the original compressible flow pressure correction formulation and first order upwind discretisation in the momentum and energy equation. We used the boundary conditions as previously discussed and again  $\Delta t = 0.001$ . The difference with the computations for inviscid flow are the no-slip boundary conditions at the walls. After 4011 time steps a stationary solution was obtained.

The resulting Mach number in the domain is shown in Figure 10.7. A close-up of the iso Mach contours in the air inlet is presented in Figure 10.8. Compared to the Mach numbers for inviscid flow the Mach numbers in viscous flow are smaller. The maximum Mach number, for example is here  $M_{max} = 0.593$ , whereas for the inviscid case it is much larger:  $M_{max} = 1.382$ . This difference is caused by the losses that occur



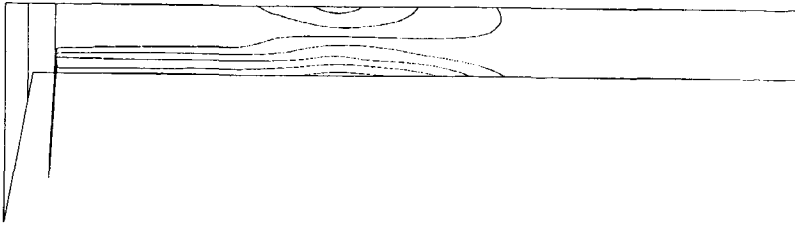


Figure 10.4: Iso Mach contours for inviscid flow in a straight blower,  $\Delta M = 0.142$

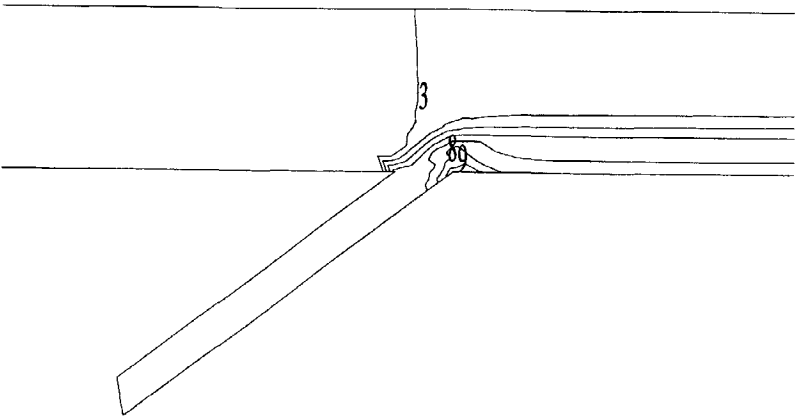


Figure 10.5: Iso Mach contours for inviscid flow in a straight blower, close-up of air inlet, levels: 3 = 0.386; 8 = 1.097; 9 = 1.239,  $\Delta M = 0.142$

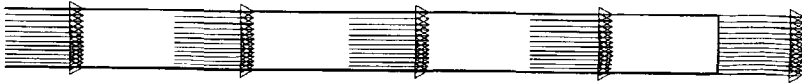


Figure 10.6: Velocity at end of fiber channel for inviscid flow in a straight blower

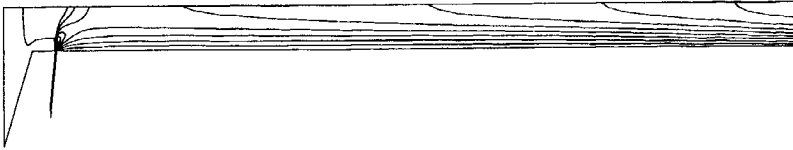


Figure 10.7: Iso Mach contours for viscous flow in a straight blower,  $\Delta M = 0.066$

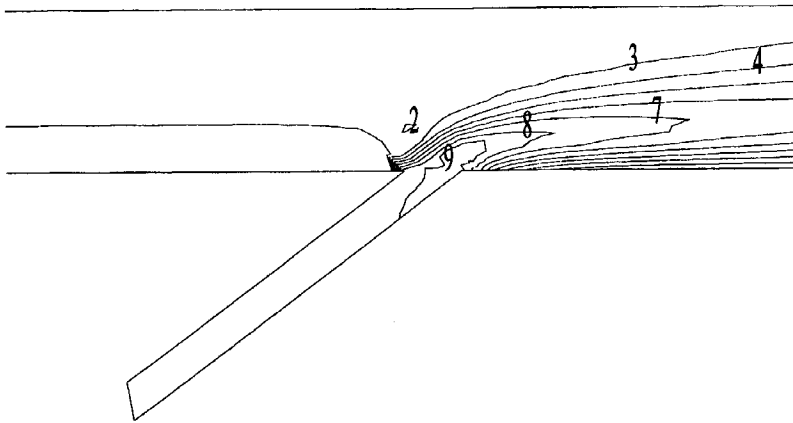


Figure 10.8: Iso Mach contours for viscous flow in a straight blower, close-up of air inlet, levels: 2 = 0.128; 3 = 0.194; 7 = 0.394; 8 = 0.460; 9 = 0.526;  $\Delta M = 0.066$



Figure 10.9: Velocity at end of fiber channel for viscous flow in a straight blower

in viscous flow at the walls. This is also the cause of the different flow pattern. As can be seen from Figure 10.9 the flow profile at the outlet is parabolic, due to the no-slip boundary condition at the wall. In reality the form will be different due to turbulence. The Mach number at the outlet goes from 0 at the wall to 0.57 at the symmetry plane. As a result the computed mean Mach number at the outlet is 0.38, which is close to 0.3, the Mach number following from Persoon's measurements. In Figure 10.10 the flow pattern at the point where the air inlet ends in the fiber channel is shown.

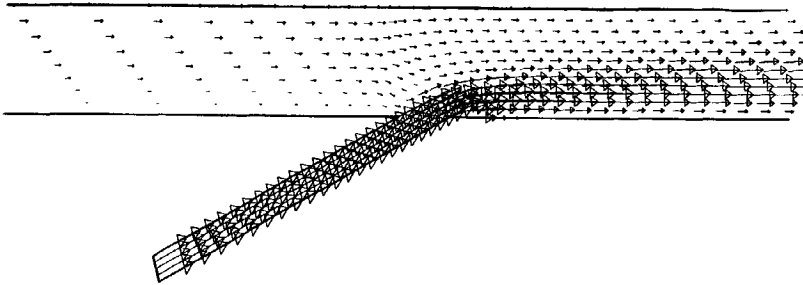


Figure 10.10: Velocity field at end of air inlet

#### 10.1.4 Computational results for fiber channel with widening

Results of computations of viscous flow in a blower with a widening will be shown and compared with viscous flow in a straight channel. In the computations we used the original compressible flow pressure correction formulation and first order upwind discretisation in the momentum and energy equation. We used the viscous flow boundary conditions as previously discussed, where we assumed the amount of air entrained in the widened channel to be the same as in the straight channel case. We chose  $\Delta t = 0.001$ . After 3021 time steps a stationary solution was obtained.

The resulting Mach number in the domain is shown in Figure 10.11. A close-up of the iso Mach contours in the air inlet is presented in Figure 10.12. Compared to the Mach numbers for the straight channel the Mach numbers in the widened channel are larger. The maximum Mach number, for example is here 0.822, whereas for the straight channel it is 0.593. Apparently the wider channel results in less resistance so that the flow can attain a higher speed. This is desirable, since the pulling force of the blower depends on the difference in speed between the air and the fiber. The larger this speed difference the larger the force, hence the larger the speed at the symmetry plane, the

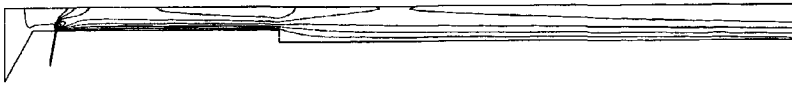


Figure 10.11: Iso Mach contours for viscous flow in a widened blower,  $\Delta M = 0.092$

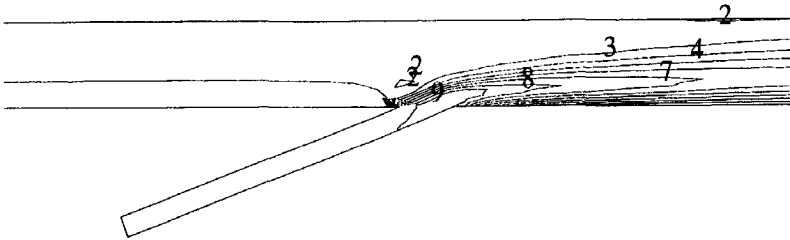


Figure 10.12: Iso Mach contours for viscous flow in a widened blower, close-up of air inlet, levels: 2=0.085; 3=0.177; 4=0.269; 7=0.546; 8=0.638; 9=0.730;  $\Delta M = 0.092$

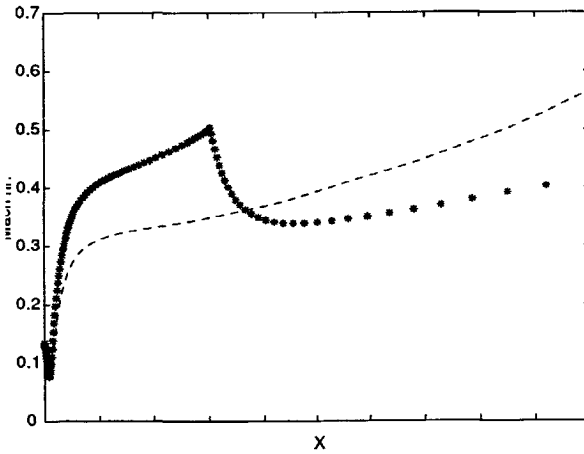


Figure 10.13: Mach number at symmetry line, --- = straight channel, \* = widened channel

better. In Figure 10.13 the Mach number at the symmetry line is plotted for both the straight and the widened channel. The surface between the x-axis and the line can be seen as a measure of the force on the fiber. For both channels the pull force seems to be approximately the same, while one would expect, given the difference in maximum Mach numbers, the widened channel to result in a larger force on the fiber. The reason for this might be that we kept the entrained flow through the fiber inlet constant, while one would expect faster flow to entrain more mass, resulting in a larger mass flux, hence a larger force on the fiber.

## 10.2 Flow around an airfoil

In this section we will show results of the calculation of an external flow with a stagnation point: inviscid flow around an airfoil. Since the purpose is primarily to show the accuracy and convergence of our numerical method for flows with stagnation points, the example is restricted to non-lifting inviscid flow around a NACA0012 airfoil.

### Mesh

We used an O-mesh, of  $128 \times 80$  grid points, displayed in Figure 10.14. In this mesh the gridlines are perpendicular to the surface, which turned out to be important for convergence of our method. For our computations the entire mesh was used, so that the symmetry of the computed flow field can be tested. The mesh extends about 100 chords from the profile. The O-mesh has one point near the trailing edge, where two edges of a finite volume cell almost collapse, so that the cell almost becomes a triangle, see Figure 10.15. This appeared to be a hard cell for our general coordinate method. Without the improved discretisation described in [73, 85, 83], mentioned in Section 5.2, the computed flow near the trailing edge became distorted. Hence the improved discretisation was used.

### Subsonic flow

Two computations of subsonic inviscid flow around the NACA0012 airfoil have been performed, one for  $M_\infty = 0.01$  and for  $M_\infty = 0.1$ . We used  $\Delta t = 0.001$ . For both computations a central discretisation was used. We did not find spurious wiggles, and convergence to the stationary solution was obtained for  $M_\infty = 0.01$  in 12,341 time steps and for  $M_\infty = 0.1$  in 13,009 time steps. Here, we assumed the solution to be converged when  $\|\mathbf{u}^{k+1} - \mathbf{u}^k\| < \frac{1-\lambda}{\lambda}(c_1 + \|\mathbf{u}^k\|c_2)$ , with  $c_1 = 10^{-6}$  the absolute stationary accuracy and  $c_2 = 10^{-2}$  the relative stationary accuracy and  $\lambda$  the computed speed of convergence. The resulting iso Mach contours are shown in Figure 10.16 and 10.17. As expected the contour plots for  $M_\infty = 0.01$  and for  $M_\infty = 0.1$  are symmetric and the same. The maximum Mach number for  $M_\infty = 0.01$  was  $M_{max} = 0.012$  and for  $M_\infty = 0.1$  was  $M_{max} = 0.12$ . Compared with [77], who found maximum Mach numbers of 0.01187 and 0.1186, this is only a difference of less than 2%.

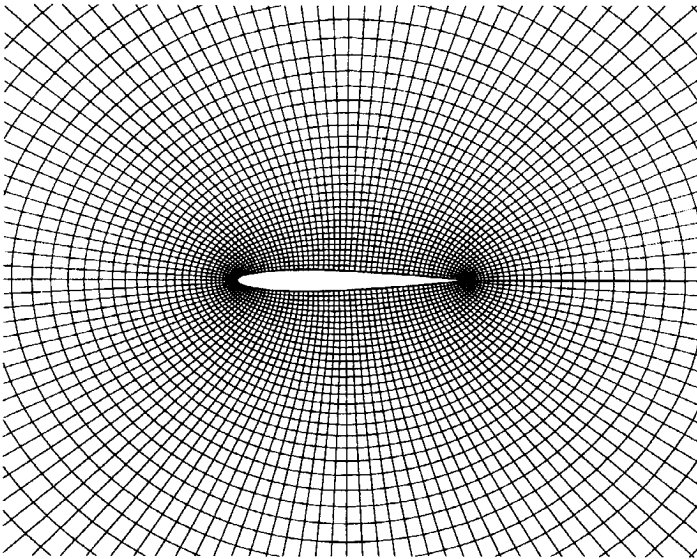


Figure 10.14: Airfoil, O-mesh

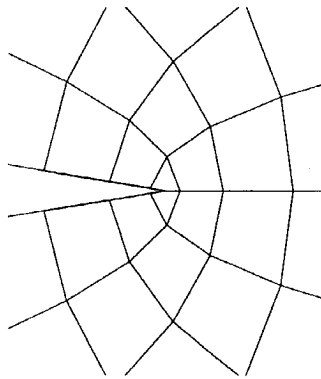


Figure 10.15: Airfoil, distorted cell at trailing edge

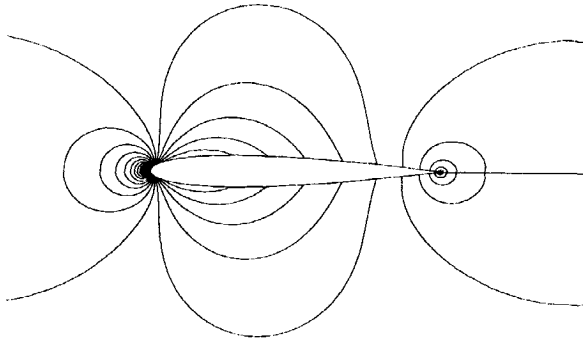


Figure 10.16: Airfoil, Iso Mach contours for  $M_\infty = 0.01$ ,  $M_{max} = 0.012$ ,  $\Delta M = 0.0004$

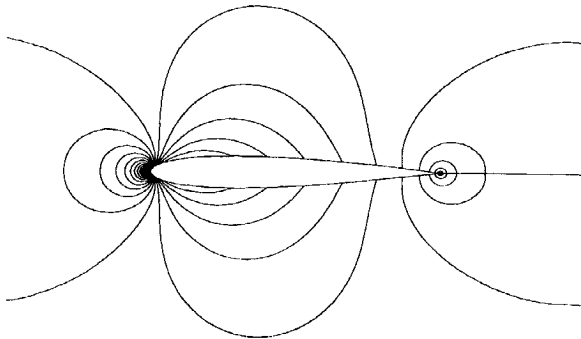


Figure 10.17: Airfoil, Iso Mach contours for  $M_\infty = 0.1$ ,  $M_{max} = 0.12$ ,  $\Delta M = 0.004$

### Transonic flow

In the computation of flow around the NACA0012 airfoil with  $M_\infty = 0.85$  we did observe spurious wiggles. Since the first order upwind scheme is not yet implemented for the improved discretisation we tried to damp the wiggles using artificial dissipation. In Figure 10.18 the iso Mach contours for an artificial viscosity coefficient of  $\mu_{art} = 10^{-4}$  are shown. The shock which should appear is smeared and the iso Mach contours are too much skewed backwards, for comparison see for example [77]. When we used less damping wiggles arose and no stationary solution was obtained. With more damping, artificial viscosity equal to  $\mu_{art} = 10^{-3}$ , the shock was even more smeared as can be seen from the pressure coefficient on the upper side of the profile as shown in Figure 10.19. A close-up at the stagnation point shown in Figure 10.20 shows that the flow near the stagnation point is not disturbed.

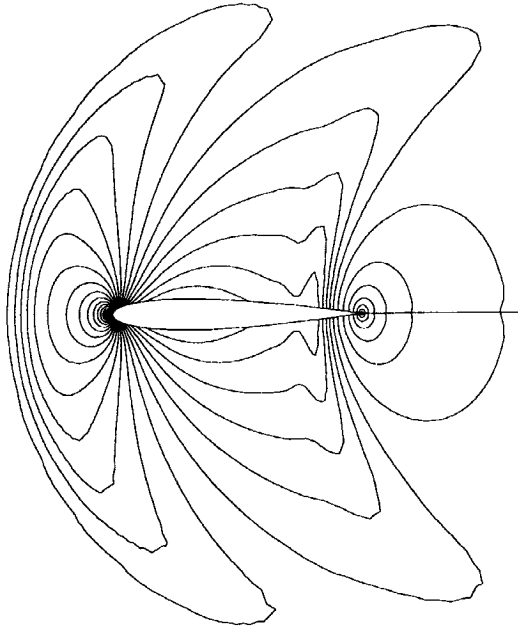


Figure 10.18: Airfoil, Iso Mach contours for  $M_\infty = 0.85$ ,  $M_{max} = 1.1$ ,  $\Delta M = 0.032$ ,  $\mu_{art} = 1 \cdot 10^{-3}$



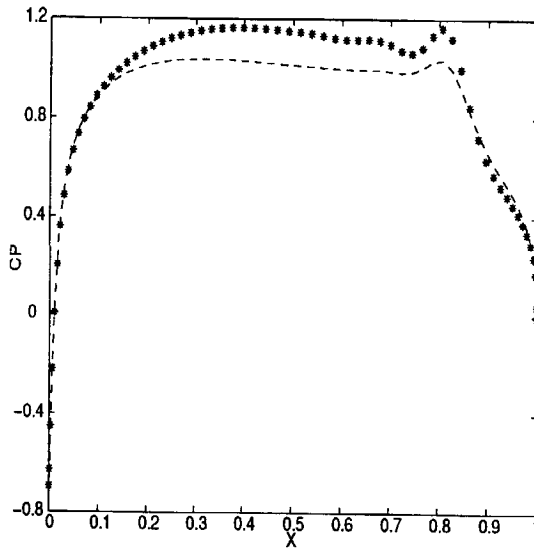


Figure 10.19: Pressure coefficient on profile  $M_\infty = 0.85$ ,  $-- = \mu_{art} = 10^{-3}$ ,  $* = \mu_{art} = 10^{-4}$

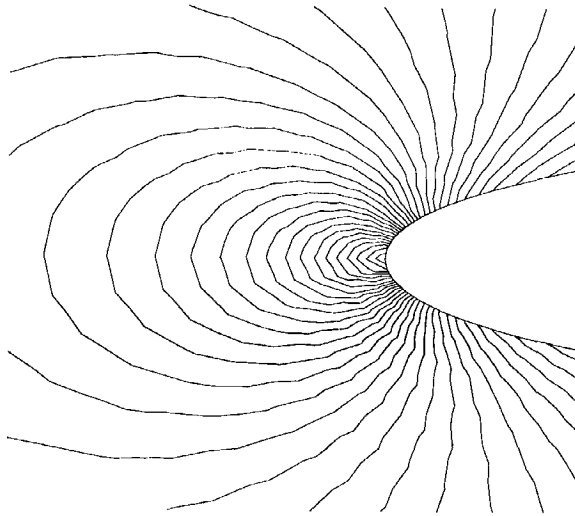


Figure 10.20: Airfoil, Iso Mach contours for  $M_\infty = 0.85$ ,  $M_{max} = 1.1$ ,  $\Delta M = 0.032$ ,  $\mu_{art} = 1 \cdot 10^{-3}$ , close-up near stagnation point

### 10.2.1 Final remarks

Of course, there is still room for improvement and for more tests. We did not try our method on low speed variable density flow, such as low speed combustion. It would be interesting to see how our method will perform for these flows with strong temperature gradients. Another interesting application is two-phase flow. Currently, a PhD-student is working on extension of our method for these flows. Nevertheless, we may say that:

- Feasibility of the basic idea has been sufficiently shown.
- The original aim was to develop a unified method for incompressible and subsonic flow. It came as a pleasant surprise to find that the method works for transonic and supersonic flows as well.

## Bibliography

- [1] J.D. Anderson. *Modern compressible flow with historical perspective*. McGraw-Hill, 1990.
- [2] R. Aris. *Vectors, tensors and the basic equations of fluid mechanics*. Prentice-Hall, Inc., Englewood Cliffs, N.J., 1962. Reprinted, Dover, New York, 1989.
- [3] M. Arora and P.L. Roe. A well-behaved TVD limiter for high-resolution calculations of unsteady flow. *J. Comp. Phys.*, 132:3–11, 1997.
- [4] G.K. Batchelor. *An Introduction to Fluid Dynamics*. Cambridge University Press, Cambridge, UK, 1967.
- [5] H. Bijl and P. Wesseling. A numerical method for the computation of viscous flows at all speeds. To appear in *Proceedings of ENUMATH 97, Heidelberg*.
- [6] H. Bijl and P. Wesseling. A method for the numerical solution of the almost incompressible Euler equations. Report 96-37, Faculty of Technical Mathematics and Informatics, Delft University of Technology, Delft, 1996.
- [7] H. Bijl and P. Wesseling. A numerical method for computing flows for arbitrarily small and medium mach number. In J.L. Lumley L. Fulachier and F. Anselmet, editors, *Proceedings of the IUTAM Symposium on Variable Density Low-Speed Turbulent Flows*, pages 317–324, Dordrecht, 1996. Kluwer Academic Publishers.
- [8] H. Bijl and P. Wesseling. A numerical method for the computation of compressible flows with low Mach number regions. In J.-A. Désidéri, C. Hirsch, P. Le Tallec, M. Pandolfi, and J. Périaux, editors, *Computational Fluid Dynamics '96*, pages 206 – 212. Wiley, Chichester, 1996.
- [9] H. Bijl and P. Wesseling. A numerical method for the computation of compressible viscous flows with low Mach number regions. In K. Kozel M. Feistauer and R. Rannacher, editors, *Proceedings of the Symposium on Numerical Modelling in Continuum Mechanics*, pages 149–59, Prague, 1997. Matfyzpress, Charles University.
- [10] H. Bijl and P. Wesseling. A unified method for computing incompressible and compressible flows in boundary-fitted coordinates. *J. Comp. Phys.*, 141:153–173, 1998.

- [11] W.R. Briley, H. McDonald, and S.J. Shamroth. A low Mach number Euler formulation and application to time-iterative LBI schemes. *AIAA J.*, 21:1467-1469, 1983.
- [12] V. Casulli and D. Greenspan. Pressure method for the numerical solution of transient, compressible fluid flows. *Int. J. Num. Meth. Fl.*, 4:1001-12, 1984.
- [13] D.R. Chenoweth and S. Paolucci. Natural convection in an enclosed vertical air layer with large horizontal temperature differences. *J. Fluid Mech.*, 169:173-210, 1986.
- [14] Y.-H. Choi and C.L. Merkle. The application of preconditioning in viscous flows. *J. Comp. Phys.*, 105:207-223, 1993.
- [15] L. Davidson and P. Hedberg. Mathematical derivation of a finite volume formulation for laminar flow in complex geometries. *Int. J. Num. Meth. Fluids*, 9:531-540, 1989.
- [16] I. Demirdžić, Z. Lilek, and M. Perić. A collocated finite volume method for predicting flows at all speeds. *Int. J. Num. Meth. Fluids*, 16:1029-1050, 1993.
- [17] S. Eidelman, P. Colella, and R.P. Shreeve. Application of the Godunov method and its second-order extension to cascade flow modelling. *AIAA J.*, 22:1609-1615, 1984.
- [18] A.G. Godfrey, R.W. Walters, and B. van Leer. Preconditioning for the Navier-Stokes equations with finite rate chemistry. AIAA Paper 93-0535, 1993.
- [19] J. Guerra and B. Gustafsson. A numerical method for incompressible and compressible flow problems with smooth solutions. *J. Comp. Phys.*, 63:377-397, 1986.
- [20] W.G. Habashi and M.M. Hafez. Finite element method for transonic cascade flows. AIAA Paper 81-1472, 1981.
- [21] F.H. Harlow and A.A. Amsden. Numerical calculation of almost incompressible flows. *J. Comp. Phys.*, 3:80-93, 1968.
- [22] F.H. Harlow and A.A. Amsden. A numerical fluid dynamics calculation method for all flow speeds. *J. Comp. Phys.*, 8:197-213, 1971.
- [23] F.H. Harlow and J.E. Welch. Numerical calculation of time-dependent viscous incompressible flow of fluid with a free surface. *The Physics of Fluids*, 8:2182-2189, 1965.
- [24] A. Harten. High resolution schemes for hyperbolic conservation laws. *J. Comp. Phys.*, 49:357-393, 1983.

- [25] A. Harten, B. Engquist, S. Osher, and S.R. Chakravarty. Uniformly high order accurate essentially non-oscillatory schemes, III. *J. Comp. Phys.*, 71:231–303, 1987.
- [26] C. Hirsch. *Numerical Computation of Internal and External Flows. Vol.2: Computational Methods for Inviscid and Viscous Flows*. John Wiley, Chichester, 1990.
- [27] C. W. Hirt, A. A. Amsden, and J. L. Cook. An arbitrary Lagrangian-Eulerian computing method for all flow speeds. *J. Comp. Phys.*, 14:227–253, 1974.
- [28] A. Hosangadi, C.L. Merkle, and S.R. Turns. Analysis of forced combusting jets. *AIAA J.*, 28:1473–1480, 1990.
- [29] T.J.R. Hughes and M. Mallet. A new finite element formulation for computational fluid dynamics: III. The generalized streamline operator for multi-dimensional advective-diffusive schemes. *Comp. Meth. for Appl. Mech. Eng.*, 58:305–28, 1986.
- [30] T. Ikhagi, B.R. Shin, and H. Daiguji. Application of an implicit time-marching scheme to a three-dimensional incompressible flow problem in curvilinear coordinate systems. *Computers and Fluids*, 21:163–175, 1992.
- [31] R. I. Issa, A. D. Gosman, and A. P. Watkins. The computation of compressible and incompressible flows by a non-iterative implicit scheme. *J. Comp. Phys.*, 62:66–82, 1986.
- [32] R.I. Issa. Solution of the implicitly discretised fluid flow equations by operator-splitting. *J. Comp. Phys.*, 62:40–65, 1986.
- [33] S.M.H. Karimian and G.E. Schneider. Pressure-based control volume finite element method for flow at all speeds. *AIAA J.*, 33:1611–1618, 1995.
- [34] K.C. Karki and S.V. Patankar. Pressure based calculation procedure for viscous flows at all speed in arbitrary configurations. *AIAA J.*, 27:1167–1174, 1989.
- [35] S. Klainerman and A. Majda. Singular limits of quasilinear hyperbolic systems with large parameters and the incompressible limit of compressible fluids. *Comm. Pure Appl. Math.*, 34:481–524, 1981.
- [36] S. Klainerman and A. Majda. Compressible and incompressible flows. *Comm. Pure Appl. Math.*, 35:629–651, 1982.
- [37] R. Klein. Semi-implicit extension of a Godunov-type scheme based on low Mach number asymptotics I: one-dimensional flow. *J. Comp. Phys.*, 121:213–237, 1995.

- [38] R. Klein and C.D. Munz. The multiple pressure variable (mpv) approach for the numerical approximation of weakly compressible fluid flow. In K. Kozel, editor, *Proceedings of Numerical Modelling in Continuum Mechanics*, pages 47–54, Prague, 1994. Matfyzpress.
- [39] S. Koshizuka, Y. Oka, and S. Kondo. A staggered differencing technique on boundary-fitted curvilinear grids for incompressible flows along curvilinear or slant walls. *Computational Mechanics*, 7:123–136, 1990.
- [40] H.O. Kreiss, J. Lorenz, and M.J. Naughton. Convergence of the solutions of the compressible to the solutions of the incompressible Navier-Stokes equations. *Adv. Appl. Math.*, 12:187–214, 1991.
- [41] P.D. Lax. Weak solutions of nonlinear hyperbolic equations and their numerical approximation. *Comm. Pure Appl. Math.*, 7:150–193, 1954.
- [42] H.W. Liepmann and A. Roshko. *Elements of gasdynamics*. John Wiley & Sons, New York, 1957.
- [43] A. Majda. *Compressible fluid flow and systems of conservation laws in several space variables*, volume 53 of *Applied Mathematical Sciences*. Springer, New York, 1984.
- [44] A. Majda and J. Sethian. The derivation and numerical solution of the equations for zero Mach number combustion. *Combust. Sci. and Tech.*, 42:185–105, 1985.
- [45] P.A. McMurtry, W.H. Jou, J.J. Riley, and R.W. Metcalfe. Direct numerical simulations of a reacting mixing layer with chemical heat release. *AIAA J.*, 24:962–970, 1986.
- [46] C.L. Merkle and Y.-H. Choi. Computation of low-speed compressible flows with time marching procedures. *Int. J. Numer. Methods Eng.*, 25:831–838, 1988.
- [47] K. Morinishi. Comparison of numerical solutions of pseudocompressible flows and compressible flows at low Mach numbers. AIAA Paper 92-2648, 1992.
- [48] B. Müller. *Computation of compressible low Mach number flow*. PhD-thesis, ETH, Zürich, 1996.
- [49] E.S. Oran and J.P. Boris. Detailed modelling of combustion systems. *Prog. Energy Combust. Sci.*, 7:1–72, 1981.
- [50] S. Osher and S. Chakravarthy. Upwind schemes and boundary conditions with applications to Euler equations in general geometries. *J. Comp. Phys.*, 50:447–481, 1983.
- [51] S. Osher and F. Solomon. Upwind difference schemes for hyperbolic systems of conservation laws. *Math. Comp.*, 38:339–374, 1982.

- [52] R.L. Panton. *Incompressible Flow*. John Wiley, New York, 1984.
- [53] G. Patnaik, R.H. Guirguis, J.P. Boris, and E.S. Oran. A barely implicit correction for flux-corrected transport. *J. Comp. Phys.*, 71:1–20, 1987.
- [54] H.C.J. Persoon. Analysis of flow phenomena in transport jet of spunlaid process. Master's thesis, Delft University of Technology, 1997.
- [55] R.H. Pletcher and K.H. Chen. On solving the compressible Navier-Stokes equations for unsteady flows at very low Mach numbers. AIAA Paper 93-3368, 1993.
- [56] P.Wesseling, A. Segal, C.G.M. Kassels, H. Bijl, and M. Zijlema. Computing flows on general three-dimensional nonsmooth staggered grids. Report 97-23, Faculty of Technical Mathematics and Informatics, Delft University of Technology, Delft, 1997.
- [57] R.G. Rehm and H.R. Baum. The equations of motion for thermally driven buoyant flows. *J. Res. Nat. Bur. Stand.*, 83:297–308, 1978.
- [58] C.M. Rhie and W.L. Chow. Numerical study of the turbulent flow past an airfoil with trailing edge separation. *AIAA J.*, 21:1525–1532, 1983.
- [59] M. Rosenfeld, D. Kwak, and M. Vinokur. A fractional step solution method for the unsteady incompressible Navier-Stokes equations in generalized coordinate systems. *J. Comp. Phys.*, 94:102–137, 1991.
- [60] Y. Saad and M.H. Schultz. GMRES: a generalized minimal residual algorithm for solving non-symmetric linear systems. *SIAM J. Sci. Stat. Comp.*, 7:856–869, 1986.
- [61] A. Segal, P. Wesseling, J. van Kan, C.W. Oosterlee, and K. Kassels. Invariant discretization of the incompressible Navier-Stokes equations in boundary fitted co-ordinates. *Int. J. Num. Meth. Fluids*, 15:411–426, 1992.
- [62] J. Sesterhenn, B. Müller, and H. Thomann. On the cancellation problem in calculating compressible and incompressible flows. In J.-A. Désidéri, C. Hirsch, P. Le Tallec, M. Pandolfi, and J. Périaux, editors, *Computational Fluid Dynamics '96*, pages 57–61, Chichester, 1996. Wiley.
- [63] J.-S. Shuen, K.-H. Chen, and Y. Choi. A coupled implicit method for chemical non-equilibrium flows at all speeds. *J. Comp. Phys.*, 106:306–318, 1993.
- [64] W. Shyy. A numerical study of two-dimensional compressible Navier-Stokes flows. *Num. Heat Transfer*, 14:323–341, 1988.
- [65] W. Shyy and M.E. Braaten. Adaptive grid computation for inviscid compressible flows using a pressure correction method. AIAA Paper 88-3566-CP, 1988.

- [66] W. Shyy, M.-H. Chen, and C.-S. Sun. Pressure-based multigrid algorithm for flow at all speeds. *AIAA J.*, 30:2660–2669, 1992.
- [67] W. Shyy and C.-S. Sun. Development of a pressure-correction/staggered-grid based multigrid solver for incompressible recirculating flows. *Computers and Fluids*, 22:51–76, 1992.
- [68] G.A. Sod. A survey of several finite difference methods for systems of nonlinear conservation laws. *J. Comp. Phys.*, 27:1–31, 1978.
- [69] M.C. Thompson and J.H. Ferziger. An adaptive multigrid technique for the incompressible Navier-Stokes equations. *J. Comp. Phys.*, 82:94–121, 1989.
- [70] E.F. Toro. *Riemann solvers and numerical methods for fluid dynamics*. Springer, Berlin, 1997.
- [71] E. Turkel. Review of preconditioning techniques for fluid dynamics. *Appl. Num. Math.*, 12:257–284, 1993.
- [72] E. Turkel, A. Fiterman, and B. van Leer. Preconditioning and the limit to the incompressible flow equations. Report 93-42, ICASE, NASA Langley, 1993.
- [73] P. van Beek, R.R.P. van Nooyen, and P. Wesseling. Accurate discretization on non-uniform curvilinear staggered grids. *J. Comp. Phys.*, 117:364–367, 1995.
- [74] J.J.I.M. Van Kan. A second-order accurate pressure correction method for viscous incompressible flow. *SIAM J. Sci. Stat. Comp.*, 7:870–891, 1986.
- [75] B. van Leer. Towards the ultimate conservative difference scheme. V. A second-order sequel to Godunov's method. *J. Comput. Phys.*, 32:101–136, 1979.
- [76] B. van Leer, W.-T. Lee, and P.L. Roe. Characteristic time-stepping or local preconditioning of the Euler equations. AIAA Paper 91-1552, 1991.
- [77] B. van Leer, L. Mesaros, C.-H. Tai, and E. Turkel. Local preconditioning in a stagnation point. AIAA Paper 95-1654, 1995.
- [78] S. Venkateswaran, C.L. Merkle, and S.T. Thynell. Analysis of direct solar thermal rocket propulsion. *J. Propulsion Power*, 8:541–547, 1992.
- [79] H. Viviand. Pseudo-unsteady systems for steady inviscid flow calculations. In F. Angrand, A. Dervieux, and J.A. Désidéri, editors, *Numerical methods for the Euler equations of fluid dynamics*, pages 334–368, Philadelphia, 1985. SIAM.
- [80] C. Vuik. Solution of the discretized incompressible Navier-Stokes equations with the GMRES method. *Int. J. Num. Meth. Fluids*, 16:507–523, 1993.
- [81] C. Vuik. Fast iterative solvers for the discretized incompressible Navier-Stokes equations. *Int. J. Num. Meth. Fluids*, 22:195–210, 1996.



- [82] P. Wesseling, C.G.M. Kassels, C.W. Oosterlee, A. Segal, C. Vuik, S. Zeng, and M. Zijlema. Computing incompressible flows in general domains. In F.-K. Hebeker, R. Rannacher, and G. Wittum, editors, *Numerical methods for the Navier-Stokes equations*, pages 298–314, Braunschweig, 1994. Vieweg.
- [83] P. Wesseling, A. Segal, C.G.M. Kassels, and H. Bijl. Computing flows on general two-dimensional nonsmooth staggered grids. *J. Eng. Math.*, 34:21–44, 1998.
- [84] P. Wesseling, A. Segal, J.J.I.M. van Kan, C.W. Oosterlee, and C.G.M. Kassels. Finite volume discretization of the incompressible Navier-Stokes equations in general coordinates on staggered grids. *Comp. Fluid Dynamics Journal*, 1:27–33, 1992.
- [85] P. Wesseling, P. van Beek, and R.R.P. van Nooyen. Aspects of non-smoothness in flow computations. In A. Peters, G. Wittum, B. Herrling, U. Meissner, C.A. Brebbia, W.G. Gray, and G.F. Pinder, editors, *Computational Methods in Water Resources X*, pages 1263 – 1271, Dordrecht, 1994. Kluwer.
- [86] J.P. Withington, J.S. Shuen, and V. Yang. A time accurate implicit method for chemically reacting flows at all Mach numbers. AIAA Paper 91-0581, 1991.
- [87] S. Zeng, C. Vuik, and P. Wesseling. Numerical solution of the incompressible Navier-Stokes equations by Krylov subspace and multigrid methods. *Advances in Computational Mathematics*, 4:27–50, 1995.
- [88] G. Zhou and L. Davidson. A pressure-based euler scheme for transonic internal and external flow simulation. *Comp. Fluid Dyn.*, 5:169–188, 1995.
- [89] O.C. Zienkiewicz, K. Morgan, B.V.K. Satya Sai, R. Codina, and M. Vasquez. A general algorithm for compressible and incompressible flow. *Int. J. Num. Meth. Fl.*, 20:887–913, 1995.
- [90] M. Zijlema. *Computational modeling of turbulent flows in general domains*. PhD thesis, Delft University of Technology, The Netherlands, April 1996.
- [91] M. Zijlema. On the construction of a third-order accurate monotone convection scheme with application to turbulent flow in general coordinates. *Int. J. Num. Meth. Fluids*, 22:619–641, 1996.
- [92] M. Zijlema, A. Segal, and P. Wesseling. Finite volume computation of incompressible turbulent flows in general coordinates on staggered grids. *Int. J. Num. Meth. Fluids*, 20:621–640, 1995.
- [93] M. Zijlema, A. Segal, and P. Wesseling. Invariant discretization of the  $k-\epsilon$  model in general co-ordinates for prediction of turbulent flow in complicated geometries. *Computers and Fluids*, 24:209–225, 1995.

- [94] M. Zijlema and P. Wesseling. Higher order flux-limiting methods for steady-state, multidimensional, convection-dominated flow. Report 95-131, Faculty of Technical Mathematics and Informatics, Delft University of Technology, Delft, 1995.

# Samenvatting

## Berekening van stromingen met alle snelheden met een 'staggered' schema

Binnen de Numerieke Stromingsleer bestaat een streng onderscheid tussen methoden ter berekening van compressibele stromingen enerzijds en incompressibele stromingen anderzijds. Dit maakt berekening van stromingen met zowel compressibele als incompressibele gebieden niet eenvoudig. De toepassing van methoden voor de berekening van compressibele stromingen - hoewel relatief eenvoudig - leidt in de regel tot aanzienlijke convergentieproblemen of zelfs afbreken van de berekening indien gebieden met lage Mach getallen voorkomen.

In dit proefschrift wordt een methode geïntroduceerd gericht op de efficiënte en nauwkeurige berekening van zowel compressibele als incompressibele stromingen. Tests hebben aangetoond dat met deze methode een nauwkeurige oplossing kan worden bepaald in een beperkte, niet van het Mach getal afhankelijke rekentijd. Bovendien kan een arbitrair klein Mach getal worden opgelegd, of zelfs nul, waarna het incompressibele schema van Harlow en Welch [24] (in orthogonale coördinaten) of dat van Zijlema et al. [89,90] (in algemene coördinaten) wordt verkregen. Op relatief eenvoudige wijze wordt temporale nauwkeurigheid behaald, zonder gebruik van een pseudo-tijdsvariabele en duale tijdstappen zoals in zoveel andere methoden noodzakelijk is. De prestaties van deze methode bij volledig compressibele stromingen zijn daarnaast verrassend gunstig.

De twee belangrijkste onderdelen van de methode zijn:

- nondimensionalisering van de variabelen teneinde de singulariteit die optreedt bij  $M \downarrow 0$  op te heffen
- discretisatie van de compressibele stromingsvergelijkingen op een "staggered" rooster ten einde de "spurious" modes in de druk die ontstaan bij  $M \downarrow 0$  te voorkomen

De primaire onbekenden zijn massaflux, druk en enthalpie. Bij deze methode worden allereerst de dimensieloze compressibele stromingsvergelijkingen met behulp van de eindige volume methode gediscretiseerd op een staggered rooster. Daarna worden deze vergelijkingen gediscretiseerd in de tijd met de  $\theta$ -methode en opgelost met een compressibele uitbreiding van de drukcorrectiemethode. Dit houdt in dat na de energiev-

ergelijking een massaflux-predictorvergelijking wordt opgelost. De voorspelde massaflux wordt dan gecorrigeerd met een term die bepaald wordt door oplossing van de drukcorrectievergelijking, een vergelijking die is verkregen uit manipulatie van de oorspronkelijke vergelijkingen. Alledrie de systemen van discrete vergelijkingen worden opgelost met behulp van een gepreconditioneerde Krylov subspace-methode: gepreconditioneerde GMRES.

Op basis van verschillende testproblemen wordt geconcludeerd dat deze methode bij de berekening van stromingen met alle snelheden efficiënt en nauwkeurig is. Dat wil zeggen dat een nauwkeurige oplossing kan worden bepaald in een beperkte tijd met een niet van het Mach-getal afhankelijke convergentiesnelheid. Dit is gedaan voor een kanaal met bump met Mach-getallen van 0 tot 0,5 en voor een sterk convergerende-divergerende nozzle met Mach-getallen van 0,045 tot 2,67 in hetzelfde domein. Bovendien wordt bij schokken eenzelfde nauwkeurigheid bereikt als met andere methoden met een vergelijkbaar nauwkeurige discretisatie. Dit is aangetoond voor het kanaal met bump met Mach-getallen aan de inlaat van 0,675 en 1,65. Ook voor volledig compressibele niet-stationaire stromingen is dit staggered rooster schema net zo nauwkeurig als "colocated" compressibele schema's. Dit is aangetoond voor voor verschillende Riemann-problemen, waar schokken, contactdiscontinuïteiten en expansiegolven voorkomen. Daarnaast is deze methode ook geschikt voor de berekening van stromingen met stagnatiepunten, zoals aangetoond voor het NACA0012 profiel. Ten slotte is deze methode ook geschikt gebleken voor praktische toepassingen met verschillende Mach-getallen, zoals een industriële blazeropstelling van AKZO Nobel.

Hester Bijl

# Curriculum Vitae

- December 15 1970    Born in Voorburg
- 1982 - 1988        Haags Montessori Lyceum, Den Haag, The Netherlands,  
secondary school, VWO (9 subjects).
- 1988 - 1994        Delft University of Technology, The Netherlands,  
Master's degree in Applied Mathematics,  
subject: Computational Fluid Dynamics.
- 1994                Oxford University Computing Laboratory, United Kingdom,  
Second part of graduation project in Computational Fluid  
Dynamics, for Rolls Royce aero engines,  
subject: Parallelisation of Preconditioned Iterative Methods.
- 1991 - 1997        Leiden State University, The Netherlands,  
Master's degree in English Language and Literature,  
subject: English Syntax.
- 1994 - 1998        Delft University of Technology, The Netherlands,  
PhD-student in Computational Fluid Dynamics,  
supported by the Dutch Technology Foundation (STW),  
research subject: design and implementation of an accurate  
and efficient numerical method for compressible flows  
with low Mach numbers.
- summer 1997       Summer visitor at ICASE Institute, NASA Langley, USA,  
performed computations on flow around an airfoil.
- 1998 - present     Senior Associate Consultant, The Boston Consulting Group.

**Publications**

- H. Bijl and P. Wesseling, A numerical method for the computation of compressible flows with low Mach number regions, in: J-A Désidéri, C Hirsch, P. Le Tallec, M. Pandolfi, and J. Périaux (eds.), *Computational Fluid Dynamics '96 Proceedings of the Third Eccomas CFD Conference*, Paris/France, September 9-13, 1996, John Wiley & Sons, ISBN 0-471-95851-4, Chichester, 1996, p. 206-212.
- H. Bijl and P. Wesseling, A numerical method for computing flows for arbitrarily small and medium Mach numbers, in: L. Fulachier, J.L. Lumley, and F. Anselmet (eds.), *Proceedings of the IUTAM Symposium on Variable Density Low-Speed Turbulent Flows*, Marseille/France, July 8-10, 1996, Kluwer Academic Publishers, ISBN 0-7923-4602-5, Dordrecht, 1997, p. 317-324.
- H. Bijl and P. Wesseling, *A method for the numerical solution of the almost incompressible Euler equations*, Report 96-37, Faculty of Technical Mathematics and Informatics, Delft University of Technology, 1996.
- H. Bijl and P. Wesseling, A numerical method for the computation of compressible viscous flows with low Mach number regions, in: M. Feistauer, K. Kozel, and R. Rannacher (eds.), *Proceedings of the Symposium on Numerical Modelling in Continuum Mechanics*, Prague/Czech Republic, 8-11 September 1997, Matfyzpress, ISBN 80-85863-25-1, Prague 1997, p. 149-59.
- P.Wesseling, A. Segal, C.G.M. Kassels, and H. Bijl, *Computing Flows on General Three-Dimensional Nonsmooth Staggered Grids*, Report 97-23, Faculty of Technical Mathematics and Informatics, Delft University of Technology, 1997.
- P.Wesseling, A. Segal, C.G.M. Kassels, H. Bijl and M. Zijlema, *Computing Flows on General Nonsmooth Staggered Grids*, Report 97-14, Faculty of Technical Mathematics and Informatics, Delft University of Technology, 1997.
- H. Bijl and P. Wesseling, A Unified Method for Computing Incompressible and Compressible Flows in Boundary-Fitted Coordinates, *J. Comp. Phys.*, 141: 153-73, 1998.
- P.Wesseling, A. Segal, C.G.M. Kassels, H. Bijl and M. Zijlema, Computing flows on general two-dimensional nonsmooth staggered grids, *J. Eng. Math.*, 34: 21-44, 1998.
- H. Bijl and P. Wesseling, A numerical method for the computation of viscous flows at all speeds, to appear in: *Proceedings of ENUMATH 97*, Heidelberg/Germany, 1998, World Scientific, Singapore.